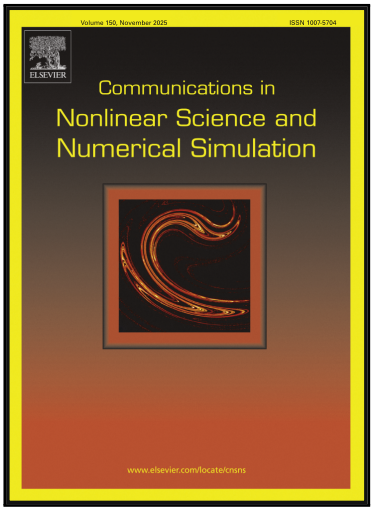

Unified isogeometric-SUC model for nonlinear stability analysis of fuzzy fiber-reinforced composite microplates comprising various strain gradient tensors besides interphase region

Saeid Sahmani , Eligiusz Postek , Reza Ansari ,
Mohammad Kazem Hassanzadeh-Aghdam

PII: S1007-5704(26)00406-5
DOI: https://doi.org/10.1016/j.cnsns.2026.110047
Reference: CNSNS 110047

To appear in: *Communications in Nonlinear Science and Numerical Simulation*

Received date: 23 June 2025
Revised date: 6 February 2026
Accepted date: 13 April 2026

Please cite this article as: Saeid Sahmani , Eligiusz Postek , Reza Ansari , Mohammad Kazem Hassanzadeh-Aghdam , Unified isogeometric-SUC model for nonlinear stability analysis of fuzzy fiber-reinforced composite microplates comprising various strain gradient tensors besides interphase region, *Communications in Nonlinear Science and Numerical Simulation* (2026), doi: https://doi.org/10.1016/j.cnsns.2026.110047

Highlights

- Development a MSGT-based size-dependent isogeometric-SUC model
- Modeling of FFRC contains uniformly aligned CNTs grown radially on the glass fibers
- Isogeometric-based numerical analysis of nonlinear stability of arbitrary-shaped FFRC microplates
- Numerical tracing of the nonlinear equilibrium paths incorporating interphase region resulting from van der Waals interactions

Unified isogeometric-SUC model for nonlinear stability analysis of fuzzy fiber-reinforced composite microplates comprising various strain gradient tensors besides interphase region

Saeid Sahmani[a,b,c]*, Eligiusz Postek[b], Reza Ansari[d,a]*, Mohammad Kazem Hassanzadeh-Aghdam[e]

[a] *Department of Civil Engineering, School of Science and Technology, The University of Georgia, Tbilisi 0171, Georgia*
[b] *Institute of Fundamental Technological Research, Polish Academy of Sciences, Pawińskiego 5B, 02-106 Warsaw, Poland*
[c] *School of Civil, Environmental, and Architectural Engineering, Korea University, Seoul 02841, Republic of Korea*
[d] *Faculty of Mechanical Engineering, University of Guilan, Rasht, Iran*
[e] *Department of Engineering Science, Faculty of Technology and Engineering, East of Guilan, University of Guilan, Rudsar-Vajargah, Iran*

Abstract

In the present exploration, by unifying the simplified unit cell (SUC) micromechanical approach with the isogeometric numerical technique, a new solution model is developed to examine the small-scale dependent nonlinear stability feature of fuzzy fiber reinforced composite (FFRC) microplates under in-plane axial compression. A notable structural feature of this hybrid composite is the presence of uniformly aligned radially grown carbon nanotubes (CNTs) on the surfaces of the glass fibers, all of equal length, together with the interphase area between the nanotubes and the polymer material. Additionally, the interphase region between CNTs and the matrix is modeled as a distinct phase. To capture the influence of material microstructure, the effective elastic constants are first predicted using the SUC micromechanics model, while size-dependent effects are incorporated through the modified strain gradient theory. These material characteristics are then combined with an isogeometric plate formulation to enable accurate and efficient numerical analysis of FFRC microplates with different geometries and boundary conditions. The results show that the presence of CNTs as well as the interphase region significantly enhances both the buckling resistance and postbuckling stability through improving the stiffness and load transfer capability, particularly when the interphase becomes thicker or stiffer. The examination also highlights the influence of glass fiber volume fraction as well as the role of strain gradient tensors in enhancing the load-bearing capability. Overall, the proposed framework provides a consistent link between micromechanical design features and structural-scale stability performance of FFRC microstructures.

Keywords: Micromechanical model; Fuzzy fiber-reinforced composites; Size dependency; Interphase region; Isogeometric analysis.

*Corresponding authors.
E-mail addresses: s.sahmani@ug.edu.ge; ssahmani@ippt.pan.pl (S. Sahmani); r_ansari@guilan.ac.ir; r.ansari@ug.edu.ge (R. Ansari)

1. Introduction

The importance of developing carbon nanotube (CNT)-filled nanocomposites is increasing as demand for high-performance materials grows, especially in the aircraft and aerospace industries. Compared to the dispersion of CNTs in polymer matrices followed by fiber insertion, direct growth of CNTs on fiber surfaces can be an alternative and more promising route to obtain high-performance nanocomposites [1-4]. Such a fiber coated with radially grown CNTs on its surface is called "fuzzy fiber" [1,5,6] and the resulting nanocomposite is a fuzzy fiber-reinforced composite (FFRC). A comprehensive understanding of mechanical properties and behavior of FFRCs is needed to use these nanocomposites in engineering applications. Kundalwal and Ray [7] predicted the elastic properties of an FFRC using the analytical and numerical micromechanics methods. The results showed that the transverse elastic constants of the FFRC are notably enhanced owning to the radial growth of CNTs on the fiber surface at nanoscale. Dhala and Ray [8] determined the piezoelectric and elastic properties of the piezoelectric FFRCs by the micromechanics approach. They reported that the in-plane elastic and piezoelectric constants of the piezoelectric FFRC are enhanced as compared to the piezoelectric composites without CNTs. Hassanzadeh-Aghdam et al. [9] employed a unit cell-based model for exploring the mechanical properties of FFRCs under off-axis loadings. It was observed that, by increasing the off-axis angle from 0° to 90°, the elastic modulus of the FFRC reduces to 45° and then rises. Also, the growth of nanotubes on the fiber surface led to the maximum improvement of the elastic modulus of 90° on-axis specimen [9].

To capture an accurate design for microscale structures, the role of size dependency must be taken into consideration. To accomplish this, several alternative continuum theories of elasticity have been proposed and resorted in the last decade. One of them, which has delineated coherent appropriateness at microscale, is the modified strain gradient theory (MSGT) [10]. For instance, Ansari et al. [11] examined the small-scale dependent nonlinear free oscillations of heterogeneous Timoshenko microbeams using the MSGT. Akgoz and Civalek [12] presented a new sinusoidal beam model within the MSGT framework to obtain an exact solution for the buckling of microbeams. Jamalpoor et al. [13] developed an MSGT-based plate model for biaxial buckling response of dual-orthotropic microplate systems in the presence of a magnetic field. Zhang et al. [14] predicted the critical buckling loads and natural frequencies of inhomogeneous microplates on the basis of MSGT. Mohammadimehr et al. [15] formulated an MSGT-based Reddy plate model for flexural analysis of piezoelectric composite microplates reinforced with CNTs. Shojaeian et al. [16] explored the MSGT-based electromechanical stability features of naosize bridges incorporating the geometrical nonlinearity besides the van der Waals force. Yaghoubi et al. [17] explored the stability behavior of centrosymmetric heterogeneous microbeams by combining the Euler-Bernoulli beam theory and MSGT. Mirsalehi et al. [18] employed the spline finite strip methodology for buckling and free oscillation analyses of inhomogeneous microplates based upon the MSGT. Khakalo et

al. [19] investigated the bending, vibration, and buckling responses of two-dimensional triangular lattices on the basis of MSGT. Salehipour and Shahsavar [20] employed the three-dimensional elasticity within the MSGT framework for free oscillations of graded composite microplates. Arefi et al. [21] examined the MSGT-based thermomechanical buckling of functionally graded microscale higher-order shear flexible plates. Farzam and Hassani [22] modeled the temperature-dependent composite microplates and captures their critical thermal buckling loads via the MSGT-based isogeometric model. Zhang et al. [23] examined the static and dynamic characteristics of third-order shear deformable beams at microscale by using a MSGT-based finite element approach. Fu et al. [24] explained different applications of the MSGT in modeling of microstructures made of isotropic materials. Bacciocchi and Tarantino [25] established a MSGT-based third-order shear flexible plate model to obtain an analytical solution for the linear stability and vibrations of sandwich composite microplates. Zheng et al. [26] proposed a MSGT-based trigonometric theoretical framework for thermomechanical stability analysis of multilayer nanocomposite microplates.

More recently, Torabi and Niiranen [27] established a MSGT-based finite element solving process using quasi-continuous triangular element for the nonlinear bending analysis of sandwich microplates having a prismatic corrugated core. Sun et al. [28] explored the nonlinear lateral stability behavior of random reinforced composite microshells via a MSGT-based moving Kriging meshfree numerical solution. Chu et al. [29] and Wang et al. [30] advanced MSGT-based isogeometric numerical models for, respectively, nonlinear vibrations and stability characteristics of functionally graded porous microplates. Fu et al. [31] studies the effects of different strain gradient tensors on the buckling response of partially covered sandwich microbeams using the MSGT. Le et al. [32] introduced a size-dependent shell model based upon the generalized form of the strain gradient continuum elasticity including the constructive equations besides the required boundary conditions. Hung et al. [33,34] constructed a MSGT-based isogeometric numerical model to calculate the natural frequencies and bending response of porous microsize plates. Khorshidi et al. [35] calculated the size-dependent natural frequencies of microplates subjected to the influence of the fluid medium using the MSGT within the framework of the higher-order shear flexibility. Xiang et al. [36] introduced a new closed-form solution to analyze the size-dependent flexural oscillations of microplates on the basis of the MSGT of continuum mechanics. Hai et al. [37] predicted the free vibration characteristics of laminated microplates possessing a honeycomb lattice structure coated by piezoelectric actuators via the MSGT-based sinusoidal shear flexible plate formulations. Barbaros et al. [38] employed the MSGT within the curved beam model for the nonlinear in-plane stability behavior shallow microsize arches. Karamanli et al. [39] represented MSGT-based finite element models for transient response of functionally graded inhomogeneous microplates. Hou et al. [40] anticipated the vibrational response of cylindrical microshells via developing a MSGT-based meshfree

formulations. Jain et al. [41] inspected the thermal instability behavior of porous microplates under localized heating through formulating the MSGT-based Reddy's plate theory. Sahmani et al. [42] developed a NSGT-based isogeometric collocation curved beam model for the nonlinear stability characteristics of microsize arches having graded through-thickness porosity. Nguyen et al. [43] investigated the roles of various microstructural gradient tensors in the linear mechanical behaviors of metal foam microbeams based on the MSGT-based Reddy beam model. Sahmani et al. [44] traced the transient dynamical response of actuated piezoelectric microplate-type energy harvesters by the MSGT-based piezoelectric plate formulations. Zhou and Huang [45] constructed a MSGT-based Kirchhoff-Love plate framework for static and dynamic stability analysis of microplates. Mirzaei et al. [46] explored the size-dependent mechanical behaviors of bi-directional graded porous microplates having inconstant thickness with the aid of a MSGT-based isogeometric analysis. Sahmani et al. [47] proposed an isogeometric solving process based on the MSGT to explore the nonlinear asymmetric instability characteristics of arch-kind structures at microscale. Saffari et al. [48] examined the energy harvesting application of fluid-immersed bimorph laminated microplates based on the MSGT continuum elasticity with different edge supports. Imani et al. [49] proposed a MSGT-based finite element approach to capture the size-dependent natural frequencies of functionally graded heterogeneous curved microbeams.

Although micromechanical modeling of fuzzy fiber-reinforced composites using the SUC approach and size-dependent plate formulations based on the MSGT of elasticity have each been investigated independently, an integrated computational platform capable of linking micromechanics, interphase modeling, and nonlinear plate stability within an isogeometric framework has not yet been reported. Accordingly, the present study contributes in this direction by developing a novel unified isogeometric-SUC model to numerically analyze the nonlinear stability response of FFRC microplates with arbitrary geometries. This model incorporates the interfacial zone between the radially aligned CNTs and the polymer matrix, which arises from van der Waals interactions. To account for size effects, the isogeometric-SUC model of FFRC microplates is derived based on the MSGT. In this regard:

- Based upon the SUC part of the developed unified computational model, the mechanical properties of a newly proposed FFRC composing of uniformly aligned carbon nanotubes of equal length grown radially on the surface of the glass fibers are extracted.
- Based upon the isogeometric part of the developed unified computational model, the nonlinear stability characteristics of microplates made of this newly proposed FFRC are predicted attributed to diverse geometries as well as various newly proposed material parameters.

Therefore, beyond the methodological integration, the proposed numerical strategy allows a detailed exploration of how CNT volume fraction, glass nanofiber content, interphase thickness and stiffness, and

strain gradient microstructural-dependent parameters jointly influence both the buckling and postbuckling responses of axially compressed FFRC microplates.

2. Micromechanical modeling

In this section, a micromechanical investigation is conducted to analyze the mechanical properties of FFRCs. Herein, the material behavior of the FFRC constituents is considered linearly elastic and temperature-independent. Therefore, material nonlinearity, viscoelasticity and thermal loading effects are not addressed. In most of the analytical and numerical studies [7], [50-53], it is assumed that the reinforcement phase in the composite is arranged in a repeating array as shown in Figure 1. In unit cell models, such as the method of cells [7], [54] and the simplified unit cell (SUC) technique [9], the cross-section of the reinforcement phase is represented as rectangular that it is illustrated in Figure 2. To derive the micromechanical formulations, the displacement components are assumed to be linear which results in the constant stress and strain components into the sub-cells. Furthermore, it is assumed that the normal stresses applied to the representative volume element (RVE) do not induce shear stresses in the sub-cells, and vice versa [7,8], [51-53].

2.1. SUC model

In this study, as shown in Figure 3, the RVE of the composite is divided into an $r \times c$ grid of rectangular cells in the SUC model. The RVE has dimensions L_c and L_r in the x- and y-directions, sequentially, with a unit length in the z-direction. If i is the counter variable in the x-direction and j in the y-direction, each cell is identified by the designation ij. The length of each cell in the x-direction is denoted by a_i, and in the y-direction by b_j. The RVE expands in both the x- and y-directions. The subsequent sections provide a detailed explanation of the governing equations for this method subjected to the normal and shear loading conditions.

2.1.1. Normal loading case

Equilibrium equations relating the global stresses on the faces of the RVE, represented as ($\overline{S_i}$), and the local stresses within the sub-cell ij, denoted as (σ_i^{ij}), can be expressed as [8,9], [54,55]

$$\sum_{i=1}^{c} \sigma_y^{1i} a_i = \overline{S_y} L_c$$

$$\sum_{j=1}^{r} \sigma_x^{1j} b_j = \overline{S_x} L_r \tag{1}$$

$$\sum_{j=1}^{r} \sum_{i=1}^{c} b_j \, a_i \sigma_z^{ij} = \overline{S_z} L_r L_c$$

Furthermore, another relation is attained from the balance of local stress along the interfaces between the sub-cells

$$\sigma_x^{1j} = \sigma_x^{ij} \quad (i > 1)$$
$$\sigma_y^{i1} = \sigma_y^{ij} \quad (j > 1) \tag{2}$$

The RVE kinematic boundary conditions, which guarantee the displacement compatibility mandated by the definition of the RVE, are formulated as follows [7-9]

$$\sum_{i=1}^{c} a_i \varepsilon_x^{i1} = \sum_{i=1}^{c} a_i \varepsilon_x^{ij} = L_c \bar{\varepsilon}_x \quad (j > 1)$$

$$\sum_{j=1}^{r} b_j \varepsilon_y^{1j} = \sum_{j=1}^{r} b_j \varepsilon_y^{ij} = L_r \bar{\varepsilon}_y \quad (i > 1) \tag{3}$$

$$\varepsilon_z^{ij} = \overline{\varepsilon_z} \; (i > 1 \, , j > 1)$$

In Eq. (3), $\overline{\varepsilon_l}$ denotes the global strain, and ε_l^{ij} represents the local strain. The stress-strain formula for the sub-cell ij can be written as

$$\{\varepsilon\}^{ij} = [\mathrm{S}]^{ij} \{\sigma\}^{ij} \tag{4}$$

where $\{\sigma\}^{ij}$ and $\{\varepsilon\}^{ij}$ represent the normal stress and strain first-order tensor components, respectively, and $[\mathrm{S}]^{ij}$ indicates the elastic compliance tensor for the sub-cell ij.

By extending Eq. (4), one can write

$$\begin{cases} \varepsilon_x^{ij} = \dfrac{1}{E^{ij}} \sigma_x^{ij} - \dfrac{v^{ij}}{E^{ij}} (\sigma_y^{ij} + \sigma_z^{ij}) \\ \varepsilon_y^{ij} = \dfrac{1}{E^{ij}} \sigma_y^{ij} - \dfrac{v^{ij}}{E^{ij}} (\sigma_x^{ij} + \sigma_z^{ij}) \\ \varepsilon_z^{ij} = \dfrac{1}{E^{ij}} \sigma_z^{ij} - \dfrac{v^{ij}}{E^{ij}} (\sigma_x^{ij} + \sigma_y^{ij}) \end{cases} \tag{5}$$

where v and E denote Poisson's ratio and Young's modulus, sequentially. Substitution of Eq. (4) into (3), utilizing Eqs. (1) and (2), a system of equation is attained as

$$[\mathbf{A}]_{m\times m}[\boldsymbol{\sigma}]_{m\times 1} = [\mathbf{F}]_{m\times 1} \quad (m = c + r + rc) \tag{6}$$

here $[\mathbf{A}]_{m\times m}$ is the coefficient tensor, $[\mathbf{F}]_{m\times 1}$ is the vector of external forces, and $[\boldsymbol{\sigma}]_{m\times 1}$ is the local stress vector.

2.1.2. Shear loading case

For deriving the equations for shear loading, a similar approach is employed for the global shear stresses. The initial set of equations is derived by equating the global shear stresses ($\bar{\tau}_{kl}$) to the corresponding local shear stresses (τ_{kl}^{ij}) into the sub-cell ij (here, k and l indicate the x or y directions)

$$\begin{aligned} &\sum_{i=1}^{c} \tau_{yz}^{ij} a_i = \bar{\tau}_{yz} L_c \\ &\sum_{j=1}^{r} \tau_{xz}^{ij} b_j = \bar{\tau}_{xz} L_r \\ &\tau_{xy}^{ij} = \bar{\tau}_{xy} \end{aligned} \tag{7}$$

Considering shear strain compatibility inside each sub-cell locally, Eq. (8) is attained

$$\begin{aligned} &\varepsilon_{xz}^{i1} = \varepsilon_{xz}^{ij} \quad (j > 1) \\ &\varepsilon_{yz}^{1j} = \varepsilon_{yz}^{ij} \quad (i > 1) \end{aligned} \tag{8}$$

The kinematic boundary conditions in the case of shear loads yields

$$\begin{aligned} &\sum_{i=1}^{c} a_i \varepsilon_{xz}^{i1} = L_c \bar{\varepsilon}_{xz} \\ &\sum_{j=1}^{r} b_j \varepsilon_{yz}^{1j} = L_r \bar{\varepsilon}_{yz} \\ &\sum_{j=1}^{r}\sum_{i=1}^{c} b_j\, a_i \varepsilon_{xy}^{ij} = \bar{\varepsilon}_{xy} L_r L_c \end{aligned} \tag{9}$$

Utilizing Eqs. (7-9) as well as Hooke's law, the corresponding equations for the shear loads are obtained. Longitudinal shear modulus ($\bar{G}_{xz}$ or $\bar{G}_{yz}$) as well as the transverse shear modulus ($\bar{G}_{xy}$) can be indicated as

$$\frac{L_r}{\bar{G}_{yz}} = \sum_{j=1}^{r} \frac{b_j}{\sum_{i=1}^{c} a_i G^{ij}}$$

$$\frac{L_c}{\bar{G}_{xz}} = \sum_{i=1}^{c} \frac{a_i}{\sum_{j=1}^{r} b_j G^{ij}} \tag{10}$$

$$\frac{L_r L_c}{\bar{G}_{xy}} = \sum_{j=1}^{r} \sum_{i=1}^{c} \frac{a_i b_j}{G^{ij}}$$

2.2. Multi-step procedure for FFRC modeling

Figure 4a illustrates a layer of a FFRC. A notable structural feature of this hybrid composite is the presence of uniformly aligned, radially grown CNTs of equal length, aligned with the glass fibers. The CNTs are assumed to exhibit transverse isotropy, with their transverse isotropy axis aligned perpendicular to the fiber surface. Figure 4b depicts a fuzzy fiber. When this fuzzy fiber is embedded in a polymer matrix, the gaps between the CNTs are filled with the polymer. The radially aligned CNTs enhance the transverse reinforcement of the polymer matrix surrounding the glass fiber. A fuzzy fiber, with the polymer matrix filling the gaps between the CNTs, is referred to as a composite fuzzy fiber [7]. It can be modeled as a glass fiber embedded into the polymer matrix reinforced by CNTs. Figure 4c also presents a transverse cross-section of a composite fuzzy fiber (CFF).

The initial phase of this analysis employs the SUC micromechanical model to determine the elastic properties of the polymer matrix nanocomposite (PMNC). The PMNC consists of CNTs reinforcing phase and a polymer matrix. Between the CNTs and the polymer matrix lies an interphase region, resulting from van der Waals (vdW) interactions. Research has demonstrated that this interphase significantly influences the mechanical performance of nanotube-filled polymer composite systems [7], [56]. This interphase layer envelops the nanofillers with a specific thickness, and its characteristics depend on the manufacturing methods and curing conditions [7], [47], [57,58].

Figure 5(a) presents a cross-sectional schematic of an unrolled CFF, where radially aligned CNT-reinforced composites surround the glass fiber core. Upon rolling, this configuration forms the CFF, as shown in Figure 5(b) [8,9]. The elastic properties of the rolled PMNC are determined as

$$\left[\mathbf{C}^{\mathrm{PMNC}}\right] = \frac{1}{\pi(R^2 - a^2)} \int_0^{2\pi} \int_a^R \left[\bar{\mathbf{C}}^{\mathrm{PMNC}}\right] r dr d\alpha \tag{11}$$

here a and R denote the glass fiber radius at nanoscale and the sum of fiber radius and nanotube length. Considering $[\bar{\mathbf{C}}^{NC}]$ as the elastic stiffness tensor of unrolled PMNC, $\left[\bar{\mathbf{C}}^{\mathrm{PMNC}}\right]$ can be presented as

$$\left[\bar{\mathbf{C}}^{\mathrm{PMNC}}\right] = [\mathbf{T}]^{-T} [\bar{\mathbf{C}}^{NC}] [\mathbf{T}]^{-1} \tag{12}$$

Additionally, [**T**] is expressed as

$$[\mathbf{T}]=\begin{bmatrix} 1 & 0 & 0 & 0 & 0 & 0 \\ 0 & \cos^2\alpha & \sin^2\alpha & \cos\alpha\sin\alpha & 0 & 0 \\ 0 & \sin^2\alpha & \cos^2\alpha & -\cos\alpha\sin\alpha & 0 & 0 \\ 0 & -2\cos\alpha\sin\alpha & 2\cos\alpha\sin\alpha & \cos^2\alpha-\sin^2\alpha & 0 & 0 \\ 0 & 0 & 0 & 0 & \cos\alpha & \sin\alpha \\ 0 & 0 & 0 & 0 & \sin\alpha & \cos\alpha \end{bmatrix} \tag{13}$$

Once the elastic properties of the rolled PMNC are determined, the next step is to derive the properties of the CFF. This is achieved by treating the PMNC as the matrix phase and the glass fiber as the reinforcing phase. Finally, the elastic properties of the FFRC are calculated by considering the CFF as the reinforcement and the polymer matrix as the matrix phase. These calculations are carried out using the micromechanical model.

2.3. Composite constituents

The FFRC is made of CNT, glass fibers, and an epoxy matrix. Additionally, the interfacial area among the nanotubes and the matrix is modeled as a distinct phase. The mechanical properties of the CNT, glass fibers, and epoxy matrix are provided in Table 1 [7], [50], [55], [59]. The glass fiber diameter is assumed to be 5 μm. The elastic modulus and Poisson's ratio of the interphase are considered to be ten times the modulus of the matrix and equal to the matrix's Poisson ratio [54-56], respectively. At the same time, its thickness is taken to be half the nanotube diameter.

In modeling the FFRC, the volume fraction occupied by the nanotubes (V_{CNT}) depends on the nanotube diameter, the diameter of the glass fiber, and the spacing between adjacent nanotube surfaces. The maximum volume fraction of CNTs in this type of composite can be expressed by the following equation [52,53,60]

$$(V_{\mathrm{CNT}})_{max}=\frac{\pi d^2}{2(d+1.7)^2}\left(\sqrt{\frac{\pi v_f}{2\sqrt{3}}}-v_f\right) \tag{14}$$

where v_f represents the volume fraction of glass fibers in the FFRC, and d is the nanotube's diameter.

According to the previous explorations using the SUC micromechanics approach, some of the advantages allocated to the constructed SUC part of the present unified computational model include simplicity as well as efficiency [61], capability to give closed-form formulations [62], applicable to elastic and thermal properties [63], extendable to different geometrics associated with the reinforcement phase [61], considering directional behavior of the reinforcement phase such as isotropic, transversely isotropic,

etc. [64], applicable to general on-axis, off-axis and multiaxial loading conditions [65], considering some different materials simultaneously [66], and applicable to local phenomena such as damage, debonding, and etc. [67].

3. MSGT-based isogeometric formulations of FFRC microplates

In order to describe the displacement field of the studied FFRC microplate as shown in Figure 6, the refined exponential shear flexible plate theory [68] is adopted. It presents two key advantages. First, unlike the first-order shear flexibility theory, it does not require a shear correction factor, which is challenging to determine due to its dependence on various specifications. Second, in contrast to third-order shear flexible theory, the bending elements do not affect the shear elements for in-plane and transverse displacements, and vice versa. This significantly simplifies the constitutive equations in these refined theories compared to their third-order counterparts. Therefore, it yields

$$\boldsymbol{\mathcal{U}} = \begin{Bmatrix} \mathcal{U}_x(x,y,z) \\ \mathcal{U}_y(x,y,z) \\ \mathcal{U}_z(x,y,z) \end{Bmatrix} = \begin{Bmatrix} u(x,y) \\ v(x,y) \\ w(x,y) \end{Bmatrix} - z \begin{Bmatrix} \dfrac{\partial w(x,y)}{\partial x} \\ \dfrac{\partial w(x,y)}{\partial y} \\ 0 \end{Bmatrix} + ze^{-\frac{2z^2}{h^2}} \begin{Bmatrix} \psi_x(x,y) \\ \psi_y(x,y) \\ 0 \end{Bmatrix} = \boldsymbol{\mathcal{U}}^{(\mathbf{0})} - z\boldsymbol{\mathcal{U}}^{(\mathbf{1})} + ze^{-\frac{2z^2}{h^2}}\boldsymbol{\mathcal{U}}^{(\mathbf{2})} \tag{15}$$

where u, v and w in order refer to the displacement elements allocated to a random point located on the midplane of FFRC microplate across the x, y, and z axes. Also, ψ_x and ψ_y mention the rotations of the FFRC microplate about y and x axes, respectively.

As a result, in classical (CL) view of the FFRC microplate, the elements of exponential shear flexible strain tensor comprising the von Karman geometrical nonlinearity is derived as

$$\boldsymbol{\varepsilon}_{\mathbf{b}} = \begin{Bmatrix} \varepsilon_{xx} \\ \varepsilon_{yy} \\ \gamma_{xy} \end{Bmatrix} = \begin{Bmatrix} \dfrac{\partial u}{\partial x} + \dfrac{1}{2}\left(\dfrac{\partial w}{\partial x}\right)^2 \\ \dfrac{\partial v}{\partial y} + \dfrac{1}{2}\left(\dfrac{\partial w}{\partial y}\right)^2 \\ \dfrac{\partial u}{\partial y} + \dfrac{\partial v}{\partial x} + \dfrac{\partial w}{\partial x}\dfrac{\partial w}{\partial y} \end{Bmatrix} + z \begin{Bmatrix} -\dfrac{\partial^2 w}{\partial x^2} \\ -\dfrac{\partial^2 w}{\partial y^2} \\ -2\dfrac{\partial^2 w}{\partial x \partial y} \end{Bmatrix} + ze^{-\frac{2z^2}{h^2}} \begin{Bmatrix} \dfrac{\partial \psi_x}{\partial x} \\ \dfrac{\partial \psi_y}{\partial y} \\ \dfrac{\partial \psi_x}{\partial y} + \dfrac{\partial \psi_y}{\partial x} \end{Bmatrix}$$

$$= \boldsymbol{\varepsilon}_{\mathbf{b}}^{(\mathbf{0})} + z\boldsymbol{\varepsilon}_{\mathbf{b}}^{(\mathbf{1})} + ze^{-\frac{2z^2}{h^2}}\boldsymbol{\varepsilon}_{\mathbf{b}}^{(\mathbf{2})} \tag{16a}$$

$$\boldsymbol{\varepsilon}_{\mathbf{s}} = \begin{Bmatrix} \gamma_{xz} \\ \gamma_{yz} \end{Bmatrix} = e^{-\frac{2z^2}{h^2}} \begin{Bmatrix} \psi_x \\ \psi_y \end{Bmatrix} + \frac{4z^2}{h^2} e^{-\frac{2z^2}{h^2}} \begin{Bmatrix} -\psi_x \\ -\psi_y \end{Bmatrix} = e^{-\frac{2z^2}{h^2}}\boldsymbol{\varepsilon}_{\mathbf{s}}^{(\mathbf{0})} + \frac{4z^2}{h^2} e^{-\frac{2z^2}{h^2}}\boldsymbol{\varepsilon}_{\mathbf{s}}^{(\mathbf{1})} \tag{16b}$$

Based around the idea of MSGT [10], one will have the following microstructural gradient tensors attributed to the exponential shear flexible FFRC microplate. These size-dependent tensors represent a

complete higher-order kinematic description of microstructural interactions, and their simultaneous inclusion is essential to preserve the theoretical consistency of MSGT [10] and its experimentally supported size-dependent behavior.

As the first one, the rotation gradient tensor contains the succeeding elements

$$\chi_{ij} = \frac{1}{2}\left(\frac{\partial \theta_i}{\partial j} + \frac{\partial \theta_j}{\partial i}\right) \tag{17}$$

in which θ_i stands for the components of the rotation vector. So, it yields the attributed elements as given in Appendix A.

As the second one, the dilatation gradient tensor contains the succeeding elements

$$\boldsymbol{\varsigma}_i = \frac{\partial \varepsilon_{mm}}{\partial i} \tag{18}$$

which are presented in Appendix A.

As the third one, the deviatoric stretch gradient tensor contains the succeeding elements

$$\boldsymbol{\eta}_{ijk} = \frac{1}{3}\left(\frac{\partial \varepsilon_{jk}}{\partial i} + \frac{\partial \varepsilon_{ki}}{\partial j} + \frac{\partial \varepsilon_{ij}}{\partial k}\right) - \frac{1}{15}\left[\delta_{ij}\left(\frac{\partial \varepsilon_{mm}}{\partial k} + 2\frac{\partial \varepsilon_{mk}}{\partial m}\right) + \delta_{jk}\left(\frac{\partial \varepsilon_{mm}}{\partial i} + 2\frac{\partial \varepsilon_{mi}}{\partial m}\right) + \delta_{ki}\left(\frac{\partial \varepsilon_{mm}}{\partial j} + 2\frac{\partial \varepsilon_{mj}}{\partial m}\right)\right] \tag{19}$$

So, it results in the allocated components as written in Appendix A.

Inevitably, the CL-based as well as MSGT-based characteristic equations attributed to the FFRC microplates can be manifested as

$$\begin{Bmatrix} \sigma_{xx} \\ \sigma_{yy} \\ \tau_{xz} \\ \tau_{yz} \\ \tau_{xy} \end{Bmatrix} = \begin{bmatrix} Q_{11}^{SUC} & Q_{12}^{SUC} & 0 & 0 & 0 \\ Q_{21}^{SUC} & Q_{22}^{SUC} & 0 & 0 & 0 \\ 0 & 0 & Q_{44}^{SUC} & 0 & 0 \\ 0 & 0 & 0 & Q_{55}^{SUC} & 0 \\ 0 & 0 & 0 & 0 & Q_{66}^{SUC} \end{bmatrix} \begin{Bmatrix} \varepsilon_{xx} \\ \varepsilon_{yy} \\ \gamma_{xz} \\ \gamma_{yz} \\ \gamma_{xy} \end{Bmatrix}$$

$$\{m_{xx}, m_{yy}, m_{zz}, m_{xy}, m_{xz}, m_{yz}\} = [2l_0^2 C_{55}]\{\chi_{xx}, \chi_{yy}, \chi_{zz}, \chi_{xy}, \chi_{xz}, \chi_{yz}\} \tag{20}$$

$$\{p_x, p_y, p_z\} = [2l_1^2 C_{55}]\{\varsigma_x, \varsigma_y, \varsigma_z\}$$

$$\{\tau_{xxx}, \tau_{yyy}, \tau_{xxy}, \tau_{xyy}, \tau_{xzz}, \tau_{yzz}\} = [2l_2^2 C_{55}]\{\eta_{xxx}, \eta_{yyy}, \eta_{xxy}, \eta_{xyy}, \eta_{xzz}, \eta_{yzz}\}$$

$$\{\tau_{zzz}, \tau_{xxz}, \tau_{yyz}, \tau_{xyz}\} = [2l_2^2 C_{55}]\{\eta_{333}, \eta_{113}, \eta_{223}, \eta_{123}\}$$

where

$$Q_{11}^{SUC} = C_{11} - \frac{C_{13}^2}{C_{33}} \quad , \quad Q_{12}^{SUC} = Q_{21}^{SUC} = C_{12} - \frac{C_{13}C_{23}}{C_{33}}$$

$$Q_{22}^{SUC} = C_{22} - \frac{C_{23}^2}{C_{33}} \quad , \quad Q_{44}^{SUC} = Q_{55}^{SUC} = Q_{66}^{SUC} = C_{55} \tag{21}$$

and l_0, l_1 and l_2 are the small scale parameters attributed to the MSGT-based gradient tensors.

It should be pointed out that the values of stiffness parameters (C_{ij}) are extracted for the considered FFRC microplates with the aid of the developed SUC model in the previous section, corresponding to various GP and CNT volume fractions as well as different thicknesses and stiffness of the interphase region.

Furthermore, the Dirichlet boundary conditions relevant to the exploited displacement variables are prescribed in a straight route at the boundary control points alike the finite element approach.

The allocated expressions for the clamped FFRC microplate can be written as:

$$v = w = \frac{\partial w}{\partial x} = \psi_x = \psi_y = 0 \qquad at \;\; x = 0, L_1 \tag{22a}$$

$$u = w = \frac{\partial w}{\partial y} = \psi_x = \psi_y = 0 \qquad at \;\; y = 0, L_2 \tag{22b}$$

The allocated expressions for the simply supported FFRC microplate can be written as:

$$v = w = \psi_y = 0 \qquad at \;\; x = 0, L_1 \tag{23a}$$

$$u = w = \psi_x = 0 \qquad at \;\; y = 0, L_2 \tag{23b}$$

Isogeometric analysis is a numerical method that integrates the finite element analysis with computer-aided design (CAD) tools, aiming to bridge the gap between geometric modeling and simulation. So, it allows for the direct use of the exact CAD representation in simulations without the need for meshing. Due to its several advantages including exact representation of an arbitrary geometry, unified framework for geometry and analysis, higher-order continuity, and significant reduction in computational cost, the isogeometric analysis has been exploited in various structural behaviors studies in recent years [69-84].

Thus, by employing isogeometric meshing with cubic elements, as shown in Figure 7, the two-dimensional domain under exploration in this study leads to two distinct knot vectors in a non-reducing scheme, corresponding to each direction as follows

$$\mathbb{A}(\xi) = \left\{ \begin{matrix} \xi_1 \\ \xi_2 \\ \xi_3 \\ \vdots \\ \xi_{m+p+1} \end{matrix} \right\}^T \qquad \xi_{i+1} \geq \xi_i \;\; and \; 1 < i < m + p + 1 \tag{24a}$$

$$\mathbb{B}(\xi) = \begin{Bmatrix} \zeta_1 \\ \zeta_2 \\ \zeta_3 \\ \vdots \\ \zeta_{n+q+1} \end{Bmatrix}^T \qquad \zeta_{i+1} \geq \zeta_i \ \ and \ 1 < i < n+q+1 \tag{24b}$$

Here, m and n represent the number of B-spline basis functions in the ξ and ζ directions, respectively, corresponding to the orders p and q. Additionally, each knot i_{th} used in the numerical model is picked out within the determined spans of $0 \leq \xi_i \leq 1$ and $0 \leq \zeta_i \leq 1$. Subsequently, appraising the Cox-de Boor algorithm, the mathematical expressions for the engaged basis functions can be written as

$$X_{i,0}(\xi) = \begin{cases} 1 & \xi_i \leq \xi < \xi_{i+1} \\ 0 & otherwise \end{cases}, \quad X_{i,p}(\xi) = \left(\frac{\xi - \xi_i}{\xi_{i+p} - \xi_i}\right) X_{i,p-1}(\xi) + \left(\frac{\xi_{i+p+1} - \xi}{\xi_{i+p+1} - \xi_{i+1}}\right) X_{i+1,p-1}(\xi)$$

$$Y_{i,0}(\zeta) = \begin{cases} 1 & \zeta_i \leq \zeta < \zeta_{i+1} \\ 0 & otherwise \end{cases}, \quad Y_{i,q}(\zeta) = \left(\frac{\zeta - \zeta_i}{\zeta_{i+q} - \zeta_i}\right) Y_{i,q-1}(\zeta) + \left(\frac{\zeta_{i+q+1} - \zeta}{\zeta_{i+q+1} - \zeta_{i+1}}\right) Y_{i+1,q-1}(\zeta) \tag{25}$$

On this account, via practicing pertinent tensor product, the allocated B-spline basis functions for the modeled FFRC microplates are expressed as below

$$\mathfrak{B}_i(\xi, \zeta) = \left(X_{i,p}(\xi) Y_{j,q}(\zeta) \mathbb{W}_{i,j}\right) / \left(\sum_{i=1}^{m} \sum_{j=1}^{n} X_{i,p}(\xi) Y_{j,q}(\zeta) \mathbb{W}_{i,j}\right) \tag{26}$$

where $\mathbb{W}_{i,j}$ refers to the weighting constants relevant to the exploited basis function.

It should be pointed out that in the employed isogeometric framework, the geometry of the FFRC microplates is described using NURBS basis functions. As a consequence, in contrast to the conventional finite element approach, the control points in the isogeometric analysis do not necessarily coincide with the physical points of the domain. However, the B-spline mapping ensures that the resulting geometry represents the exact CAD model with no geometrical approximation error. Refinement of the computational model is achieved through knot-insertion and order-elevation procedures, which increase the number of control points and enhance the approximation accuracy while keeping the physical geometry unchanged. Therefore, the non-coincidence of control and physical points does not affect the accuracy of the modeled geometry. For the plate structures considered in the current exploration, the physical boundaries coincide with corresponding boundary control points. In this regard, Dirichlet boundary conditions were therefore prescribed directly on these boundary control points in the same manner as in the finite element method, ensuring that constraints are applied on the exact physical boundary.

With the aid of the introduced basis function, the CL-based strain tensor of an exponential shear flexible FFRC microplate can be conveyed in the succeeding discretized configuration

$$\boldsymbol{\varepsilon}_{\mathbf{b}} = \boldsymbol{\varepsilon}_{\mathbf{b}}^{\boldsymbol{L}} + \boldsymbol{\varepsilon}_{\mathbf{b}}^{\boldsymbol{NL}} = \sum_{i=1}^{m\times n} \boldsymbol{\mathcal{S}}_{\boldsymbol{Lb}}^{\boldsymbol{i}} \mathbb{X}^{i} + \sum_{i=1}^{m\times n} \frac{1}{2} \boldsymbol{\mathcal{S}}_{\boldsymbol{NLb}}^{\boldsymbol{i}} \mathbb{X}^{i} \quad , \quad \boldsymbol{\varepsilon}_{\mathbf{s}} = \sum_{\boldsymbol{i=1}}^{\boldsymbol{m\times n}} \boldsymbol{\mathcal{S}}_{\boldsymbol{s}}^{\boldsymbol{i}} \mathbb{X}^{\boldsymbol{i}} \tag{27}$$

in which $\boldsymbol{\mathcal{S}}_{\boldsymbol{Lb}}^{\boldsymbol{i}}, \boldsymbol{\mathcal{S}}_{\boldsymbol{NLb}}^{\boldsymbol{i}}, \boldsymbol{\mathcal{S}}_{\boldsymbol{s}}^{\boldsymbol{i}}$ and $\mathbb{X}^{\boldsymbol{i}}$ are defined in Appendix A.

In a similar way, by utilizing the introduced basis function, the MSGT-based rotation gradient tensor of an exponential shear flexible FFRC microplate can be conveyed in the succeeding discretized configuration

$$\boldsymbol{\chi}_{\mathbf{b}} = \sum_{\boldsymbol{i=1}}^{\boldsymbol{m\times n}} \boldsymbol{\mathcal{G}}_{\boldsymbol{b}}^{\boldsymbol{i}} \mathbb{X}^{\boldsymbol{i}} \quad , \quad \boldsymbol{\chi}_{\boldsymbol{s}} = \sum_{\boldsymbol{i=1}}^{\boldsymbol{m\times n}} \boldsymbol{\mathcal{G}}_{\boldsymbol{s}}^{\boldsymbol{i}} \mathbb{X}^{\boldsymbol{i}} \tag{28}$$

where $\boldsymbol{\mathcal{G}}_{\boldsymbol{b}}^{\boldsymbol{i}}$ and $\boldsymbol{\mathcal{G}}_{\boldsymbol{s}}^{\boldsymbol{i}}$ are introduced in Appendix A.

Likewise, by utilizing the introduced basis function, the MSGT-based dilatation gradient tensor of an exponential shear flexible FFRC microplate can be conveyed in the succeeding discretized configuration

$$\boldsymbol{\varsigma}_{\boldsymbol{b}} = \boldsymbol{\varsigma}_{\boldsymbol{b}}^{\boldsymbol{L}} + \boldsymbol{\varsigma}_{\boldsymbol{b}}^{\boldsymbol{NL}} = \sum_{\boldsymbol{i=1}}^{\boldsymbol{m\times n}} \boldsymbol{\mathcal{J}}_{\boldsymbol{Lb}}^{\boldsymbol{i}} \mathbb{X}^{\boldsymbol{i}} + \sum_{\boldsymbol{i=1}}^{\boldsymbol{m\times n}} \boldsymbol{\mathcal{J}}_{\boldsymbol{NLb}}^{\boldsymbol{i}} \mathbb{X}^{\boldsymbol{i}} \quad , \quad \boldsymbol{\varsigma}_{\boldsymbol{s}} = \sum_{\boldsymbol{i=1}}^{\boldsymbol{m\times n}} \boldsymbol{\mathcal{J}}_{\boldsymbol{s}}^{\boldsymbol{i}} \mathbb{X}^{\boldsymbol{i}} \tag{29}$$

in which $\boldsymbol{\mathcal{J}}_{\boldsymbol{Lb}}^{\boldsymbol{i}}, \boldsymbol{\mathcal{J}}_{\boldsymbol{NLb}}^{\boldsymbol{i}}$ and $\boldsymbol{\mathcal{J}}_{\boldsymbol{s}}^{\boldsymbol{i}}$ are formulated in Appendix A.

Likewise, by utilizing the introduced basis function, the MSGT-based deviatoric stretch gradient tensor of an exponential shear flexible FFRC microplate can be conveyed in the succeeding discretized configuration

$$\boldsymbol{\eta}_{\mathbf{b}} = \boldsymbol{\eta}_{\mathbf{b}}^{\boldsymbol{L}} + \boldsymbol{\eta}_{\mathbf{b}}^{\boldsymbol{NL}} = \sum_{i=1}^{m\times n} \boldsymbol{\mathcal{Y}}_{\boldsymbol{Lb}}^{\boldsymbol{i}} \mathbb{X}^{i} + \sum_{i=1}^{m\times n} \boldsymbol{\mathcal{Y}}_{\boldsymbol{NLb}}^{\boldsymbol{i}} \mathbb{X}^{i} \quad , \quad \boldsymbol{\eta}_{\mathbf{s}} = \sum_{\boldsymbol{i=1}}^{\boldsymbol{m\times n}} \boldsymbol{\mathcal{Y}}_{\boldsymbol{s}}^{\boldsymbol{i}} \mathbb{X}^{\boldsymbol{i}} \tag{30}$$

where $\boldsymbol{\mathcal{Y}}_{\boldsymbol{Lb}}^{\boldsymbol{i}}, \boldsymbol{\mathcal{Y}}_{\boldsymbol{NLb}}^{\boldsymbol{i}}$ and $\boldsymbol{\mathcal{Y}}_{\boldsymbol{s}}^{\boldsymbol{i}}$ are defined in Appendix A.

Finally, with the aid of the variation principle, the discretized conformation of the nonlinear differential equations allocated to the nonlinear stability analysis of axially compressed FFRC microplates is derived as follows

$$\sum_{i=1}^{m\times n} \left(\boldsymbol{\mathcal{K}}^{\boldsymbol{i}}(\mathbb{X}) - \boldsymbol{\mathcal{P}}_{\boldsymbol{cr}} \boldsymbol{\mathcal{K}}_{\boldsymbol{G}}^{\boldsymbol{i}}\right) \mathbb{X}^{i} = 0 \tag{31}$$

where $\boldsymbol{\mathcal{P}}_{\boldsymbol{cr}}$ mentions the critical buckling value of the applied axial compressive load vector, and $\boldsymbol{\mathcal{K}}^{\boldsymbol{i}}(\mathbb{X})$ refers to the global stiffness matrix of the MSGT-based FFRC microplate comprising the linear and nonlinear fragments as below

$$\sum_{i=1}^{m\times n}\boldsymbol{\mathcal{K}}_{L}^{i}(\mathbb{X})=\sum_{i=1}^{m\times n}\left[\int_{\Omega}\left\{\left(\boldsymbol{\mathcal{S}}_{\boldsymbol{Lb}}^{i}\right)^{T}\mathbb{C}_{\boldsymbol{1b}}\boldsymbol{\mathcal{S}}_{\boldsymbol{Lb}}^{i}+\left(\boldsymbol{\mathcal{S}}_{\boldsymbol{s}}^{i}\right)^{T}\mathbb{C}_{\boldsymbol{1s}}\boldsymbol{\mathcal{S}}_{\boldsymbol{s}}^{i}+\left(\boldsymbol{\mathcal{G}}_{\boldsymbol{b}}^{i}\right)^{T}\mathbb{C}_{\boldsymbol{2b}}\boldsymbol{\mathcal{G}}_{\boldsymbol{b}}^{i}+\left(\boldsymbol{\mathcal{G}}_{\boldsymbol{s}}^{i}\right)^{T}\mathbb{C}_{\boldsymbol{2s}}\boldsymbol{\mathcal{G}}_{\boldsymbol{s}}^{i}+\left(\boldsymbol{\mathcal{J}}_{\boldsymbol{Lb}}^{i}\right)^{T}\mathbb{C}_{\boldsymbol{3b}}\boldsymbol{\mathcal{J}}_{\boldsymbol{Lb}}^{i}\right.\right.$$
$$\left.\left.+\left(\boldsymbol{\mathcal{J}}_{\boldsymbol{s}}^{i}\right)^{T}\mathbb{C}_{\boldsymbol{3s}}\boldsymbol{\mathcal{J}}_{\boldsymbol{s}}^{i}+\left(\boldsymbol{\mathcal{Y}}_{\boldsymbol{Lb}}^{i}\right)^{T}\mathbb{C}_{\boldsymbol{4b}}\boldsymbol{\mathcal{Y}}_{\boldsymbol{Lb}}^{i}+\left(\boldsymbol{\mathcal{Y}}_{\boldsymbol{s}}^{i}\right)^{T}\mathbb{C}_{\boldsymbol{4s}}\boldsymbol{\mathcal{Y}}_{\boldsymbol{s}}^{i}\right\}d\Omega\right] \tag{32a}$$

$$\sum_{i=1}^{m\times n}\boldsymbol{\mathcal{K}}_{NL}^{i}(\mathbb{X})=\sum_{i=1}^{m\times n}\left[\int_{\Omega}\left\{\frac{1}{2}\left(\boldsymbol{\mathcal{S}}_{\boldsymbol{Lb}}^{i}\right)^{T}\mathbb{C}_{\boldsymbol{1b}}\boldsymbol{\mathcal{S}}_{\boldsymbol{NLb}}^{i}+\left(\boldsymbol{\mathcal{S}}_{\boldsymbol{NLb}}^{i}\right)^{T}\mathbb{C}_{\boldsymbol{1b}}\boldsymbol{\mathcal{S}}_{\boldsymbol{Lb}}^{i}+\frac{1}{2}\left(\boldsymbol{\mathcal{S}}_{\boldsymbol{NLb}}^{i}\right)^{T}\mathbb{C}_{\boldsymbol{1b}}\boldsymbol{\mathcal{S}}_{\boldsymbol{NLb}}^{i}+\left(\boldsymbol{\mathcal{J}}_{\boldsymbol{Lb}}^{i}\right)^{T}\mathbb{C}_{\boldsymbol{3b}}\boldsymbol{\mathcal{J}}_{\boldsymbol{NLb}}^{i}\right.\right.$$
$$+\left(\boldsymbol{\mathcal{J}}_{\boldsymbol{NLb}}^{i}\right)^{T}\mathbb{C}_{\boldsymbol{3b}}\boldsymbol{\mathcal{J}}_{\boldsymbol{Lb}}^{i}+\left(\boldsymbol{\mathcal{J}}_{\boldsymbol{NLb}}^{i}\right)^{T}\mathbb{C}_{\boldsymbol{3b}}\boldsymbol{\mathcal{J}}_{\boldsymbol{NLb}}^{i}+\left(\boldsymbol{\mathcal{Y}}_{\boldsymbol{Lb}}^{i}\right)^{T}\mathbb{C}_{\boldsymbol{4b}}\boldsymbol{\mathcal{Y}}_{\boldsymbol{NLb}}^{i}+\left(\boldsymbol{\mathcal{Y}}_{\boldsymbol{NLb}}^{i}\right)^{T}\mathbb{C}_{\boldsymbol{4b}}\boldsymbol{\mathcal{Y}}_{\boldsymbol{Lb}}^{i}$$
$$\left.\left.+\left(\boldsymbol{\mathcal{Y}}_{\boldsymbol{NLb}}^{i}\right)^{T}\mathbb{C}_{\boldsymbol{4b}}\boldsymbol{\mathcal{Y}}_{\boldsymbol{NLb}}^{i}\right\}d\Omega\right] \tag{32b}$$

$$\sum_{i=1}^{m\times n}\boldsymbol{\mathcal{K}}_{G}^{i}=\sum_{i=1}^{m\times n}\left[\int_{\Omega}\left\{\left(\boldsymbol{\mathcal{S}}_{\boldsymbol{G}}^{i}\right)^{\boldsymbol{T}}\boldsymbol{\mathcal{N}}\boldsymbol{\mathcal{S}}_{\boldsymbol{G}}^{i}\right\}d\Omega\right] \tag{32c}$$

in which $\boldsymbol{\mathcal{N}}=\begin{bmatrix}\mathcal{N}_{xx} & \mathcal{N}_{xy}\\ \mathcal{N}_{xy} & \mathcal{N}_{yy}\end{bmatrix}$ stands for the stress resultant linear approximated derivative (LAD) matrix.

4. Numerical results and discussions

In this section, using the unified isogeometric-SUC model, the CL- and MSGT-based nonlinear stability performances of FFRC microplates are demonstrated for different boundary conditions, geometries, and FFRC constitutions. The dimensions are assumed: $h=30\,\mu m$ and $L_1=L_2=L=50h$. Furthermore, in the scrutinized size-dependent model, the quantities attributed to the small-scale parameters are typically chosen based on the smallest characteristic dimension of the structure. Herein, the FFRC microplates have a thickness of $30\,\mu m$, which represents their smallest dimension. Accordingly, the internal length scale parameters relevant to the MSGT-based computational model are selected within the range of $30\pm 10\,\mu m$. Additionally, since the nonlinear stability behavior of FFRC microplates involves coupled bending-stretching mechanisms, all three gradient tensors act concurrently and their effects cannot be meaningfully separated without losing the physical integrity of the model. Therefore, the present study concentrates on the combined contribution of these microstructural-dependent strain gradient tensors, which together produce the observed enhancement in stiffness and stability attributable to microsize effects.

In Figure 8, a flowchart representing the summary of the numerical solving scenario allocated to the developed unified SUC-IGA computational model is illustrated. Because the scrutinized mathematical formulations attributed to the proposed unified computational model are given in Cartesian coordinate system, the considered geometries associated with the presented numerical outcomes are within the framework of rectangular microplates.

Primarily, the validity of the advanced MSGT-based size-dependent numerical model is surveyed. With this in mind, by ignoring the terms allocated to the geometrical nonlinearity, the critical axial buckling loads of a simply supported functionally graded composite microplate are calculated corresponding to diverse values of the MSGT-based small-scale parameters. As tabulated in Table 2, the outcomes of the current numerical solution strategy are compared with those communicated by Zhang et al. [14] using an analytical approach. A very good consensus between the two reported results is observed which acknowledges the accuracy of the present model.

In another comparison, after ignoring the expressions assigned to the MSGT, the critical buckling loads of uniformly CNT-reinforced nanocomposite plates with various aspect ratios and corresponding to different CNT volume fractions are obtained and compared with those reported by Mehrabadi et al. [85] using an exact solution strategy. As shown in Table 3, excellent agreement between the two results is observed, which supports the validity of the established micromechanics model.

Furthermore, to enable a comparative investigation of the nonlinear stability behavior of plates with complex geometries, the normalized load-deflection stability responses of rectangular plates containing a square central cutout and subjected to biaxial compressive loading are evaluated. The study considers functionally graded nanocomposite porous rectangular plates with either fully simply supported or fully clamped boundary conditions applied along all external and cutout edges. The obtained results are then benchmarked against those reported by Ansari et al. [85] that employed a finite element-based numerical approach. As shown in Figure 9, the close agreement between the two sets of results further demonstrates the accuracy and reliability of the present numerical solution methodology.

Figures 10 and 11 in order display the normalized load-deflection and load-shortening nonlinear stability features of the FFRC microplates in the absence of a central cutout obtained by the CL-based and MSGT-based isogeometric-SUC models. The plots are traced for two reinforcing patterns: GF-epoxy (with no radially aligned CNTs) and CNT-GF-Epoxy (FFRC kind of reinforcement). It can be found that by taking the microstructural gradient tensors into consideration, the critical buckling load besides the critical shortening enhance resulting in higher load-bearing as well as shortening-bearing potentialities of the FFRC microplates. Moreover, it is seen that due to having more restrictive boundary conditions, the clamped microplates exhibit larger overall stiffness, leading to higher critical buckling and postbuckling loads compared to simply supported ones. In addition, clamped edges restrict the lateral rotation more effectively than simply supported ones, which intensifies the nonlinear coupling between bending and membrane stresses. This enhanced interaction leads to a difference in the slope of the corresponding equilibrium paths. Accordingly, by taking $l_0 = l_1 = l_2 = 40\,\mu m$ into account, in the case of GF-Epoxy reinforcing pattern, the normalized critical buckling load increases from 0.3932 to 0.4519 $(+14.93\%)$ for the simply supported microplate and from 0.9601 to 1.1036 $(+14.95\%)$ for the clamped microplate.

Also, the normalized critical shortening intensifies from 0.0512 to 0.0589 (+15.04%) for the simply supported microplate and from 0.1251 to 0.1438 (+14.95%) for the clamped microplate. On the other hand, in the case of CNT-GF-Epoxy reinforcing pattern, the normalized critical buckling load increases from 0.4331 to 0.4978 (+14.94%) for the simply supported microplate and from 1.0576 to 1.2156 (+14.94%) for the clamped microplate. Also, the normalized critical shortening intensifies from 0.0557 to 0.0641 (+15.08%) for the simply supported microplate and from 0.1295 to 0.1564 (+20.77%) for the clamped microplate.

In Figures 12 and 13 together with Tables 4 and 5, the influence of GF volume fraction on the normalized load-deflection and load-shortening nonlinear stability features of the FFRC microplates in the absence of a central cutout obtained by the CL-based and MSGT-based isogeometric-SUC models is depicted. It is disclosed that a higher GF volume fraction results in a considerable increment in the value of the critical buckling loads of FFRC microplates. However, its influence on the shortening-bearing potentiality is negligible. From a micromechanical standpoint, increasing the volume fraction of the stiff glass nanofibers enhances both the axial and transverse stiffness of the microplate and, more importantly, significantly raises its effective flexural rigidity due to their dominant contribution to the section's moment of inertia. Because the critical buckling load is principally controlled by bending stiffness, this directly explains the pronounced increase in buckling resistance with higher GF content. Moreover, a greater proportion of glass fibers promotes more efficient load transfer among the composite constituents and restricts matrix deformation, thereby reducing shear compliance and postponing the onset of instability. In this regard, through increasing the GF volume fraction from 30% to 70%, in the case of CL-based model, the normalized critical buckling load enhances from 0.2820 to 0.5926 (+110.14%) for the simply supported microplate and from 0.6887 to 1.4471 (+110.12%) for the clamped microplate. Also, the normalized critical shortening intensifies from 0.0558 to 0.0567 (+1.61%) for the simply supported microplate and from 0.1362 to 0.1384 (+1.62%) for the clamped microplate. On the other hand, in the case of MSGT-based model with $l_0 = l_1 = l_2 = 40\,\mu m$, the normalized critical buckling load increases from 0.3242 to 0.6811 (+110.09%) for the simply supported microplate and from 0.7916 to 1.6633 (+110.12%) for the clamped microplate. Also, the normalized critical shortening intensifies from 0.0641 to 0.0651 (+1.56%) for the simply supported microplate and from 0.1566 to 0.1591 (+1.60%) for the clamped microplate.

Figures 14 and 15 together with Tables 6 and 7 demonstrate the influence of CNT volume fraction on the normalized load-deflection and load-shortening nonlinear stability features of the FFRC microplates in the absence of a central cutout obtained by the CL-based and MSGT-based isogeometric-SUC models. It can be observed that a higher CNT volume fraction results in an appreciable increment in the value of the critical shortening of FFRC microplates. The results demonstrate that increasing the CNT volume

fraction leads to a rise in both the critical buckling load and the critical shortening of FFRC microplates. This trend originates from the micromechanical role of CNTs as effective nanoscale reinforcements of the polymer matrix surrounding the glass fibers. The CNTs enhance the stiffness of the matrix phase and significantly improve load transfer capability due to their high modulus and efficient mechanical interaction with the surrounding matrix-interphase system. Consequently, the effective nanocomposite stiffness participating in global bending increases, which elevates the load-bearing capacity. At the same time, CNT reinforcement improves the resistance to in-plane distortion and stabilizes the microstructure in the postbuckling regime, thereby enhancing the shortening-bearing capacity. In other words, CNTs contribute both to the flexural stiffness prior to instability and to the membrane stiffening after buckling, leading to consistent improvements in both bifurcation behavior and nonlinear stability performance. Accordingly, through increasing the CNT volume fraction from 0.25% to its maximum quantity, in the case of CL-based model, the normalized critical buckling load enhances from 0.4021 to 0.4331 (+7.71%) for the simply supported microplate and from 0.9818 to 1.0576 (+7.72%) for the clamped microplate. Also, the normalized critical shortening intensifies from 0.0523 to 0.0557 (+6.50%) for the simply supported microplate and from 0.1277 to 0.1361 (+6.58%) for the clamped microplate. On the other hand, in the case of MSGT-based model with $l_0 = l_1 = l_2 = 40\,\mu m$, the normalized critical buckling load increases from 0.4621 to 0.4978 (+7.73%) for the simply supported microplate and from 1.1285 to 1.2156 (+7.72%) for the clamped microplate. Also, the normalized critical shortening intensifies from 0.0601 to 0.0641 (+6.66%) for the simply supported microplate and from 0.1468 to 0.1564 (+6.54%) for the clamped microplate.

In Figures 16 and 17 together with Tables 8 and 9, the influence of interphase thickness (IT) value on the normalized load-deflection and load-shortening nonlinear stability features of the FFRC microplates in the absence of a central cutout obtained by the CL-based and MSGT-based isogeometric-SUC models is depicted. It is found that the interphase thickness plays an essential role in the nonlinear stability characteristics of FFRC microplates, especially when its thickness becomes large. A thicker interphase improves the quality of mechanical load transfer between CNTs and the surrounding matrix by reducing interfacial compliance and mitigating shear-lag effects. This results in more effective stress distribution around the fuzzy fiber architecture, suppression of local stress concentrations, and enhanced utilization of CNT reinforcement. From a structural standpoint, this translates to enhanced effective stiffness and energy absorption capacity, improving both buckling resistance and postbuckling stability. In particular, as the interphase becomes more mechanically active, the nanocomposite behaves less like a weakly bonded inclusion system and more like an integrated multi-phase material, which explains the appreciable increase in load-bearing and shortening-bearing capacity observed in the results. In this regard, through increasing the IT value from $0.10\,nm$ to $0.78\,nm$, in the case of CL-based model, the normalized critical

buckling load enhances from 0.4164 to 0.4893 (+17.51%) for the simply supported microplate and from 1.0168 to 1.1950 (+17.53%) for the clamped microplate. Also, the normalized critical shortening intensifies from 0.0547 to 0.0579 (+5.85%) for the simply supported microplate and from 0.1336 to 0.1415 (+5.91%) for the clamped microplate. On the other hand, in the case of MSGT-based model with $l_0 = l_1 = l_2 = 40\,\mu m$, the normalized critical buckling load increases from 0.4786 to 0.5625 (+17.53%) for the simply supported microplate and from 1.1687 to 1.3735 (+17.52%) for the clamped microplate. Also, the normalized critical shortening intensifies from 0.0629 to 0.0666 (+5.88%) for the simply supported microplate and from 0.1535 to 0.1626 (+5.93%) for the clamped microplate.

Figures 18 and 19 together with Tables 10 and 11 demonstrate the influence of interphase stiffness (IS) value on the normalized load-deflection and load-shortening nonlinear stability features of the FFRC microplates in the absence of a central cutout obtained by the CL-based and MSGT-based isogeometric-SUC models. It is revealed that a higher interphase stiffness results in an appreciable increment in the both load-bearing as well as shortening-bearing potentialities of the FFRC microplates, so it is necessary to take it into account. In other words, it is observed again that with increasing mechanical contribution of the interphase, the nanocomposite evolves from a loosely bonded inclusion structure to a mechanically unified multi-phase medium, which leads to the observed improvement in both load-carrying and shortening capacity. Accordingly, through increasing the IS value from 4.34 GPa to 434 GPa, in the case of CL-based model, the normalized critical buckling load enhances from 0.4129 to 0.4382 (+6.13%) for the simply supported microplate and from 1.0083 to 1.0701 (+6.13%) for the clamped microplate. Also, the normalized critical shortening intensifies from 0.0545 to 0.0563 (+3.30%) for the simply supported microplate and from 0.1330 to 0.1374 (+3.31%) for the clamped microplate. On the other hand, in the case of MSGT-based model with $l_0 = l_1 = l_2 = 40\,\mu m$, the normalized critical buckling load increases from 0.4746 to 0.5037 (+6.13%) for the simply supported microplate and from 1.1590 to 1.2300 (+6.12%) for the clamped microplate. Also, the normalized critical shortening intensifies from 0.0626 to 0.0647 (+3.35%) for the simply supported microplate and from 0.1528 to 0.1579 (+3.34%) for the clamped microplate.

In Figures 20 and 21 together with Figures 22 and 23, the influence of exciting, respectively, a central circular cutout and a central square cutout on the normalized load-deflection and load-shortening nonlinear stability features of the FFRC microplates obtained by the MSGT-based isogeometric-SUC model is portrayed corresponding to various cases with different IT and IS values. It is revealed that by making a central cutout in the geometry of FFRC microplates, the both load-bearing and shortening-bearing of them reduce at the critical buckling point due to the decrease in the microplate's flexural stiffness as well as the localized stress redistribution around the cutout. Also, it can be deduced that the postbuckling response remains stable attributed to all values of IT and IS, with a smooth nonlinear rise in

load-carrying capacity as the lateral deflection increases, indicating the dominance of membrane stresses through progressing to deep postbuckling regime. It is because of the membrane energy dependency of the plate mainly on the in-plane stiffness as well as the geometric stretching. This observation represents a matching trend reported theoretical and experimental by Ritchie and Rhodes [87] for the classical plate study. Consistently, by changing the IT value from $0.10\,nm$ to $0.78\,nm$ and considering IS$= 43.4\,GPa$, the normalized critical buckling load enhances from 0.4403 to 0.5175, from 0.4164 to 0.4893 in order for existing circular ($d = 0.1L$) and square ($a = 0.1L$) cutouts in the simply supported FFRC microplate, and from 1.0752 to 1.2636, from 1.0168 to 1.1950 in order for existing circular ($d = 0.1L$) and square ($a = 0.1L$) cutouts in the clamped FFRC microplate. On the other hand, by changing the IS value from $4.34\,GPa$ to $434\,GPa$ and considering IT$= 0.39\,nm$, the normalized critical buckling load enhances from 0.4366 to 0.4634, from 0.4129 to 0.4382 in order for existing circular ($d = 0.1L$) and square ($a = 0.1L$) cutouts in the simply supported FFRC microplate, and from 1.0663 to 1.1316, from 1.0083 to 1.0701 in order for existing circular ($d = 0.1L$) and square ($a = 0.1L$) cutouts in the clamped FFRC microplate.

5. Concluding remarks

In the present investigation, via a consistent integration of the micromechanics approach and the numerical solution methodology, a unified isogeometric-SUC computational framework was established to analyze numerically the nonlinear stability response of FFRC microplates having an arbitrary geometry while explicitly accounting for the interphase region. In order to contemplate the size dependency, the isogeometric-SUC model of FFRC microplates were formulated based upon the MSGT. So, this unified model provided a physically transparent pathway from micromechanical properties to microstructural design variables. The findings obtained in the current study particularly clarified the combined effect of CNT reinforcement, interphase characteristics, and strain gradient size dependency in the nonlinear stability regime, offering new insight that can support rational design and optimization of FFRC microscale structural elements.

It was deduced that by taking the microstructural gradient tensors into consideration, the critical buckling load besides the critical shortening enhance resulting in higher load-bearing as well as shortening-bearing potentialities of the FFRC microplates. Also, it was illustrated that a higher GF volume fraction results in a considerable increment in the value of the critical buckling loads of FFRC microplates. However, its influence on the shortening-bearing potentiality is negligible. Accordingly,

through increasing the CNT volume fraction from 0.25% to its maximum quantity, in the case of CL-based model, the normalized critical buckling load enhances from 0.4021 to 0.4331 (+7.71%) for the simply supported microplate and from 0.9818 to 1.0576 (+7.72%) for the clamped microplate. Also, the normalized critical shortening intensifies from 0.0523 to 0.0557 (+6.50%) for the simply supported microplate and from 0.1277 to 0.1361 (+6.58%) for the clamped microplate. On the other hand, in the case of MSGT-based model with $l_0 = l_1 = l_2 = 40\,\mu m$, the normalized critical buckling load increases from 0.4621 to 0.4978 (+7.73%) for the simply supported microplate and from 1.1285 to 1.2156 (+7.72%) for the clamped microplate. Also, the normalized critical shortening intensifies from 0.0601 to 0.0641 (+6.66%) for the simply supported microplate and from 0.1468 to 0.1564 (+6.54%) for the clamped microplate.

Furthermore, it was found that a higher CNT volume fraction results in an appreciable increment in the value of the critical shortening of FFRC microplates. However, its influence on the load-bearing potentiality is not so significant. Additionally, it was seen that a higher interphase stiffness results in an appreciable increment in the both load-bearing as well as shortening-bearing potentialities of the FFRC microplates, so it is necessary to take it into account. Moreover, it was seen that by making a central cutout in the geometry of FFRC microplates, the both load-bearing and shortening-bearing of them initially reduce at the critical buckling point, but by progressing to more deep postbuckling region, a physical consequence of the nonlinear transition from bending-dominated to membrane-dominated deformation was observed.

Appendix A

$$\boldsymbol{\chi_b} = \begin{Bmatrix} \chi_{xx} \\ \chi_{yy} \\ \chi_{zz} \\ \chi_{xy} \end{Bmatrix} = \begin{Bmatrix} \dfrac{\partial^2 w}{\partial x \partial y} \\ -\dfrac{\partial^2 w}{\partial x \partial y} \\ 0 \\ \dfrac{1}{2}\left(\dfrac{\partial^2 w}{\partial y^2} - \dfrac{\partial^2 w}{\partial x^2}\right) \end{Bmatrix} + e^{-\frac{2z^2}{h^2}} \begin{Bmatrix} -\dfrac{1}{2}\dfrac{\partial \psi_y}{\partial x} \\ \dfrac{1}{2}\dfrac{\partial \psi_x}{\partial y} \\ \dfrac{1}{2}\left(\dfrac{\partial \psi_y}{\partial x} - \dfrac{\partial \psi_x}{\partial y}\right) \\ \dfrac{1}{2}\left(\dfrac{\partial \psi_x}{\partial x} - \dfrac{\partial \psi_y}{\partial y}\right) \end{Bmatrix} + \frac{4z^2}{h^2} e^{-\frac{2z^2}{h^2}} \begin{Bmatrix} \dfrac{1}{2}\dfrac{\partial \psi_y}{\partial x} \\ -\dfrac{1}{2}\dfrac{\partial \psi_x}{\partial y} \\ \dfrac{1}{2}\left(\dfrac{\partial \psi_x}{\partial y} - \dfrac{\partial \psi_y}{\partial x}\right) \\ \dfrac{1}{2}\left(\dfrac{\partial \psi_y}{\partial y} - \dfrac{\partial \psi_x}{\partial x}\right) \end{Bmatrix}$$

$$= \boldsymbol{\chi}_{\mathbf{b}}^{(\mathbf{0})} + e^{-\frac{2z^2}{h^2}} \boldsymbol{\chi}_{\mathbf{b}}^{(\mathbf{1})} + \frac{4z^2}{h^2} e^{-\frac{2z^2}{h^2}} \boldsymbol{\chi}_{\mathbf{b}}^{(\mathbf{2})} \qquad (A1)$$

$$\boldsymbol{\chi_s} = \begin{Bmatrix} \chi_{xz} \\ \chi_{yz} \end{Bmatrix} = \begin{Bmatrix} \frac{1}{4}\left(\frac{\partial^2 v}{\partial x^2} - \frac{\partial^2 u}{\partial x \partial y}\right) \\ \frac{1}{4}\left(\frac{\partial^2 v}{\partial x \partial y} - \frac{\partial^2 u}{\partial y^2}\right) \end{Bmatrix} + \frac{z}{4} e^{-\frac{2z^2}{h^2}} \begin{Bmatrix} \frac{\partial^2 \psi_y}{\partial x^2} - \frac{\partial^2 \psi_x}{\partial x \partial y} \\ \frac{\partial^2 \psi_y}{\partial x \partial y} - \frac{\partial^2 \psi_x}{\partial y^2} \end{Bmatrix} + \frac{3z}{h^2} e^{-\frac{2z^2}{h^2}} \begin{Bmatrix} \psi_y \\ -\psi_x \end{Bmatrix} + \frac{4z^3}{h^4} e^{-\frac{2z^2}{h^2}} \begin{Bmatrix} -\psi_y \\ \psi_x \end{Bmatrix}$$

$$= \boldsymbol{\chi_s^{(0)}} + \frac{z}{4} e^{-\frac{2z^2}{h^2}} \boldsymbol{\chi_s^{(1)}} + \frac{3z}{h^2} e^{-\frac{2z^2}{h^2}} \boldsymbol{\chi_s^{(2)}} + \frac{4z^3}{h^4} e^{-\frac{2z^2}{h^2}} \boldsymbol{\chi_s^{(3)}} \qquad (A2)$$

$$\boldsymbol{\varsigma_b} = \begin{Bmatrix} \varsigma_x \\ \varsigma_y \end{Bmatrix} = \begin{Bmatrix} \frac{\partial^2 u}{\partial x^2} + \frac{\partial^2 v}{\partial x \partial y} + \frac{\partial w}{\partial x}\frac{\partial^2 w}{\partial x^2} + \frac{\partial w}{\partial y}\frac{\partial^2 w}{\partial x \partial y} \\ \frac{\partial^2 u}{\partial x \partial y} + \frac{\partial^2 v}{\partial y^2} + \frac{\partial w}{\partial x}\frac{\partial^2 w}{\partial x \partial y} + \frac{\partial w}{\partial y}\frac{\partial^2 w}{\partial y^2} \end{Bmatrix} + z \begin{Bmatrix} -\frac{\partial^3 w}{\partial x^3} - \frac{\partial^3 w}{\partial x \partial y^2} \\ -\frac{\partial^3 w}{\partial x^2 \partial y} - \frac{\partial^3 w}{\partial y^3} \end{Bmatrix} + z e^{-\frac{2z^2}{h^2}} \begin{Bmatrix} \frac{\partial^2 \psi_x}{\partial x^2} + \frac{\partial^2 \psi_y}{\partial x \partial y} \\ \frac{\partial^2 \psi_x}{\partial x \partial y} + \frac{\partial^2 \psi_y}{\partial y^2} \end{Bmatrix}$$

$$= \boldsymbol{\varsigma_b^{(0)}} + z\boldsymbol{\varsigma_b^{(1)}} + z e^{-\frac{2z^2}{h^2}} \boldsymbol{\varsigma_b^{(2)}} \qquad (A3)$$

$$\boldsymbol{\varsigma_s} = \{\varsigma_z\} = \left\{ -\frac{\partial^2 w}{\partial x^2} - \frac{\partial^2 w}{\partial y^2} \right\} + e^{-\frac{2z^2}{h^2}} \left\{ \frac{\partial \psi_x}{\partial x} + \frac{\partial \psi_y}{\partial y} \right\} + \frac{4z^2}{h^2} e^{-\frac{2z^2}{h^2}} \left\{ -\frac{\partial \psi_x}{\partial x} - \frac{\partial \psi_y}{\partial y} \right\}$$

$$= \boldsymbol{\varsigma_s^{(0)}} + e^{-\frac{2z^2}{h^2}} \boldsymbol{\varsigma_s^{(1)}} + \frac{4z^2}{h^2} e^{-\frac{2z^2}{h^2}} \boldsymbol{\varsigma_s^{(2)}} \qquad (A4)$$

$$\boldsymbol{\eta}_{\mathbf{b}} = \begin{Bmatrix} \eta_{xxx} \\ \eta_{yyy} \\ \eta_{xxy} \\ \eta_{xyy} \\ \eta_{xzz} \\ \eta_{yzz} \end{Bmatrix} = \begin{Bmatrix} \frac{2}{5}\frac{\partial^2 u}{\partial x^2} - \frac{1}{5}\frac{\partial^2 u}{\partial y^2} - \frac{2}{5}\frac{\partial^2 v}{\partial x \partial y} + \frac{2}{5}\frac{\partial w}{\partial x}\frac{\partial^2 w}{\partial x^2} - \frac{1}{5}\frac{\partial w}{\partial x}\frac{\partial^2 w}{\partial y^2} - \frac{2}{5}\frac{\partial w}{\partial y}\frac{\partial^2 w}{\partial x \partial y} \\ -\frac{2}{5}\frac{\partial^2 u}{\partial x \partial y} - \frac{1}{5}\frac{\partial^2 v}{\partial x^2} + \frac{2}{5}\frac{\partial^2 v}{\partial y^2} - \frac{2}{5}\frac{\partial w}{\partial x}\frac{\partial^2 w}{\partial x \partial y} - \frac{1}{5}\frac{\partial w}{\partial y}\frac{\partial^2 w}{\partial x^2} + \frac{2}{5}\frac{\partial w}{\partial y}\frac{\partial^2 w}{\partial y^2} \\ \frac{8}{15}\frac{\partial^2 u}{\partial x \partial y} + \frac{4}{15}\frac{\partial^2 v}{\partial x^2} - \frac{1}{5}\frac{\partial^2 v}{\partial y^2} + \frac{8}{15}\frac{\partial w}{\partial x}\frac{\partial^2 w}{\partial x \partial y} + \frac{4}{15}\frac{\partial w}{\partial y}\frac{\partial^2 w}{\partial x^2} - \frac{1}{5}\frac{\partial w}{\partial y}\frac{\partial^2 w}{\partial y^2} \\ -\frac{1}{5}\frac{\partial^2 u}{\partial x^2} + \frac{4}{15}\frac{\partial^2 u}{\partial y^2} + \frac{8}{15}\frac{\partial^2 v}{\partial x \partial y} - \frac{1}{5}\frac{\partial w}{\partial x}\frac{\partial^2 w}{\partial x^2} + \frac{4}{15}\frac{\partial w}{\partial x}\frac{\partial^2 w}{\partial y^2} + \frac{8}{15}\frac{\partial w}{\partial y}\frac{\partial^2 w}{\partial x \partial y} \\ -\frac{1}{5}\frac{\partial^2 u}{\partial x^2} - \frac{1}{15}\frac{\partial^2 u}{\partial y^2} - \frac{2}{15}\frac{\partial^2 v}{\partial x \partial y} - \frac{1}{5}\frac{\partial w}{\partial x}\frac{\partial^2 w}{\partial x^2} - \frac{1}{15}\frac{\partial w}{\partial x}\frac{\partial^2 w}{\partial y^2} - \frac{2}{15}\frac{\partial w}{\partial y}\frac{\partial^2 w}{\partial x \partial y} \\ -\frac{2}{15}\frac{\partial^2 u}{\partial x \partial y} - \frac{1}{15}\frac{\partial^2 v}{\partial x^2} - \frac{1}{5}\frac{\partial^2 v}{\partial y^2} - \frac{2}{15}\frac{\partial w}{\partial x}\frac{\partial^2 w}{\partial x \partial y} - \frac{1}{15}\frac{\partial w}{\partial y}\frac{\partial^2 w}{\partial x^2} - \frac{1}{5}\frac{\partial w}{\partial y}\frac{\partial^2 w}{\partial y^2} \end{Bmatrix}$$

$$+ z \begin{Bmatrix} -\frac{2}{5}\frac{\partial^3 w}{\partial x^3} + \frac{3}{5}\frac{\partial^3 w}{\partial x \partial y^2} \\ \frac{3}{5}\frac{\partial^3 w}{\partial x^2 \partial y} - \frac{2}{5}\frac{\partial^3 w}{\partial y^3} \\ -\frac{4}{5}\frac{\partial^3 w}{\partial x^2 \partial y} + \frac{1}{5}\frac{\partial^3 w}{\partial y^3} \\ \frac{1}{5}\frac{\partial^3 w}{\partial x^3} - \frac{4}{5}\frac{\partial^3 w}{\partial x \partial y^2} \\ \frac{1}{5}\frac{\partial^3 w}{\partial x^3} + \frac{1}{5}\frac{\partial^3 w}{\partial x \partial y^2} \\ \frac{1}{5}\frac{\partial^3 w}{\partial x^2 \partial y} + \frac{1}{5}\frac{\partial^3 w}{\partial y^3} \end{Bmatrix} + z e^{-\frac{2z^2}{h^2}} \begin{Bmatrix} \frac{2}{5}\frac{\partial^2 \psi_x}{\partial x^2} - \frac{1}{5}\frac{\partial^2 \psi_x}{\partial y^2} - \frac{2}{5}\frac{\partial^2 \psi_y}{\partial x \partial y} \\ -\frac{2}{5}\frac{\partial^2 \psi_x}{\partial x \partial y} - \frac{1}{5}\frac{\partial^2 \psi_y}{\partial x^2} + \frac{2}{5}\frac{\partial^2 \psi_y}{\partial y^2} \\ \frac{8}{15}\frac{\partial^2 \psi_x}{\partial x \partial y} + \frac{4}{15}\frac{\partial^2 \psi_y}{\partial x^2} - \frac{1}{5}\frac{\partial^2 \psi_y}{\partial y^2} \\ -\frac{1}{5}\frac{\partial^2 \psi_x}{\partial x^2} + \frac{4}{15}\frac{\partial^2 \psi_x}{\partial y^2} + \frac{8}{15}\frac{\partial^2 \psi_y}{\partial x \partial y} \\ -\frac{1}{5}\frac{\partial^2 \psi_x}{\partial x^2} - \frac{1}{15}\frac{\partial^2 \psi_x}{\partial y^2} - \frac{2}{15}\frac{\partial^2 \psi_y}{\partial x \partial y} \\ -\frac{2}{15}\frac{\partial^2 \psi_x}{\partial x \partial y} - \frac{1}{15}\frac{\partial^2 \psi_y}{\partial x^2} - \frac{1}{5}\frac{\partial^2 \psi_y}{\partial y^2} \end{Bmatrix}$$

$$+ \frac{4z}{h^2} e^{-\frac{2z^2}{h^2}} \begin{Bmatrix} 0 \\ 0 \\ 0 \\ 0 \\ -\psi_x \\ -\psi_y \end{Bmatrix} + \frac{16z^3}{3h^4} e^{-\frac{2z^2}{h^2}} \begin{Bmatrix} 0 \\ 0 \\ 0 \\ 0 \\ \psi_x \\ \psi_y \end{Bmatrix}$$

$$= \boldsymbol{\eta}_{\mathbf{b}}^{(\mathbf{0})} + z\boldsymbol{\eta}_{\mathbf{b}}^{(\mathbf{1})} + z e^{-\frac{2z^2}{h^2}} \boldsymbol{\eta}_{\mathbf{b}}^{(\mathbf{2})} + \frac{4z}{h^2} e^{-\frac{2z^2}{h^2}} \boldsymbol{\eta}_{\mathbf{b}}^{(\mathbf{3})} + \frac{16z^3}{3h^4} e^{-\frac{2z^2}{h^2}} \boldsymbol{\eta}_{\mathbf{b}}^{(\mathbf{4})} \qquad (A5)$$

$$\boldsymbol{\eta_s}=\begin{Bmatrix}\eta_{zzz}\\ \eta_{xxz}\\ \eta_{yyz}\\ \eta_{xyz}\end{Bmatrix}=\begin{Bmatrix}\frac{1}{15}\frac{\partial^2 w}{\partial x^2}+\frac{1}{15}\frac{\partial^2 w}{\partial y^2}\\ -\frac{4}{15}\frac{\partial^2 w}{\partial x^2}+\frac{1}{15}\frac{\partial^2 w}{\partial y^2}\\ \frac{1}{15}\frac{\partial^2 w}{\partial x^2}-\frac{4}{15}\frac{\partial^2 w}{\partial y^2}\\ -\frac{1}{3}\frac{\partial^2 w}{\partial x\partial y}\end{Bmatrix}+e^{-\frac{2z^2}{h^2}}\begin{Bmatrix}-\frac{2}{15}\frac{\partial\psi_x}{\partial x}-\frac{2}{15}\frac{\partial\psi_y}{\partial y}\\ \frac{8}{15}\frac{\partial\psi_x}{\partial x}-\frac{2}{15}\frac{\partial\psi_y}{\partial y}\\ -\frac{2}{15}\frac{\partial\psi_x}{\partial x}+\frac{8}{15}\frac{\partial\psi_y}{\partial y}\\ \frac{1}{3}\frac{\partial\psi_x}{\partial y}+\frac{1}{3}\frac{\partial\psi_y}{\partial x}\end{Bmatrix}$$

$$+\frac{4z^2}{h^2}e^{-\frac{2z^2}{h^2}}\begin{Bmatrix}\frac{2}{15}\frac{\partial\psi_x}{\partial x}+\frac{2}{15}\frac{\partial\psi_y}{\partial y}\\ -\frac{8}{15}\frac{\partial\psi_x}{\partial x}+\frac{2}{15}\frac{\partial\psi_y}{\partial y}\\ \frac{2}{15}\frac{\partial\psi_x}{\partial x}-\frac{8}{15}\frac{\partial\psi_y}{\partial y}\\ -\frac{1}{3}\frac{\partial\psi_x}{\partial y}-\frac{1}{3}\frac{\partial\psi_y}{\partial x}\end{Bmatrix}=\boldsymbol{\eta_s^{(0)}}+e^{-\frac{2z^2}{h^2}}\boldsymbol{\eta_s^{(1)}}+\frac{4z^2}{h^2}e^{-\frac{2z^2}{h^2}}\boldsymbol{\eta_s^{(2)}}\qquad(A6)$$

$$\boldsymbol{\mathcal{S}_{Lb}^{i}}=\{s_{b1}^{i}\quad s_{b2}^{i}\quad s_{b3}^{i}\}^{T}\quad,\quad\boldsymbol{\mathcal{S}_{NLb}^{i}}=\{s_{b4}^{i}\quad 0\quad 0\}^{T}s_{G}^{i}\quad,\quad\boldsymbol{\mathcal{S}_{s}^{i}}=\{s_{s1}^{i}\quad s_{s2}^{i}\}\quad,\quad\mathbb{X}^{i}=\begin{Bmatrix}u^i\\ v^i\\ w^i\\ \psi_x^i\\ \psi_y^i\end{Bmatrix}\qquad(A7)$$

in which

$$s_{b1}^{i}=\begin{bmatrix}\frac{\partial\mathfrak{B}_i(x,y)}{\partial x}&0&0&0&0\\ 0&\frac{\partial\mathfrak{B}_i(x,y)}{\partial y}&0&0&0\\ \frac{\partial\mathfrak{B}_i(x,y)}{\partial y}&\frac{\partial\mathfrak{B}_i(x,y)}{\partial x}&0&0&0\end{bmatrix}\quad,\quad s_{b2}^{i}=\begin{bmatrix}0&0&-\frac{\partial^2\mathfrak{B}_i(x,y)}{\partial x^2}&0&0\\ 0&0&-\frac{\partial^2\mathfrak{B}_i(x,y)}{\partial y^2}&0&0\\ 0&0&-2\frac{\partial^2\mathfrak{B}_i(x,y)}{\partial x\partial y}&0&0\end{bmatrix}\qquad(A8)$$

$$\boldsymbol{s_{b3}^{i}}=\begin{bmatrix}\mathbf{0}&\mathbf{0}&\mathbf{0}&\boldsymbol{\frac{\partial\mathfrak{B}_i(x,y)}{\partial x}}&\mathbf{0}\\ \mathbf{0}&\mathbf{0}&\mathbf{0}&\mathbf{0}&\boldsymbol{\frac{\partial\mathfrak{B}_i(x,y)}{\partial y}}\\ \mathbf{0}&\mathbf{0}&\mathbf{0}&\boldsymbol{\frac{\partial\mathfrak{B}_i(x,y)}{\partial y}}&\boldsymbol{\frac{\partial\mathfrak{B}_i(x,y)}{\partial x}}\end{bmatrix}\quad,\quad\boldsymbol{s_{b4}^{i}}=\begin{bmatrix}\boldsymbol{\frac{\partial w^i}{\partial x}}&\mathbf{0}\\ \mathbf{0}&\boldsymbol{\frac{\partial w^i}{\partial y}}\\ \boldsymbol{\frac{\partial w^i}{\partial y}}&\boldsymbol{\frac{\partial w^i}{\partial x}}\end{bmatrix}\quad,\quad\boldsymbol{s_{G}^{i}}$$

$$=\begin{bmatrix}\mathbf{0}&\mathbf{0}&\boldsymbol{\frac{\partial\mathfrak{B}_i(x,y)}{\partial x}}&\mathbf{0}&\mathbf{0}\\ \mathbf{0}&\mathbf{0}&\boldsymbol{\frac{\partial\mathfrak{B}_i(x,y)}{\partial y}}&\mathbf{0}&\mathbf{0}\end{bmatrix}$$

$$\mathcal{s}_{s1}^{i}=\begin{bmatrix}0 & 0 & 0 & \mathfrak{B}_i(x,y) & 0\\ 0 & 0 & 0 & 0 & \mathfrak{B}_i(x,y)\end{bmatrix} \quad , \quad \mathcal{s}_{s2}^{i}=\begin{bmatrix}0 & 0 & 0 & -\mathfrak{B}_i(x,y) & 0\\ 0 & 0 & 0 & 0 & -\mathfrak{B}_i(x,y)\end{bmatrix}$$

$$\mathcal{G}_b^i=\{\mathcal{g}_{b1}^i \quad \mathcal{g}_{b2}^i \quad \mathcal{g}_{b3}^i\}^T \quad , \quad \mathcal{G}_s^i = \{\mathcal{g}_{s1}^i \quad \mathcal{g}_{s2}^i \quad \mathcal{g}_{s3}^i \quad \mathcal{g}_{s4}^i\}^T \qquad (A9)$$

where

$$\mathcal{g}_{b1}^i = \begin{bmatrix}0 & 0 & \frac{\partial^2\mathfrak{B}_i(x,y)}{\partial x\partial y} & 0 & 0\\ 0 & 0 & -\frac{\partial^2\mathfrak{B}_i(x,y)}{\partial x\partial y} & 0 & 0\\ 0 & 0 & 0 & 0 & 0\\ 0 & 0 & \frac{1}{2}\left(\frac{\partial^2\mathfrak{B}_i(x,y)}{\partial y^2}-\frac{\partial^2\mathfrak{B}_i(x,y)}{\partial x^2}\right) & 0 & 0\end{bmatrix} \qquad (A10)$$

$$\mathcal{g}_{b2}^i=\begin{bmatrix}0 & 0 & 0 & 0 & -\frac{1}{2}\frac{\partial\mathfrak{B}_i(x,y)}{\partial x}\\ 0 & 0 & 0 & \frac{1}{2}\frac{\partial\mathfrak{B}_i(x,y)}{\partial y} & 0\\ 0 & 0 & 0 & -\frac{1}{2}\frac{\partial\mathfrak{B}_i(x,y)}{\partial y} & \frac{1}{2}\frac{\partial\mathfrak{B}_i(x,y)}{\partial x}\\ 0 & 0 & 0 & \frac{1}{2}\frac{\partial\mathfrak{B}_i(x,y)}{\partial x} & -\frac{1}{2}\frac{\partial\mathfrak{B}_i(x,y)}{\partial y}\end{bmatrix}, \quad \mathcal{g}_{b3}^i=\begin{bmatrix}0 & 0 & 0 & 0 & \frac{1}{2}\frac{\partial\mathfrak{B}_i(x,y)}{\partial x}\\ 0 & 0 & 0 & -\frac{1}{2}\frac{\partial\mathfrak{B}_i(x,y)}{\partial y} & 0\\ 0 & 0 & 0 & \frac{1}{2}\frac{\partial\mathfrak{B}_i(x,y)}{\partial y} & -\frac{1}{2}\frac{\partial\mathfrak{B}_i(x,y)}{\partial x}\\ 0 & 0 & 0 & -\frac{1}{2}\frac{\partial\mathfrak{B}_i(x,y)}{\partial x} & \frac{1}{2}\frac{\partial\mathfrak{B}_i(x,y)}{\partial y}\end{bmatrix}$$

$$\mathcal{g}_{s1}^i=\begin{bmatrix}-\frac{1}{4}\frac{\partial^2\mathfrak{B}_i(x,y)}{\partial x\partial y} & \frac{1}{4}\frac{\partial^2\mathfrak{B}_i(x,y)}{\partial x^2} & 0 & 0 & 0\\ -\frac{1}{4}\frac{\partial^2\mathfrak{B}_i(x,y)}{\partial y^2} & \frac{1}{4}\frac{\partial^2\mathfrak{B}_i(x,y)}{\partial x\partial y} & 0 & 0 & 0\end{bmatrix} \quad , \quad \mathcal{g}_{s2}^i = \begin{bmatrix}0 & 0 & 0 & -\frac{\partial^2\mathfrak{B}_i(x,y)}{\partial x\partial y} & \frac{\partial^2\mathfrak{B}_i(x,y)}{\partial x^2}\\ 0 & 0 & 0 & -\frac{\partial^2\mathfrak{B}_i(x,y)}{\partial y^2} & \frac{\partial^2\mathfrak{B}_i(x,y)}{\partial x\partial y}\end{bmatrix}$$

$$\mathcal{g}_{s3}^i=\begin{bmatrix}0 & 0 & 0 & 0 & \mathfrak{B}_i(x,y)\\ 0 & 0 & 0 & -\mathfrak{B}_i(x,y) & 0\end{bmatrix} \quad , \quad \mathcal{g}_{s4}^i=\begin{bmatrix}0 & 0 & 0 & 0 & -\mathfrak{B}_i(x,y)\\ 0 & 0 & 0 & \mathfrak{B}_i(x,y) & 0\end{bmatrix}$$

$$\mathcal{J}_{Lb}^i=\{\mathcal{j}_{b1}^i \quad \mathcal{j}_{b2}^i \quad \mathcal{j}_{b3}^i\}^T \quad , \quad \mathcal{J}_{NLb}^i=\{\mathcal{j}_{b4}^i \quad 0 \quad 0\}^T \mathcal{j}_G^i \quad , \quad \mathcal{J}_s^i=\{\mathcal{j}_{s1}^i \quad \mathcal{j}_{s2}^i \quad \mathcal{j}_{s3}^i\}^T \qquad (A11)$$

$$\mathcal{J}_{b1}^{i}=\begin{bmatrix}\dfrac{\partial^2\mathfrak{B}_i(x,y)}{\partial x^2} & \dfrac{\partial^2\mathfrak{B}_i(x,y)}{\partial x\partial y} & 0 & 0 & 0\\ \dfrac{\partial^2\mathfrak{B}_i(x,y)}{\partial x\partial y} & \dfrac{\partial^2\mathfrak{B}_i(x,y)}{\partial y^2} & 0 & 0 & 0\end{bmatrix} \quad , \quad \mathcal{J}_{b2}^{i}=\begin{bmatrix}0 & 0 & -\dfrac{\partial^3\mathfrak{B}_i(x,y)}{\partial x^3} & -\dfrac{\partial^3\mathfrak{B}_i(x,y)}{\partial x\partial y^2} & 0 & 0\\ 0 & 0 & -\dfrac{\partial^3\mathfrak{B}_i(x,y)}{\partial x^2\partial y} & -\dfrac{\partial^3\mathfrak{B}_i(x,y)}{\partial y^3} & 0 & 0\end{bmatrix}$$

$$\mathcal{J}_{b3}^{i}=\begin{bmatrix}0 & 0 & 0 & \dfrac{\partial^2\mathfrak{B}_i(x,y)}{\partial x^2} & \dfrac{\partial^2\mathfrak{B}_i(x,y)}{\partial x\partial y}\\ 0 & 0 & 0 & \dfrac{\partial^2\mathfrak{B}_i(x,y)}{\partial x\partial y} & \dfrac{\partial^2\mathfrak{B}_i(x,y)}{\partial y^2}\end{bmatrix} \quad , \quad \mathcal{J}_{b4}^{i}=\begin{bmatrix}\dfrac{\partial^2 w^i}{\partial x^2} & \dfrac{\partial^2 w^i}{\partial x\partial y}\\ \dfrac{\partial^2 w^i}{\partial x\partial y} & \dfrac{\partial^2 w^i}{\partial y^2}\end{bmatrix} \qquad (A12)$$

$$\mathcal{J}_{G}^{i}=\begin{bmatrix}0 & 0 & \dfrac{\partial\mathfrak{B}_i(x,y)}{\partial x} & 0 & 0\\ 0 & 0 & \dfrac{\partial\mathfrak{B}_i(x,y)}{\partial y} & 0 & 0\end{bmatrix} \quad , \quad \mathcal{J}_{s1}^{i}=\begin{bmatrix}0 & 0 & -\dfrac{\partial^2\mathfrak{B}_i(x,y)}{\partial x^2} & -\dfrac{\partial^2\mathfrak{B}_i(x,y)}{\partial y^2} & 0 & 0\end{bmatrix}$$

$$\mathcal{J}_{s2}^{i}=\begin{bmatrix}0 & 0 & 0 & \dfrac{\partial\mathfrak{B}_i(x,y)}{\partial x} & \dfrac{\partial\mathfrak{B}_i(x,y)}{\partial x}\end{bmatrix} \quad , \quad \mathcal{J}_{s3}^{i}=\begin{bmatrix}0 & 0 & 0 & -\dfrac{\partial\mathfrak{B}_i(x,y)}{\partial x} & -\dfrac{\partial\mathfrak{B}_i(x,y)}{\partial x}\end{bmatrix}$$

$$\mathcal{Y}_{Lb}^{i}=\{\mathcal{Y}_{b1}^{i} \quad \mathcal{Y}_{b2}^{i} \quad \mathcal{Y}_{b3}^{i} \quad \mathcal{Y}_{b4}^{i} \quad \mathcal{Y}_{b5}^{i}\}^{T} \quad , \quad \mathcal{Y}_{NLb}^{i}=\{\mathcal{Y}_{b6}^{i} \quad 0 \quad 0 \quad 0 \quad 0\}^{T}\mathcal{Y}_{G}^{i}$$

$$\mathcal{Y}_{s}^{i}=\{\mathcal{Y}_{s1}^{i} \quad \mathcal{Y}_{s2}^{i} \quad \mathcal{Y}_{s3}^{i}\} \qquad (A13)$$

$$\mathcal{Y}_{b1}^{i}=\begin{bmatrix}\frac{2}{5}\dfrac{\partial^2\mathfrak{B}_i(x,y)}{\partial x^2}-\frac{1}{5}\dfrac{\partial^2\mathfrak{B}_i(x,y)}{\partial y^2} & -\frac{2}{5}\dfrac{\partial^2\mathfrak{B}_i(x,y)}{\partial x\partial y} & 0 & 0 & 0\\ -\frac{2}{5}\dfrac{\partial^2\mathfrak{B}_i(x,y)}{\partial x\partial y} & -\frac{1}{5}\dfrac{\partial^2\mathfrak{B}_i(x,y)}{\partial x^2}+\frac{2}{5}\dfrac{\partial^2\mathfrak{B}_i(x,y)}{\partial y^2} & 0 & 0 & 0\\ \frac{8}{15}\dfrac{\partial^2\mathfrak{B}_i(x,y)}{\partial x\partial y} & \frac{4}{15}\dfrac{\partial^2\mathfrak{B}_i(x,y)}{\partial x^2}-\frac{1}{5}\dfrac{\partial^2\mathfrak{B}_i(x,y)}{\partial y^2} & 0 & 0 & 0\\ -\frac{1}{5}\dfrac{\partial^2\mathfrak{B}_i(x,y)}{\partial x^2}+\frac{4}{15}\dfrac{\partial^2\mathfrak{B}_i(x,y)}{\partial y^2} & \frac{8}{15}\dfrac{\partial^2\mathfrak{B}_i(x,y)}{\partial x\partial y} & 0 & 0 & 0\\ -\frac{1}{5}\dfrac{\partial^2\mathfrak{B}_i(x,y)}{\partial x^2}-\frac{1}{15}\dfrac{\partial^2\mathfrak{B}_i(x,y)}{\partial y^2} & -\frac{2}{15}\dfrac{\partial^2\mathfrak{B}_i(x,y)}{\partial x\partial y} & 0 & 0 & 0\\ -\frac{2}{15}\dfrac{\partial^2\mathfrak{B}_i(x,y)}{\partial x\partial y} & -\frac{1}{15}\dfrac{\partial^2\mathfrak{B}_i(x,y)}{\partial x^2}-\frac{1}{5}\dfrac{\partial^2\mathfrak{B}_i(x,y)}{\partial y^2} & 0 & 0 & 0\end{bmatrix}$$

$$\mathcal{Y}_{b2}^{i}=\begin{bmatrix}0&0&-\frac{2}{5}\frac{\partial^3\mathfrak{B}_i(x,y)}{\partial x^3}+\frac{3}{5}\frac{\partial^3\mathfrak{B}_i(x,y)}{\partial x\partial y^2}&0&0\\0&0&\frac{3}{5}\frac{\partial^3\mathfrak{B}_i(x,y)}{\partial x^2\partial y}-\frac{2}{5}\frac{\partial^3\mathfrak{B}_i(x,y)}{\partial y^3}&0&0\\0&0&-\frac{4}{5}\frac{\partial^3\mathfrak{B}_i(x,y)}{\partial x^2\partial y}+\frac{1}{5}\frac{\partial^3\mathfrak{B}_i(x,y)}{\partial y^3}&0&0\\0&0&\frac{1}{5}\frac{\partial^3\mathfrak{B}_i(x,y)}{\partial x^3}-\frac{4}{5}\frac{\partial^3\mathfrak{B}_i(x,y)}{\partial x\partial y^2}&0&0\\0&0&\frac{1}{5}\frac{\partial^3\mathfrak{B}_i(x,y)}{\partial x^3}+\frac{1}{5}\frac{\partial^3\mathfrak{B}_i(x,y)}{\partial x\partial y^2}&0&0\\0&0&\frac{1}{5}\frac{\partial^3\mathfrak{B}_i(x,y)}{\partial x^2\partial y}+\frac{1}{5}\frac{\partial^3\mathfrak{B}_i(x,y)}{\partial y^3}&0&0\end{bmatrix},\quad \mathcal{Y}_{b4}^{i}=\begin{bmatrix}0&0&0&0&0\\0&0&0&0&0\\0&0&0&0&0\\0&0&0&0&0\\0&0&0&-\mathfrak{B}_i(x,y)&0\\0&0&0&0&-\mathfrak{B}_i(x,y)\end{bmatrix}$$

$$\mathcal{Y}_{b3}^{i}=\begin{bmatrix}0&0&0&\frac{2}{5}\frac{\partial^2\mathfrak{B}_i(x,y)}{\partial x^2}-\frac{1}{5}\frac{\partial^2\mathfrak{B}_i(x,y)}{\partial y^2}&-\frac{2}{5}\frac{\partial^2\mathfrak{B}_i(x,y)}{\partial x\partial y}\\0&0&0&-\frac{2}{5}\frac{\partial^2\mathfrak{B}_i(x,y)}{\partial x\partial y}&-\frac{1}{5}\frac{\partial^2\mathfrak{B}_i(x,y)}{\partial x^2}+\frac{2}{5}\frac{\partial^2\mathfrak{B}_i(x,y)}{\partial y^2}\\0&0&0&\frac{8}{15}\frac{\partial^2\mathfrak{B}_i(x,y)}{\partial x\partial y}&\frac{4}{15}\frac{\partial^2\mathfrak{B}_i(x,y)}{\partial x^2}-\frac{1}{5}\frac{\partial^2\mathfrak{B}_i(x,y)}{\partial y^2}\\0&0&0&-\frac{1}{5}\frac{\partial^2\mathfrak{B}_i(x,y)}{\partial x^2}+\frac{4}{15}\frac{\partial^2\mathfrak{B}_i(x,y)}{\partial y^2}&\frac{8}{15}\frac{\partial^2\mathfrak{B}_i(x,y)}{\partial x\partial y}\\0&0&0&-\frac{1}{5}\frac{\partial^2\mathfrak{B}_i(x,y)}{\partial x^2}-\frac{1}{15}\frac{\partial^2\mathfrak{B}_i(x,y)}{\partial y^2}&-\frac{2}{15}\frac{\partial^2\mathfrak{B}_i(x,y)}{\partial x\partial y}\\0&0&0&-\frac{2}{15}\frac{\partial^2\mathfrak{B}_i(x,y)}{\partial x\partial y}&-\frac{1}{15}\frac{\partial^2\mathfrak{B}_i(x,y)}{\partial x^2}-\frac{1}{5}\frac{\partial^2\mathfrak{B}_i(x,y)}{\partial y^2}\end{bmatrix}\qquad (A14)$$

$$\mathcal{Y}_{b5}^{i}=\begin{bmatrix}0&0&0&0&0\\0&0&0&0&0\\0&0&0&0&0\\0&0&0&0&0\\0&0&0&\mathfrak{B}_i(x,y)&0\\0&0&0&0&\mathfrak{B}_i(x,y)\end{bmatrix},\quad \mathcal{Y}_{b6}^{i}=\begin{bmatrix}\frac{2}{5}\frac{\partial^2w^i}{\partial x^2}-\frac{1}{5}\frac{\partial^2w^i}{\partial y^2}&-\frac{2}{5}\frac{\partial^2w^i}{\partial x\partial y}\\-\frac{2}{5}\frac{\partial^2w^i}{\partial x\partial y}&-\frac{1}{5}\frac{\partial^2w^i}{\partial x^2}+\frac{2}{5}\frac{\partial^2w^i}{\partial y^2}\\\frac{8}{15}\frac{\partial^2w^i}{\partial x\partial y}&\frac{4}{15}\frac{\partial^2w^i}{\partial x^2}-\frac{1}{5}\frac{\partial^2w^i}{\partial y^2}\\-\frac{1}{5}\frac{\partial^2w^i}{\partial x^2}+\frac{4}{15}\frac{\partial^2w^i}{\partial y^2}&\frac{8}{15}\frac{\partial^2w^i}{\partial x\partial y}\\-\frac{1}{5}\frac{\partial^2w^i}{\partial x^2}-\frac{1}{15}\frac{\partial^2w^i}{\partial y^2}&-\frac{2}{15}\frac{\partial^2w^i}{\partial x\partial y}\\-\frac{2}{15}\frac{\partial^2w^i}{\partial x\partial y}&-\frac{1}{15}\frac{\partial^2w^i}{\partial x^2}-\frac{1}{5}\frac{\partial^2w^i}{\partial y^2}\end{bmatrix}$$

$$\boldsymbol{\mathcal{Y}}_{\boldsymbol{G}}^{\boldsymbol{i}}=\begin{bmatrix}0 & 0 & \dfrac{\partial\mathfrak{B}_i(x,y)}{\partial x} & 0 & 0\\ 0 & 0 & \dfrac{\partial\mathfrak{B}_i(x,y)}{\partial y} & 0 & 0\end{bmatrix}\quad,\quad \mathcal{Y}_{s1}^{i}=\begin{bmatrix}0 & 0 & \dfrac{1}{15}\dfrac{\partial^2\mathfrak{B}_i(x,y)}{\partial x^2}+\dfrac{1}{15}\dfrac{\partial^2\mathfrak{B}_i(x,y)}{\partial y^2} & 0 & 0\\ 0 & 0 & -\dfrac{4}{15}\dfrac{\partial^2\mathfrak{B}_i(x,y)}{\partial x^2}+\dfrac{1}{15}\dfrac{\partial^2\mathfrak{B}_i(x,y)}{\partial y^2} & 0 & 0\\ 0 & 0 & \dfrac{1}{15}\dfrac{\partial^2\mathfrak{B}_i(x,y)}{\partial x^2}-\dfrac{4}{15}\dfrac{\partial^2\mathfrak{B}_i(x,y)}{\partial y^2} & 0 & 0\\ 0 & 0 & -\dfrac{1}{3}\dfrac{\partial^2\mathfrak{B}_i(x,y)}{\partial x\partial y} & 0 & 0\end{bmatrix}$$

$$\mathcal{Y}_{s2}^{i}=\begin{bmatrix}0 & 0 & 0 & -\dfrac{2}{15}\dfrac{\partial\mathfrak{B}_i(x,y)}{\partial x} & -\dfrac{2}{15}\dfrac{\partial\mathfrak{B}_i(x,y)}{\partial y}\\ 0 & 0 & 0 & \dfrac{8}{15}\dfrac{\partial\mathfrak{B}_i(x,y)}{\partial x} & -\dfrac{2}{15}\dfrac{\partial\mathfrak{B}_i(x,y)}{\partial y}\\ 0 & 0 & 0 & -\dfrac{2}{15}\dfrac{\partial\mathfrak{B}_i(x,y)}{\partial x} & \dfrac{8}{15}\dfrac{\partial\mathfrak{B}_i(x,y)}{\partial y}\\ 0 & 0 & 0 & \dfrac{1}{3}\dfrac{\partial\mathfrak{B}_i(x,y)}{\partial y} & \dfrac{1}{3}\dfrac{\partial\mathfrak{B}_i(x,y)}{\partial x}\end{bmatrix}\quad \mathcal{Y}_{s3}^{i}=\begin{bmatrix}0 & 0 & 0 & \dfrac{2}{15}\dfrac{\partial\mathfrak{B}_i(x,y)}{\partial x} & \dfrac{2}{15}\dfrac{\partial\mathfrak{B}_i(x,y)}{\partial y}\\ 0 & 0 & 0 & -\dfrac{8}{15}\dfrac{\partial\mathfrak{B}_i(x,y)}{\partial x} & \dfrac{2}{15}\dfrac{\partial\mathfrak{B}_i(x,y)}{\partial y}\\ 0 & 0 & 0 & \dfrac{2}{15}\dfrac{\partial\mathfrak{B}_i(x,y)}{\partial x} & -\dfrac{8}{15}\dfrac{\partial\mathfrak{B}_i(x,y)}{\partial y}\\ 0 & 0 & 0 & -\dfrac{1}{3}\dfrac{\partial\mathfrak{B}_i(x,y)}{\partial y} & -\dfrac{1}{3}\dfrac{\partial\mathfrak{B}_i(x,y)}{\partial x}\end{bmatrix}$$

References

[1] N. Yamamoto, A.J. Hart, E.J. Garcia, S.S. Wicks, H.M. Duong, A.H. Slocum, B.L. Wardle. High-yield growth and morphology control of aligned carbon nanotubes on ceramic fibers for multifunctional enhancement of structural composites. *Carbon* 47 (2009) 551-560.

[2] R.B. Mathur, S. Chatterjee, B.P. Singh. Growth of carbon nanotubes on carbon fibre substrates to produce hybrid/phenolic composites with improved mechanical properties. *Composites Science and Technology* 68 (2008) 1608-1615.

[3] E.J. Garcia, B.L. Wardle, A.J. Hart, N. Yamamoto. Fabrication and multifunctional properties of a hybrid laminate with aligned carbon nanotubes grown in situ. *Composites Science and Technology* 68 (2008) 2034-2041.

[4] M. Kulkarni, D. Carnahan, K. Kulkarni, D. Qian, J.L. Abot. Elastic response of a carbon nanotube fiber reinforced polymeric composite: a numerical and experimental study. *Composites Part B: Engineering* 41 (2010) 414-421.

[5] M.C. Ray, S.I. Kundalwal. A thermomechanical shear lag analysis of short fuzzy fiber reinforced composite containing wavy carbon nanotubes. *European Journal of Mechanics-A/Solids* 44 (2014) 41-60.

[6] S.I. Kundalwal, S.A. Meguid. Micromechanics modelling of the effective thermoelastic response of nano-tailored composites. *European Journal of Mechanics-A/Solids* 53 (2015) 241-253.

[7] S.I. Kundalwal, M.C. Ray. Effective properties of a novel continuous fuzzy-fiber reinforced composite using the method of cells and the finite element method. *European Journal of Mechanics, A/Solids* 36 (2012) 191–203.

[8] S. Dhala, M.C. Ray. Micromechanics of piezoelectric fuzzy fiber-reinforced composite. *Mechanics of Materials* 81 (2015) 1-17.

[9] M.K. Hassanzadeh-Aghdam, M.J. Mahmoodi, R. Ansari. Micromechanics-based characterization of mechanical properties of fuzzy fiber-reinforced composites containing carbon nanotubes. *Mechanics of Materials* 118 (2018) 31-43.

[10] D.C.C. Lam, F. Yang, A.C.M. Chong, J. Wang, P. Tong. Experiments and theory in strain gradient elasticity. *Journal of the Mechanics and Physics of Solids* 51 (2003) 1477-1508.

[11] R. Ansari, R. Gholami, S. Sahmani. Study of small scale effects on the nonlinear vibration response of functionally graded Timoshenko microbeams based on the strain gradient theory. *Journal of Computational and Nonlinear Dynamics* 7 (2012) 031009.
[12] B. Akgoz, O. Civalek. A new trigonometric beam model for buckling of strain gradient microbeams. *International Journal of Mechanical Sciences* 81 (2014) 88-94.
[13] A. Jamalpoor, M. Hosseini. Biaxial buckling analysis of double-orthotropic microplate-systems including in-plane magnetic field based on strain gradient theory. *Composites Part B: Engineering* 75 (2015) 53-64.
[14] B. Zhang, Y. He, D. Liu, L. Shen, J. Lei. An efficient size-dependent plate theory for bending, buckling and free vibration analyses of functionally graded microplates resting on elastic foundation. *Applied Mathematical Modelling* 39 (2015) 3814-3845.
[15] M. Mohammadimehr, B. Rousta Navi, A. Ghorbanpour Arani. Modified strain gradient Reddy rectangular plate model for biaxial buckling and bending analysis of double-coupled piezoelectric polymeric nanocomposite reinforced by FG-SWNT. *Composites Part B: Engineering* 87 (2016) 132-148.
[16] M. Shojaeian, Y. Tadi Beni, H. Ataei. Electromechanical buckling of functionally graded electrostatic nanobridges using strain gradient theory. *Acta Astronautica* 118 (2016) 62-71.
[17] S.T. Yaghoubi, S. Mahmoud Mousavi, J. Paavola. Buckling of centrosymmetric anisotropic beam structures within strain gradient elasticity. *International Journal of Solids and Structures* 109 (2017) 84-92.
[18] M. Mirsalehi, M. Azhari, H. Amoushahi. Buckling and free vibration of the FGM thin micro-plate based on the modified strain gradient theory and the spline finite strip method. *European Journal of Mechanics – A/Solids* 61 (2017) 1-13.
[19] S. Khakalo, V. Balobanov, J. Niiranen. Modelling size-dependent bending, buckling and vibrations of 2D triangular lattices by strain gradient elasticity models: Applications to sandwich beams and auxetics. *International Journal of Engineering Science* 127 (2018) 33-52.
[20] H. Salehipour, A. Shahsavar. A three dimensional elasticity model for free vibration analysis of functionally graded micro/nano plates: Modified strain gradient theory. *Composite Structures* 206 (2018) 415-424.
[21] M. Arefi, E. Mohammad-Rezaei Bidgoli, T. Rabczuk. Thermo-mechanical buckling behavior of FG GNP reinforced micro plate based on MSGT. *Thin-Walled Structures* 142 (2019) 444-459.
[22] A. Farzam, B. Hassani. Size-dependent analysis of FG microplates with temperature-dependent material properties using modified strain gradient theory and isogeometric approach. *Composites Part B: Engineering* 161 (2019) 150-168
[23] B. Zhang, H. Li, L. Kong, H. Shen, X. Zhang. Size-dependent static and dynamic analysis of Reddy-type micro-beams by strain gradient differential quadrature finite element method. *Thin-Walled Structures* 148 (2020) 106496.
[24] G. Fu, S. Zhou, L. Qi. On the strain gradient elasticity theory for isotropic materials. *International Journal of Engineering Science* 154 (2020) 103348.
[25] M. Bacciocchi, A.M. Tarantino. Analytical solutions for vibrations and buckling analysis of laminated composite nanoplates based on third-order theory and strain gradient approach. *Composite Structures* 272 (2021) 114083.
[26] J. Zheng, C. Zhang, F. Musharavati, A. Khan, T.A. Sebaey. Thermo-mechanical buckling analysis of FG-GNPs reinforced composites sandwich microplates using a trigonometric four-variable shear deformation theory. *Case Studies in Thermal Engineering* 26 (2021) 101120.
[27] J. Torabi, J. Niiranen. Microarchitecture-dependent nonlinear bending analysis for cellular plates with prismatic corrugated cores via an anisotropic strain gradient plate theory of first-order shear deformation. *Engineering Structures* 236 (2021) 112117.
[28] J.H. Sun, Z.D. Zhou, S. Sahmani, B. Safaei. Microstructural size dependency in nonlinear lateral stability of random reinforced microshells via meshfree-based applied mathematical modeling. *International Journal of Structural Stability and Dynamics* 21 (2021) 2150164.

[29] J. Chu, Y. Wang, S. Sahmani, B. Safaei. Nonlinear large-amplitude oscillations of PFG composite rectangular microplates based upon the modified strain gradient elasticity theory. *International Journal of Structural Stability and Dynamics* 22 (2022) 2250068.
[30] J. Wang, B. Ma, J. Gao, H. Liu, B. Safaei, S. Sahmani. Nonlinear stability characteristics of porous graded composite microplates including various microstructural-dependent strain gradient tensors. *International Journal of Applied Mechanics* 14 (2022) 2150129.
[31] G. Fu, Z. Zhang, J. Fu, H. Zheng. On the strain gradient effects on buckling of the partially covered laminated microbeam. *Applied Mathematical Modelling* 102 (2022) 472-491.
[32] T.M. Le, D. Vo, J. Rungamornrat, T.Q. Bui. Strain-gradient theory for shear deformation free-form microshells: Governing equations of motion and general boundary conditions. *International Journal of Solids and Structures* 248 (2022) 111579.
[33] P.T. Hung, P. Phung-Van, C.H. Thai. A refined isogeometric plate analysis of porous metal foam microplates using modified strain gradient theory. *Composite Structures* 289 (2022) 115467.
[34] P.T. Hung, C.H. Thai, P. Phung-Van. Isogeometric bending and free vibration analyses of carbon nanotube-reinforced magneto-electric-elastic microplates using a four variable refined plate theory. *Computers & Structures* 287 (2023) 107121.
[35] K. Khorshidi, B. Soltannia, M. Karimi, M. Zakaryaei. Natural frequencies of submerged microplate structures, coupled to stationary fluid, using modified strain gradient theory. *Composite Structures* 326 (2023) 117583.
[36] W. Xiang, H. Ni, Y. Wu, B. Liu. New closed-form solutions for flexural vibration of microplates based on a modified strain gradient theory. *Thin-Walled Structures* 185 (2023) 110558.
[37] T. Hai, M.M. Al-Masoudy, S. Alsulamy, M.H. El Ouni, A. Ayvazyan, A. Kumar. Size-dependent free vibration analysis of honeycomb sandwich microplates integrated with piezoelectric actuators based on the modified strain gradient theory. *Composite Structures* 305 (2023) 116555.
[38] I. Barbaros, S. Sahmani, B. Safaei. Nonlinear in-plane thermomechanical stability of shallow sandwich micro-arches including strain gradient tensors. *Communications in Nonlinear Science and Numerical Simulation* 127 (2023) 107544.
[39] A. Karamanli, T.P. Vo, O. Civalek. Higher order finite element models for transient analysis of strain gradient functionally graded microplates. *European Journal of Mechanics – A/Solids* 99 (2023) 104933.
[40] D. Hou, L. Wang, J. Yan. Vibration analysis of a cylindrical shell by using strain gradient theory via a moving Kriging interpolation-based meshfree method. *Thin-Walled Structures* 184 (2023) 110466.
[41] V. Jain, R. Kumar, T. Dey, S.N. Patel, G. Watts. A meshfree formulation for size-dependent thermal buckling and post-buckling behaviour of porous microplates on elastic foundation subjected to localized heating. *Thin-Walled Structures* 205 (2024) 112451.
[42] S. Sahmani, B. Safaei, T. Rabczuk. Nonlinear in-plane buckling of small-curved and large-curved FG porous microbeams via strain gradient-based isogeometric collocation formulations. *Composite Structures* 334 (2024) 117969.
[43] N.-D. Nguyen, V.-T. Bui, T.-K. Nguyen. A modified strain gradient theory for buckling, bending and free vibration behaviors of metal foam microbeams. *Structures* 64 (2024) 106533.
[44] S. Sahmani, F. Fan, B. Safaei. Modified strain gradient plate model for nonlinear dynamics of sinusoidal impulsive actuated porous/piezoelectric laminated microharvesters. *Communications in Nonlinear Science and Numerical Simulation* 132 (2024) 107861.
[45] Y. Zhou, K. Huang. Static and dynamic stabilities of modified gradient elastic Kirchhoff–Love plates. *European Journal of Mechanics-A/Solids* 108 (2024) 105426.
[46] S. Mirzaei, M. Hejazi, R. Ansari. Size-dependent behaviour of in-plane bi-directional functionally graded porous microplates with variable thickness based on the modified strain gradient theory and IGA. *Thin-Walled Structures* 211 (2025) 113144.
[47] S. Sahmani, T. Rabczuk, J.H. Song, B. Safaei. Asymmetric nonlinear instability of thermally induced microsize arches having dissimilar boundary conditions incorporating strain gradient tensors. *Applied Mathematical Modelling* 146 (2025) 116187.

[48] P.R. Saffari, P.R. Saffari, T. Senjuntichai, S. Askarinejad, K. Ghabraie, C. Thongchom. Energy harvesting performance of fluid-immersed bimorph FG-GPLRC sandwich microplates in thermal gradient and magnetic field environments: A modified strain gradient theory approach. *European Journal of Mechanics – A/Solids* 112 (2025) 105635.
[49] M. Imani, S. Hamzehei-Javaran, S. Shojaee, B. Daraei. Vibration analysis of functionally graded curved microbeams using modified strain gradient finite elements. *Journal of Sound and Vibration* 618 (2025) 119298.
[50] X.L. Chen, Y.J. Liu. Square representative volume elements for evaluating the effective material properties of carbon nanotube-based composites. *Computational Materials Science* 29 (2004) 1–11.
[51] J.L. Tsai, S.H. Tzeng, Y.T. Chiu. Characterizing elastic properties of carbon nanotubes/polyimide nanocomposites using multi-scale simulation. *Composites Part B: Engineering* 41 (2010) 106-115.
[52] S.I. Kundalwal, M.C. Ray. Effect of carbon nanotube waviness on the elastic properties of the fuzzy fiber reinforced composites. *ASME Journal of Applied Mechanics* 80 (2013) 021010.
[53] S.I. Kundalwal, M.C. Ray. Effect of carbon nanotube waviness on the effective thermoelastic properties of a novel continuous fuzzy fiber reinforced composite. *Composites Part B: Engineering* 57 (2014) 199-209.
[54] M.J. Mahmoodi, M. Vakilifard. A comprehensive micromechanical modeling of electro-thermo-mechanical behaviors of CNT reinforced smart nanocomposites. *Materials & Design* 122 (2017) 347-365.
[55] M.K. Hassanzadeh-Aghdam, R. Ansari, A. Darvizeh. Micromechanical modeling of thermal expansion coefficients for unidirectional glass fiber-reinforced polyimide composites containing silica nanoparticles. *Composites Part A: Applied Science and Manufacturing* 96 (2017) 110-121.
[56] R. Ansari, M.K. Hassanzadeh-Aghdam. Micromechanics-based viscoelastic analysis of carbon nanotube-reinforced composites subjected to uniaxial and biaxial loading. *Composites Part B: Engineering* 90 (2016) 512-522.
[57] Y. Zare. Effects of interphase on tensile strength of polymer/CNT nanocomposites by Kelly–Tyson theory. *Mechanics of Materials* 85 (2015) 1-6.
[58] K.M. Hamdia, M. Silani, X. Zhuang, P. He, T. Rabczuk. Stochastic analysis of the fracture toughness of polymeric nanoparticle composites using polynomial chaos expansions. *International Journal of Fracture* 206 (2017) 215-227.
[59] P.J. Hine, H.R. Lusti, A.A. Gusev. Numerical simulation of the effects of volume fraction, aspect ratio and fibre length distribution on the elastic and thermoelastic properties of short fibre composites. *Composites Science and Technology* 62 (2002) 1445-1453.
[60] S.I. Kundalwal, M.C. Ray. Estimation of thermal conductivities of a novel fuzzy fiber reinforced composite. *International Journal of Thermal Sciences* 76 (2014) 90-100.
[61] M.M. Aghdam, D.J. Smith, M.J. Pavier. Finite element micromechanical modelling of yield and collapse behaviour of metal matrix composites. *Journal of the Mechanics and Physics of Solids* 48 (2000) 499-528.
[62] S.R. Falahatgard, M. Salehi, M.M. Aghdam. Nonlinear viscoelastic response of unidirectional fiber-reinforced composites in off-axis loading. *Journal of reinforced Plastics and Composites* 28 (2009) 1793-1811.
[63] M.K. Hassanzadeh-Aghdam, R. Ansari, A. Darvizeh. Micromechanical modeling of thermal expansion coefficients for unidirectional glass fiber-reinforced polyimide composites containing silica nanoparticles. *Composites Part A: Applied Science and Manufacturing* 96 (2017) 110-121.
[64] M.J. Mahmoodi, M. Vakilifard. A comprehensive micromechanical modeling of electro-thermo-mechanical behaviors of CNT reinforced smart nanocomposites. *Materials & Design* 122 (2017) 347-365.
[65] M.J. Mahmoodi, M.M. Aghdam, M. Shakeri. The effects of interfacial debonding on the elastoplastic response of unidirectional silicon carbide-titanium composites. *Proceedings of the Institution of Mechanical Engineers, Part C: Journal of Mechanical Engineering Science* 224 (2010) 259-269.
[66] M.M. Aghdam, A. Dezhsetan. Micromechanics based analysis of randomly distributed fiber reinforced composites using simplified unit cell model. *Composite Structures* 71 (2005) 327-332.
[67] M.J. Mahmoodi, M.M. Aghdam, M. Shakeri. Micromechanical modeling of interface damage of metal matrix composites subjected to off-axis loading. *Materials & Design* 31 (2010) 829-836.

[68] K. Khorshidi, A. Fallah. Buckling analysis of functionally graded rectangular nano-plate based on nonlocal exponential shear deformation theory. *International Journal of Mechanical Sciences* 113 (2016) 94-104.
[69] S. Yin, T. Yu, T.Q. Bui, P. Liu, S. Hirose. Buckling and vibration extended isogeometric analysis of imperfect graded Reissner-Mindlin plates with internal defects using NURBS and level sets. *Computers & Structures* 177 (2016) 23-38.
[70] N.N. Van Do, C.-H. Lee. Quasi-3D isogeometric buckling analysis method for advanced composite plates in thermal environments. *Aerospace Science and Technology* 92 (2019) 34-54.
[71] F. Fan, B. Safaei, S. Sahmani. Buckling and postbuckling response of nonlocal strain gradient porous functionally graded micro/nano-plates via NURBS-based isogeometric analysis. *Thin-Walled Structures* 159 (2021) 107231.
[72] E. Shafei, S. Faroughi, T. Rabczuk. Nonlinear transient vibration of viscoelastic plates: A NURBS-based isogeometric HSDT approach. *Computers & Mathematics with Applications* 84 (2021) 1-15.
[73] S. Yin, Z. Xiao, Y. Deng, G. Zhaang, J. Liu, S. Gu. Isogeometric analysis of size-dependent Bernoulli Euler beam based on a reformulated strain gradient elasticity theory. *Computers & Structures* 253 (2021) 106577.
[74] F. Fan, S. Sahmani, B. Safaei. Isogeometric nonlinear oscillations of nonlocal strain gradient PFGM micro/nano-plates via NURBS-based formulation. *Composite Structures* 255 (2021) 112969.
[75] D. Singh, R. Kiran, R. Vaish. Vibration and buckling analysis of agglomerated CNT composite plates via isogeometric analysis using non-polynomial shear deformation theory. *European Journal of Mechanics-A/Solids* 98 (2023) 104892.
[76] P.T. Hung, C.H. Thai, P. Phung-Van. Isogeometric free vibration of functionally graded porous magneto-electro-elastic plate reinforced with graphene platelets resting on an elastic foundation. *Computers & Mathematics with Applications* 169 (2024) 68-87.
[77] S. Verma, A. Gupta, R. Prasad, D. Oguamannam. NURBS-based isogeometric formulation for linear and nonlinear buckling analysis of laminated composite plates using constrained and unconstrained TSDTs. *Aerospace Science and Technology* 155 (2024) 109561.
[78] V. Nguyen Van Do, T.H. Ong, C.-H. Lee. Nonlinear thermal buckling analysis of temperature-dependent porous annular and circular microplates reinforced by graphene platelets by using isogeometric analysis method. *Engineering Structures* 305 (2024) 117738.
[79] P.T. Hung, C.H. Thai, P. Phung-Van. Isogeometric free vibration of functionally graded porous magneto-electro-elastic plate reinforced with graphene platelets resting on an elastic foundation. *Computers & Mathematics with Applications* 169 (2024) 68-87.
[80] V.N. Van Do, T.N. Dao, C.-H. Lee. Three-dimensional isogeometric finite element solution method for the nonlinear thermal and thermomechanical bending analysis of laminated graphene platelet-reinforced composite plates with and without cutout. *Advances in Engineering Software* 200 (2025) 103824.
[81] Y. Wang, F. Si, Z. Zhang, C. Pan, W. Zhou, H. Gu, J. Xu, H. Zhu. Nitsche-based isogeometric analysis of bending and free vibration of stiffened FGM plates with cutouts. *Computers & Structures* 310 (2025) 107677.
[82] H.Q. Le, S. Khatir, T. Cuong-Le. NURBS-based isogeometric analysis for layerwise local behavior of nano-laminated plates based on refined zigzag and nonlocal strain gradient theories. *Composite Structures* 354 (2025) 118766.
[83] H. Ding, B. Qian, Y. Hu, X. Wang, X. Zhang, R. Sun, B. Xu. A trimmed-NURBS-based thermal buckling isogeometric analysis framework for the variable stiffness plate with complex cutouts. *Advances in Engineering Software* 199 (2025) 103803.
[84] S. Sahmani, R. Ansari, M.K. Hassanzadeh-Aghdam, M. Zareichian. Development of isogeometric-finite element unified numerical methodology for nonlinear planar instability analysis of dual-phase SiO2-graphene nanoplatetlets reinforced shallow. *Computers & Structures* 321 (2026) 108082.
[85] S.J. Mehrabadi, B.S. Aragh, V. Khoshkhahesh, A. Teherpour. Mechanical buckling of nanocomposite rectangular plate reinforced by aligned and straight single-walled carbon nanotubes. *Composites Part B: Engineering* 43 (2012) 2031-2040.

[86] R. Ansari, R. Hassani, R. Gholami, H. Rouhi. Buckling and postbuckling of plates made of FG-GPL-reinforced porous nanocomposite with various shapes and boundary conditions. *International Journal of Structural Stability and Dynamics* 21 (2021) 2150063.
[87] D. Ritchie, J. Rhodes. Buckling and post-buckling behaviour of plates with holes. *Aeronautical Quarterly* 26 (1975) 281-296.

Table 1. Material characteristics of the FFRC constituents [7], [49], [53], [56]

Material	$E_L\ (GPa)$	$E_r\ (GPa)$	ν_L	ν_r	$G_L\ (GPa)$
CNT	1382.5	645	0.272	0.2	1120
Glass fiber	72.5	72.5	0.2	0.2	30.2
Epoxy	4.34	4.34	0.37	0.37	1.58

Table 2: Comparison investigation on the dimensionless MSGT-based critical axial buckling loads ($\frac{\mathcal{P}L^2}{Eh^3}$) of simply supported functionally graded microplates corresponding to diverse values of the small scale parameters (material gradient index = 1)

L/h	$l_0 = l_1 = l_2$	Ref. [14]	Current model
5	h	154.2099	154.1887
	$h/2$	44.9642	44.9551
	$h/5$	14.1785	14.1746
	$h/10$	9.7211	9.7188

	0 (CL model)	8.2245	8.2232
10	h	173.7865	173.7634
	$h/2$	50.5419	50.5323
	$h/5$	15.9590	15.9548
	$h/10$	10.9968	10.9941
	0 (CL model)	9.3391	9.3379

Table 3: Comparison investigation on the critical axial buckling loads (KN) of simply supported uniformly CNT-reinforced nanocomposite plates corresponding to diverse aspect ratios and CNT volume fractions ($h = 5\ mm$)

L_1/L_2	V_{CNT}	Ref. [85]	Current model
1	0.12	0.9977	0.9962
	0.28	1.5010	1.4998
2	0.12	1.1143	1.1134
	0.28	1.6999	1.6985
3	0.12	1.2667	1.2655
	0.28	1.9053	1.9037
4	0.12	1.4909	1.4889
	0.28	2.1876	2.1854
5	0.12	1.8387	1.8373
	0.28	2.4372	2.4356
6	0.12	2.2989	2.2972
	0.28	2.9074	2.9058

Table 4: Normalized critical buckling loads of FFRC microplates based on CL and MSGT continuum models corresponding to various GF volume fractions
($IT = 0.39\ nm, IS = 43.4\ GPa$, CNT volume fraction = maximum)

Different scale parameters	Different GF volume fraction		
	30%	50%	70%
Simply supported microplate			
CL model	0.2820	0.4331	0.5926
$l_0 = l_1 = l_2 = 20\ \mu m$	0.2919	0.4481	0.6131

$\boldsymbol{l_0 = l_1 = l_2 = 40\ \mu m}$	0.3242	0.4978	0.6811
Clamped microplate			
CL model	0.6887	1.0576	1.4471
$\boldsymbol{l_0 = l_1 = l_2 = 20\ \mu m}$	0.7127	1.0944	1.4974
$\boldsymbol{l_0 = l_1 = l_2 = 40\ \mu m}$	0.7916	1.2156	1.6633

Table 5: Normalized critical buckling shortenings of FFRC microplates based on CL and MSGT continuum models corresponding to various GF volume fractions
($IT = 0.39\ nm, IS = 43.4\ GPa$, CNT volume fraction = maximum)

Different scale parameters	**Different GF volume fraction**		
	30%	50%	70%
Simply supported microplate			
CL model	0.0558	0.0557	0.0567
$\boldsymbol{l_0 = l_1 = l_2 = 20\ \mu m}$	0.0577	0.0577	0.0586
$\boldsymbol{l_0 = l_1 = l_2 = 40\ \mu m}$	0.0641	0.0641	0.0651
Clamped microplate			
CL model	0.1362	0.1361	0.1384
$\boldsymbol{l_0 = l_1 = l_2 = 20\ \mu m}$	0.1410	0.1408	0.1432
$\boldsymbol{l_0 = l_1 = l_2 = 40\ \mu m}$	0.1566	0.1564	0.1591

Table 6: Normalized critical buckling loads of FFRC microplates based on CL and MSGT continuum models corresponding to various CNT volume fractions
($IT = 0.39\ nm, IS = 43.4\ GPa$, GF volume fraction = 50%)

Different scale parameters	**Different CNT volume fraction**		
	0.25%	1%	$maximum$
Simply supported microplate			
CL model	0.4021	0.4135	0.4331
$\boldsymbol{l_0 = l_1 = l_2 = 20\ \mu m}$	0.4159	0.4278	0.4481

$\boldsymbol{l_0 = l_1 = l_2 = 40\ \mu m}$	0.4621	0.4753	0.4978
Clamped microplate			
CL model	0.9818	1.0098	1.0576
$\boldsymbol{l_0 = l_1 = l_2 = 20\ \mu m}$	1.0160	1.0449	1.0944
$\boldsymbol{l_0 = l_1 = l_2 = 40\ \mu m}$	1.1285	1.1606	1.2156

Table 7: Normalized critical buckling shortenings of FFRC microplates based on CL and MSGT continuum models corresponding to various CNT volume fractions
($IT = 0.39\ nm, IS = 43.4\ GPa,$ GF volume fraction = 50%)

Different scale parameters	**Different CNT volume fraction**		
	0.25%	1%	$maximum$
Simply supported microplate			
CL model	0.0523	0.0539	0.0557
$\boldsymbol{l_0 = l_1 = l_2 = 20\ \mu m}$	0.0541	0.0557	0.0577
$\boldsymbol{l_0 = l_1 = l_2 = 40\ \mu m}$	0.0601	0.0619	0.0641
Clamped microplate			
CL model	0.1277	0.1315	0.1361
$\boldsymbol{l_0 = l_1 = l_2 = 20\ \mu m}$	0.1322	0.1361	0.1408
$\boldsymbol{l_0 = l_1 = l_2 = 40\ \mu m}$	0.1468	0.1512	0.1564

Table 8: Normalized critical buckling loads of FFRC microplates based on CL and MSGT continuum models corresponding to various values of IT
($IS = 43.4\ GPa,$ GF volume fraction = 50%, CNT volume fraction = maximum)

Different scale parameters	**Different values of IT**		
	0.10 nm	0.39 nm	0.78 nm
Simply supported microplate			
CL model	0.4164	0.4331	0.4893
$\boldsymbol{l_0 = l_1 = l_2 = 20\ \mu m}$	0.4309	0.4481	0.5064

$\boldsymbol{l_0 = l_1 = l_2 = 40\ \mu m}$	0.4786	0.4978	0.5625
Clamped microplate			
CL model	1.0168	1.0576	1.1950
$\boldsymbol{l_0 = l_1 = l_2 = 20\ \mu m}$	1.0522	1.0944	1.2366
$\boldsymbol{l_0 = l_1 = l_2 = 40\ \mu m}$	1.1687	1.2156	1.3735

Table 9: Normalized critical buckling shortenings of FFRC microplates based on CL and MSGT continuum models corresponding to various values of IT
($IS = 43.4\ GPa$, GF volume fraction = 50%, CNT volume fraction = maximum)

Different scale parameters	**Different values of IT**		
	$0.10\ nm$	$0.39\ nm$	$0.78\ nm$
Simply supported microplate			
CL model	0.0547	0.0557	0.0579
$\boldsymbol{l_0 = l_1 = l_2 = 20\ \mu m}$	0.0566	0.0577	0.0600
$\boldsymbol{l_0 = l_1 = l_2 = 40\ \mu m}$	0.0629	0.0641	0.0666
Clamped microplate			
CL model	0.1336	0.1361	0.1415
$\boldsymbol{l_0 = l_1 = l_2 = 20\ \mu m}$	0.1382	0.1408	0.1464
$\boldsymbol{l_0 = l_1 = l_2 = 40\ \mu m}$	0.1535	0.1564	0.1626

Table 10: Normalized critical buckling loads of FFRC microplates based on CL and MSGT continuum models corresponding to various values of IS
($IT = 0.39\ nm$, GF volume fraction = 50%, CNT volume fraction = maximum)

Different scale parameters	**Different values of IS**		
	$4.34\ GPa$	$43.4\ GPa$	$434\ GPa$
Simply supported microplate			
CL model	0.4129	0.4331	0.4382
$\boldsymbol{l_0 = l_1 = l_2 = 20\ \mu m}$	0.4273	0.4481	0.4535

$\boldsymbol{l_0 = l_1 = l_2 = 40\ \mu m}$	0.4746	0.4978	0.5037
Clamped microplate			
CL model	1.0083	1.0576	1.0701
$\boldsymbol{l_0 = l_1 = l_2 = 20\ \mu m}$	1.0435	1.0944	1.1074
$\boldsymbol{l_0 = l_1 = l_2 = 40\ \mu m}$	1.1590	1.2156	1.2300

Table 11: Normalized critical buckling shortenings of FFRC microplates based on CL and MSGT continuum models corresponding to various values of IS
($IT = 0.39\ nm$, GF volume fraction = 50%, CNT volume fraction = maximum)

Different scale parameters	**Different values of IS**		
	$4.34\ GPa$	$43.4\ GPa$	$434\ GPa$
Simply supported microplate			
CL model	0.0545	0.0557	0.0563
$\boldsymbol{l_0 = l_1 = l_2 = 20\ \mu m}$	0.0563	0.0577	0.0582
$\boldsymbol{l_0 = l_1 = l_2 = 40\ \mu m}$	0.0626	0.0641	0.0647
Clamped microplate			
CL model	0.1330	0.1361	0.1374
$\boldsymbol{l_0 = l_1 = l_2 = 20\ \mu m}$	0.1376	0.1408	0.1421
$\boldsymbol{l_0 = l_1 = l_2 = 40\ \mu m}$	0.1528	0.1564	0.1579

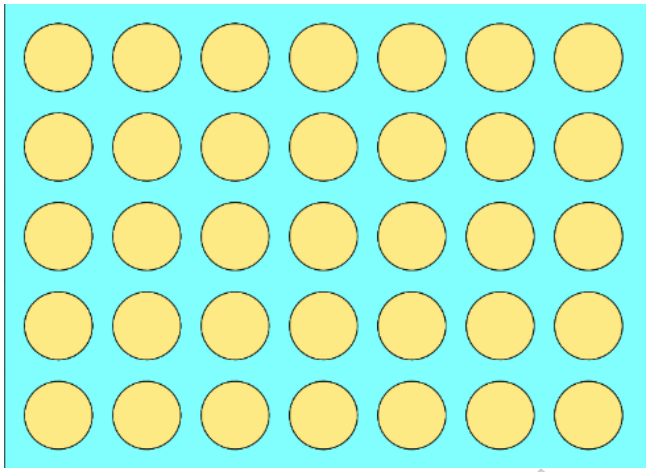

Fig. 1 Reinforcements arranged in a repeating array

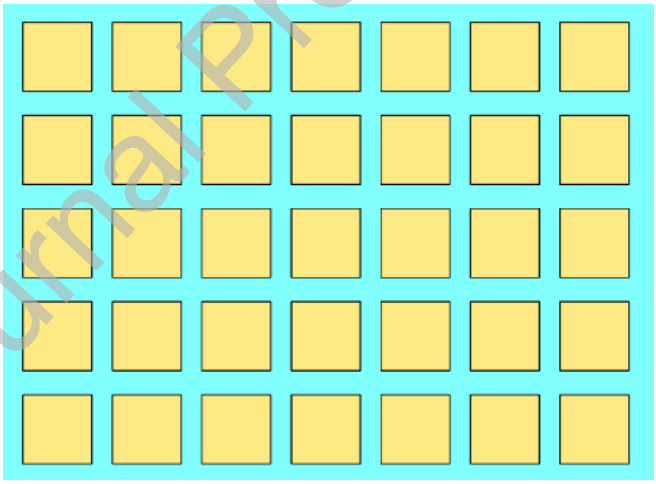

Fig. 2 Reinforcements arranged in a repeating array within the unit cell model

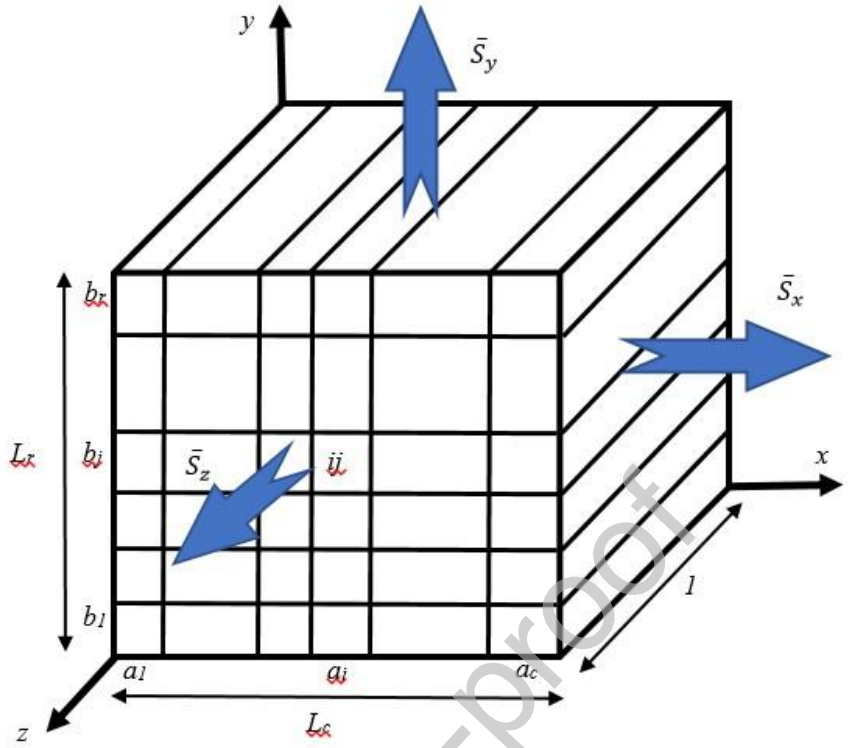

Fig. 3. Schematic of the RVE in the SUC model

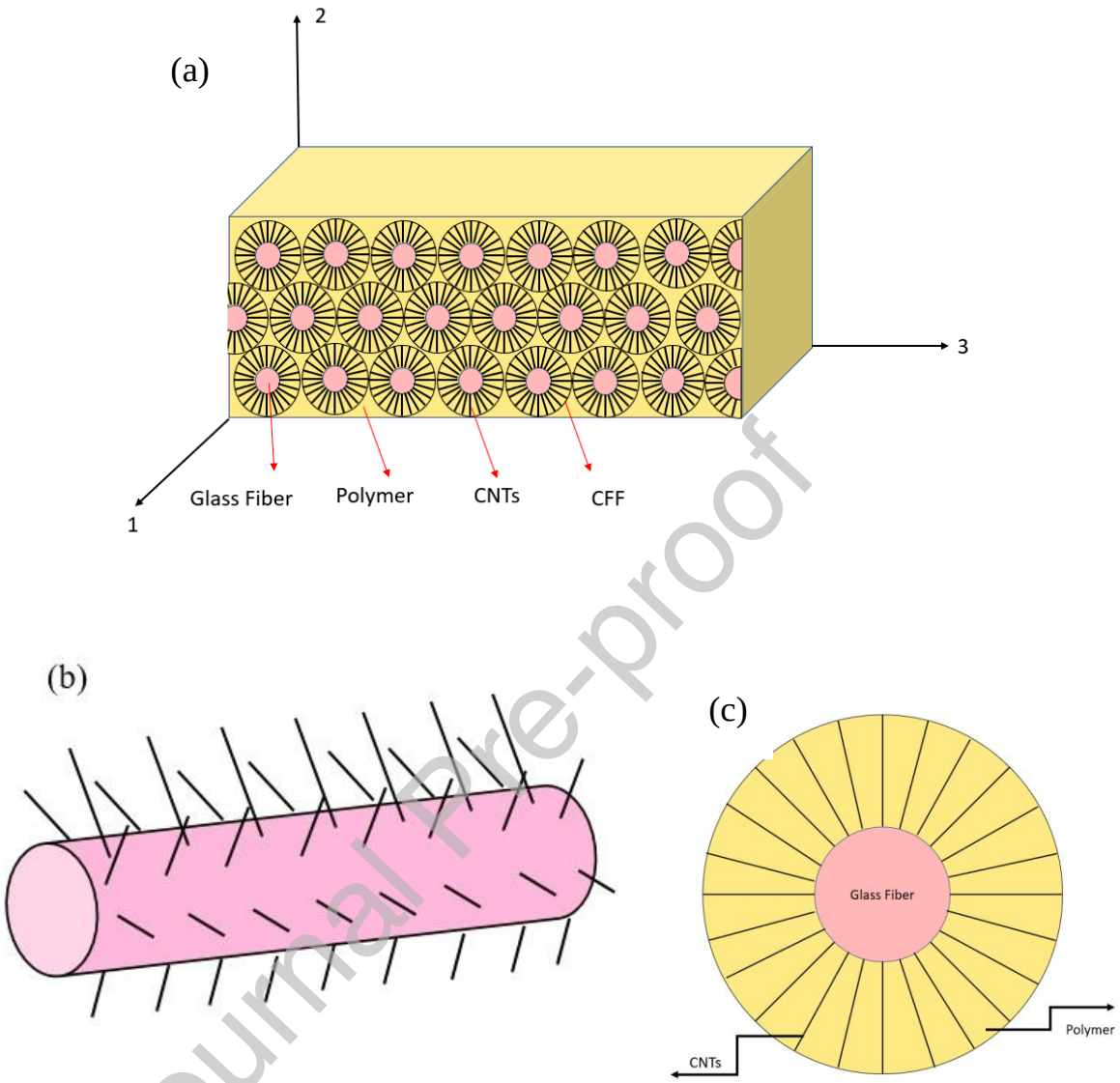

Fig. 4. (a) A lamina of the FFRC, consisting of glass fibers, CNTs, and a polymer matrix; (b) radially aligned CNTs uniformly distributed along the surface of a glass fiber (fuzzy fiber); (c) transverse cross-sectional view of the composite fuzzy fiber

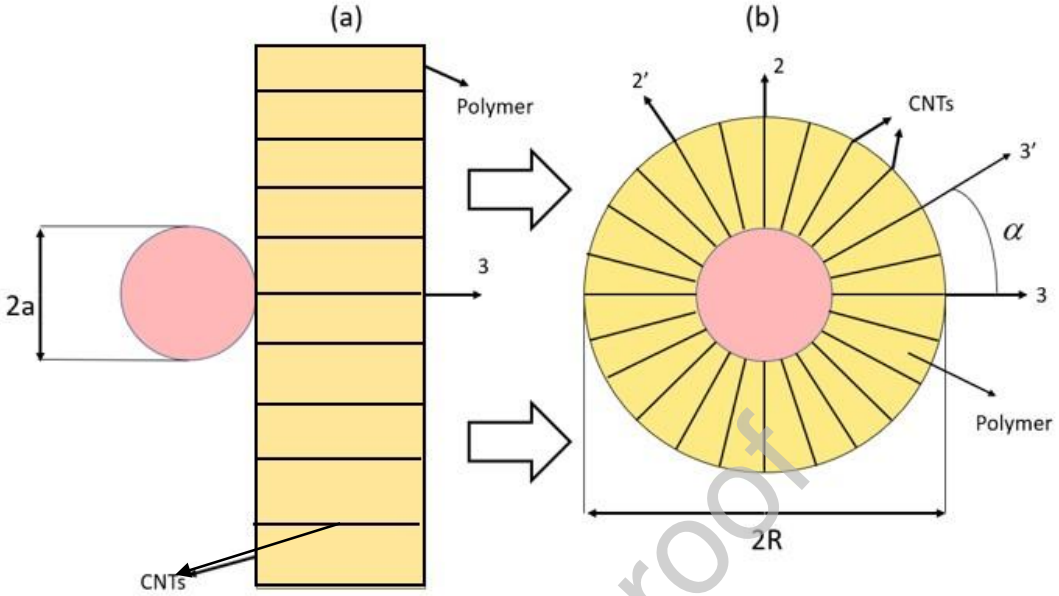

Fig. 5. Transverse cross-section of the composite fuzzy fiber featuring (a) an unrolled and (b) a rolled polymer matrix nanocomposite

Fig. 6. Modeled FFRC microplates having different geometries

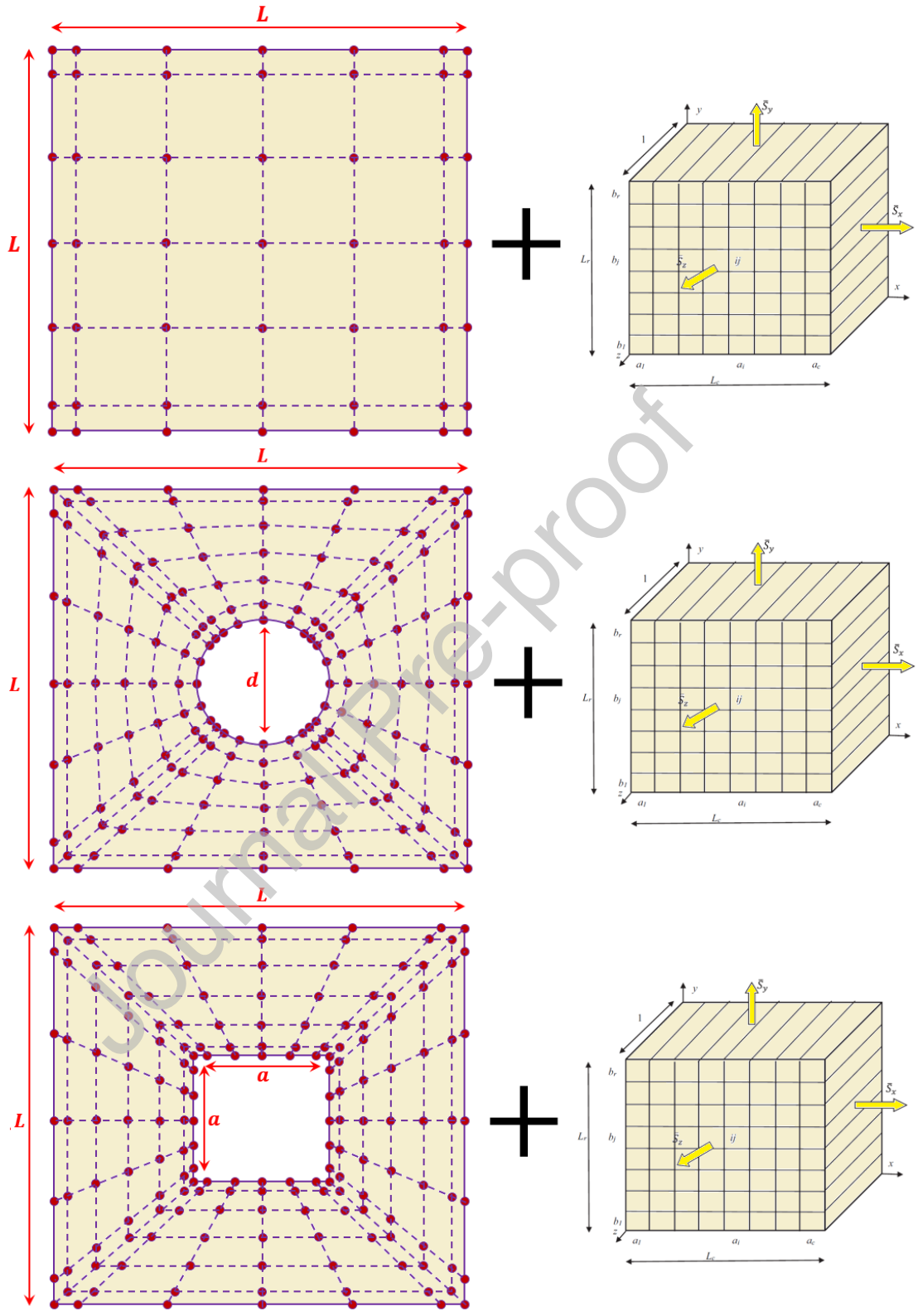

Fig. 7. Unified isogeometric-SUC models using cubic elements

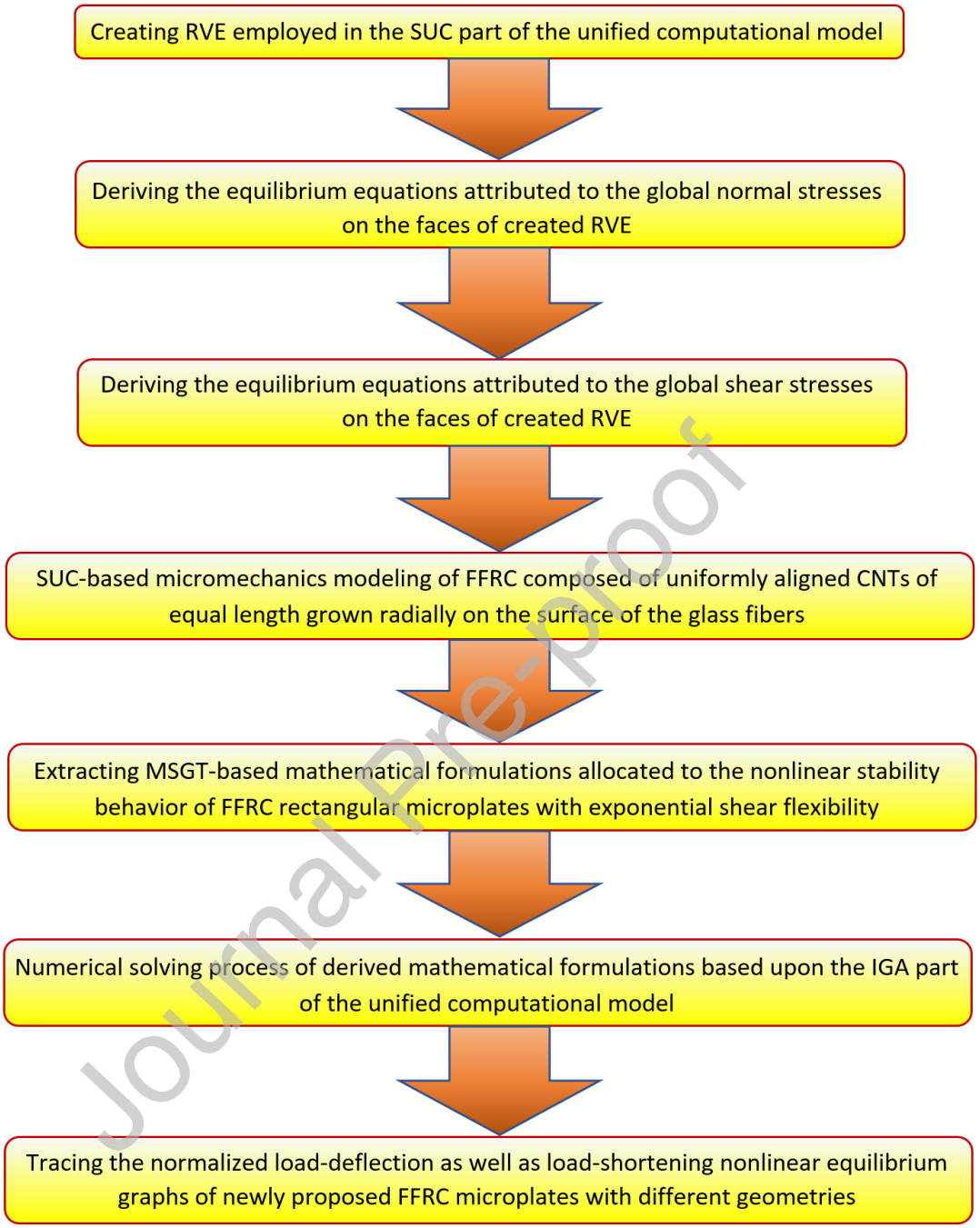

Fig. 8. The flowchart of computational scenario attributed to the developed unified SUC-IGA model

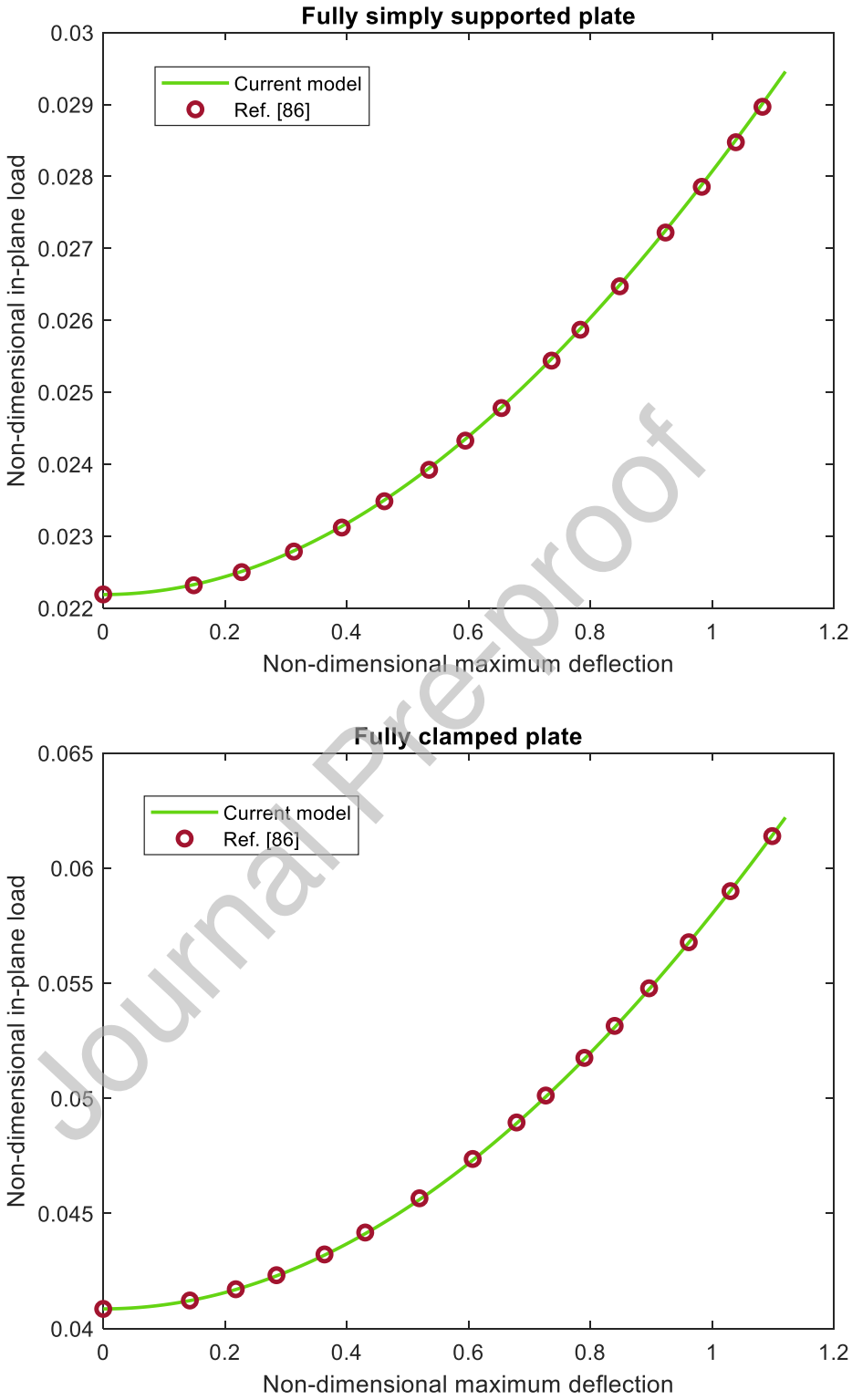

Fig. 9. Comparative investigation of the nonlinear stability behavior of porous nanocomposite rectangular plates containing a square central cutout and subjected to biaxial compressive loading and fully boundary conditions $(L_1 = L_2 = L = 16h, a = 0.1L)$

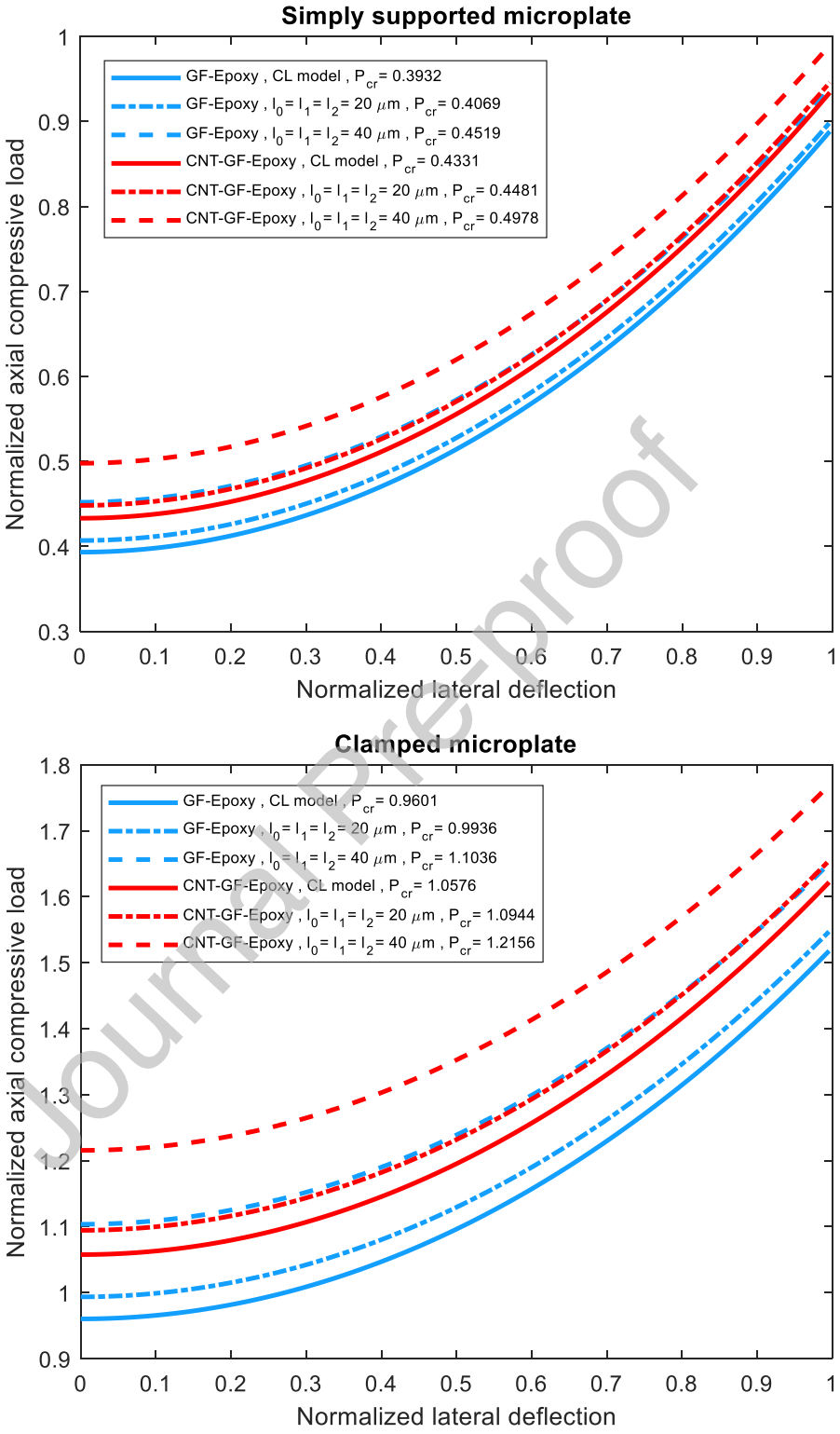

Fig. 10. CL-based and MSGT-based load-deflection nonlinear equilibrium graphs allocated to different values of small scale parameters ($IT = 0.39\ nm, IS = 43.4\ GPa, V_{CNT} = \text{maximum}, \text{V}_{\text{GF}} = 50\%$)

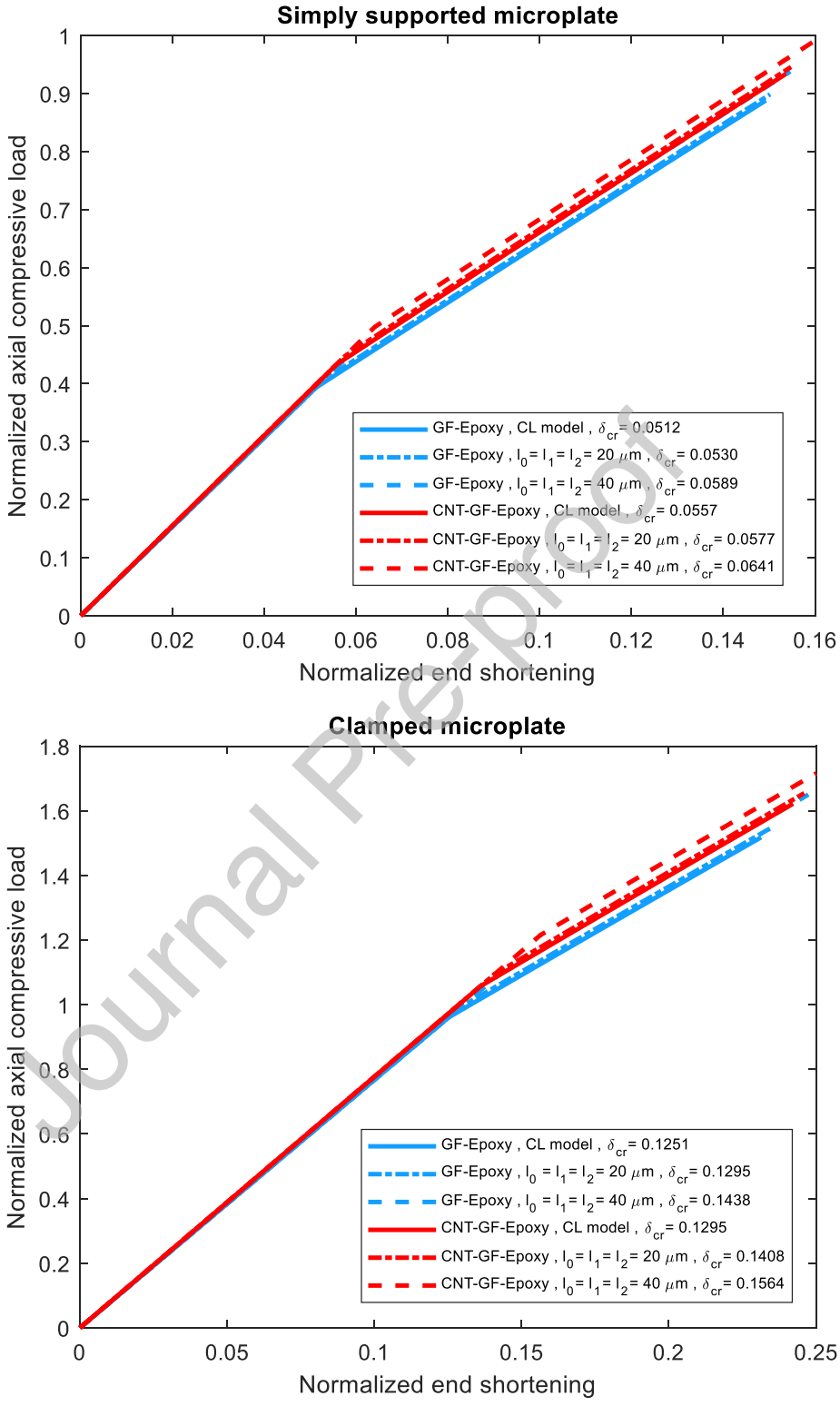

Fig. 11. CL-based and MSGT-based load-shortening nonlinear equilibrium graphs allocated to different values of small scale parameters ($IT = 0.39\ nm, IS = 43.4\ GPa, V_{CNT} = \text{maximum}, \text{V}_{\text{GF}} = 50\%$)

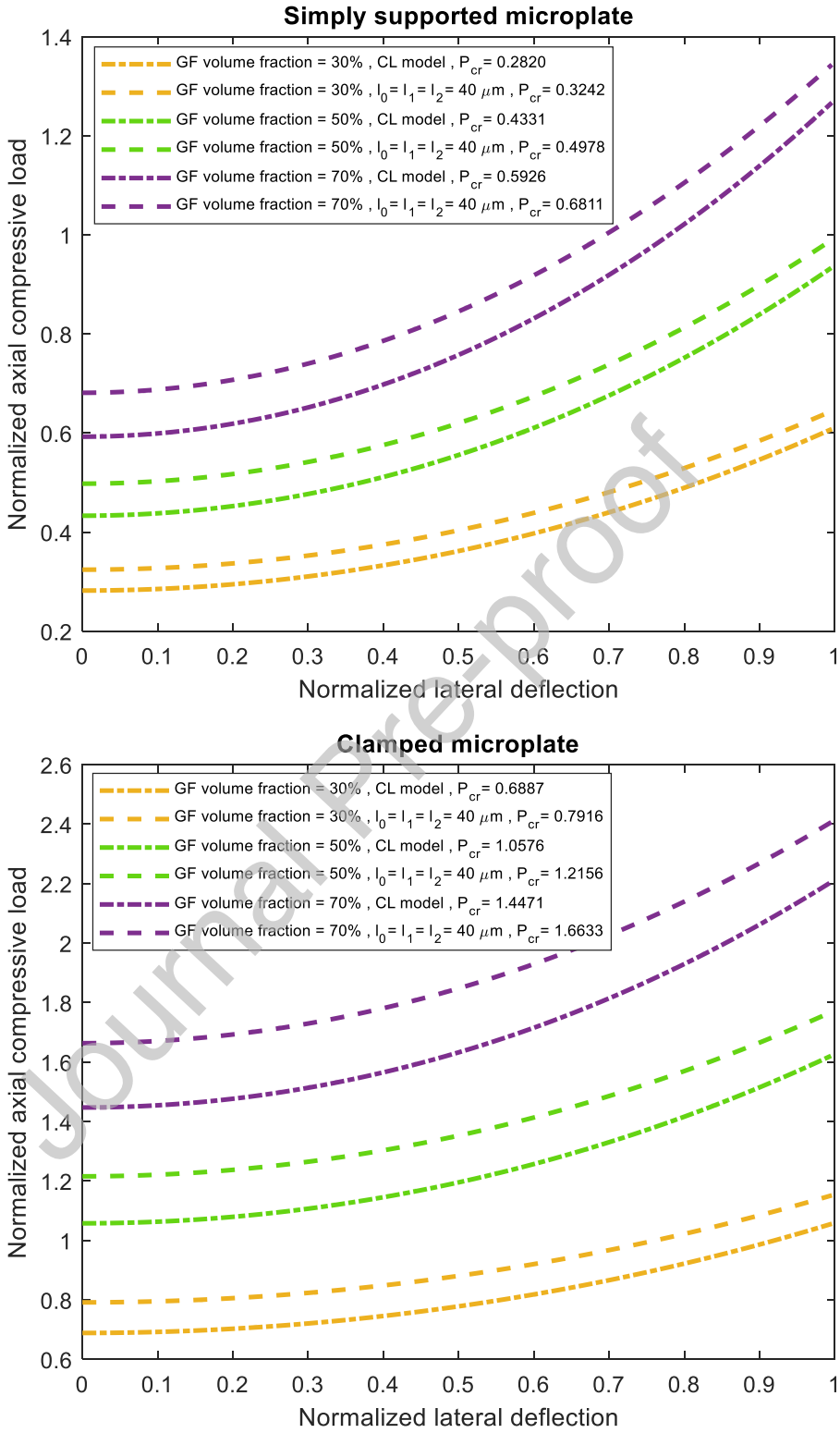

Fig. 12. CL-based and MSGT-based load-deflection nonlinear equilibrium graphs allocated to different values of GF volume fraction ($IT = 0.39\ nm, IS = 43.4\ GPa, V_{CNT} =$ maximum)

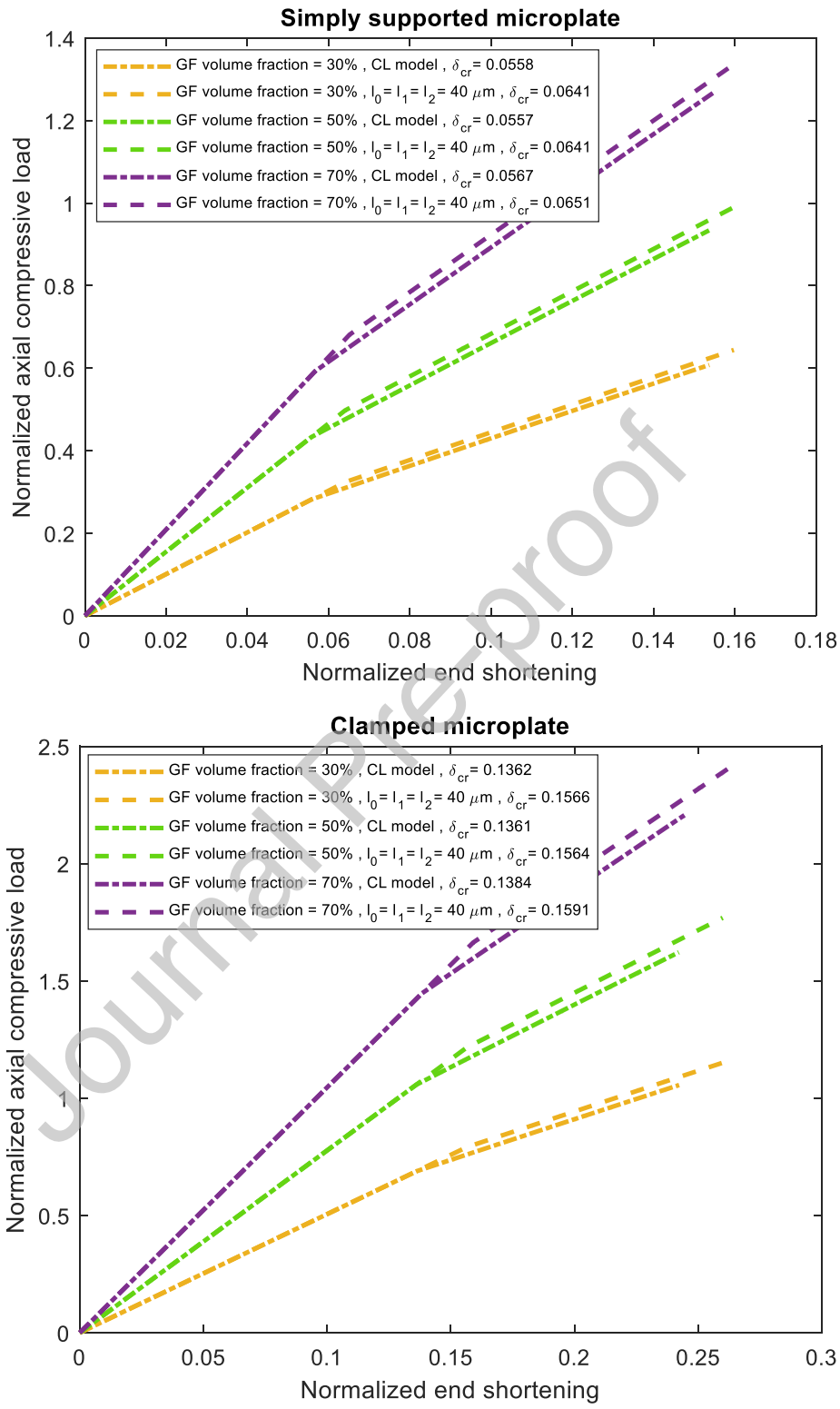

Fig. 13. CL-based and MSGT-based load-shortening nonlinear equilibrium graphs allocated to different values of GF volume fraction ($IT = 0.39\ nm, IS = 43.4\ GPa, V_{CNT}$ = maximum)

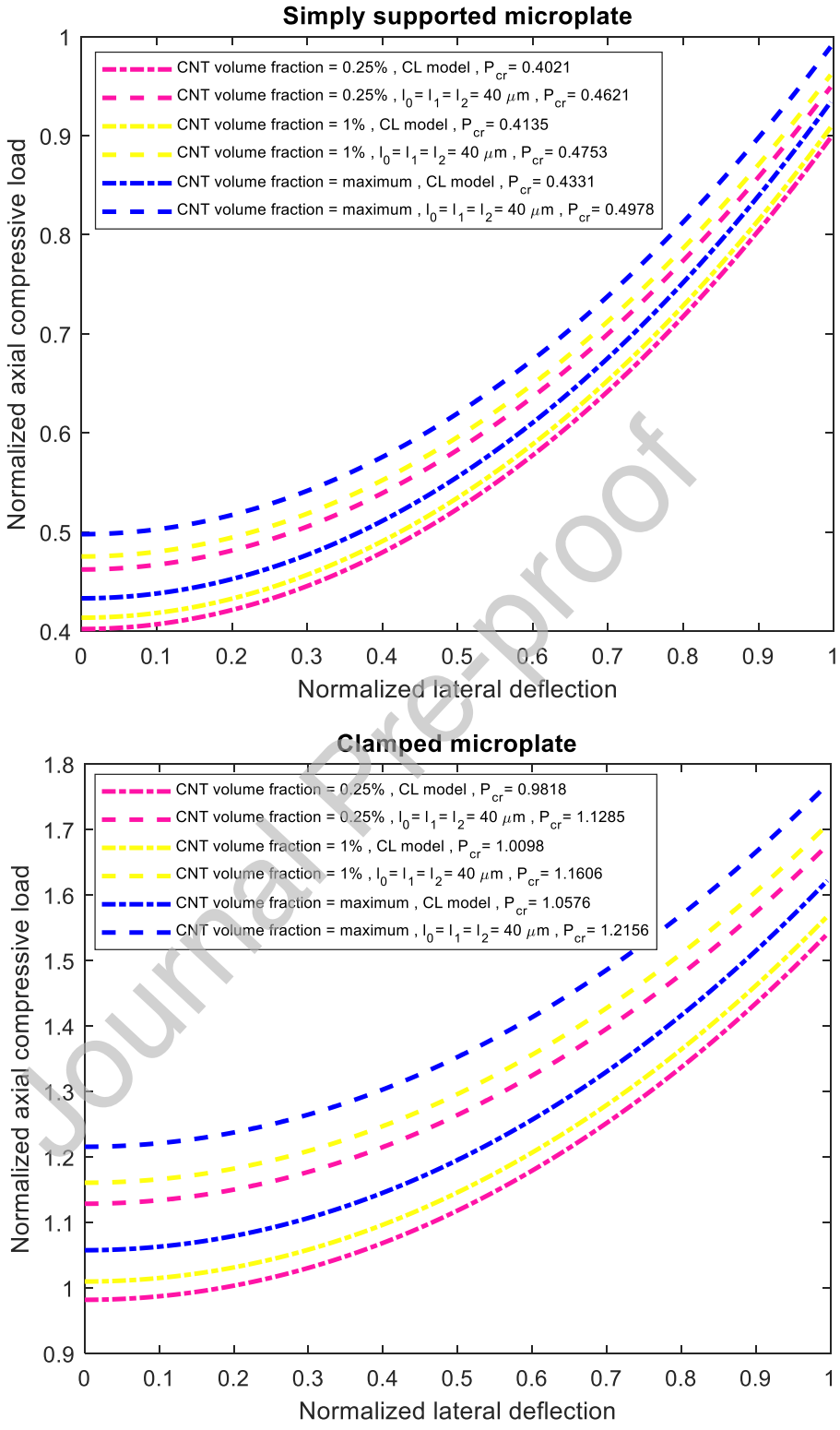

Fig. 14. CL-based and MSGT-based load-deflection nonlinear equilibrium graphs allocated to different values of CNT volume fraction ($IT = 0.39\ nm, IS = 43.4\ GPa, \mathrm{V_{GF}} = 50\%$)

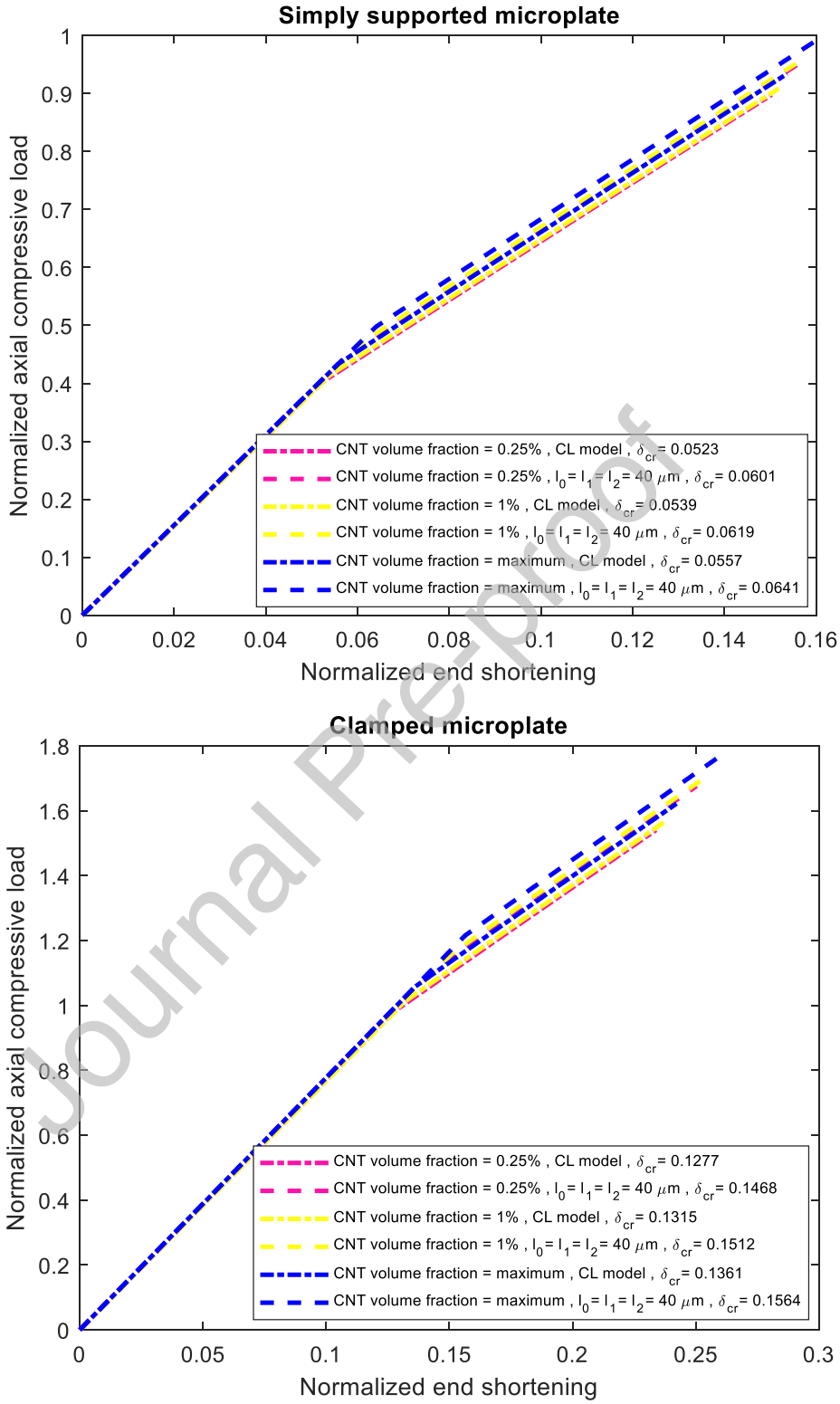

Fig. 15. CL-based and MSGT-based load-shortening nonlinear equilibrium graphs allocated to different values of CNT volume fraction ($IT = 0.39\ nm, IS = 43.4\ GPa, \mathrm{V_{GF}} = 50\%$)

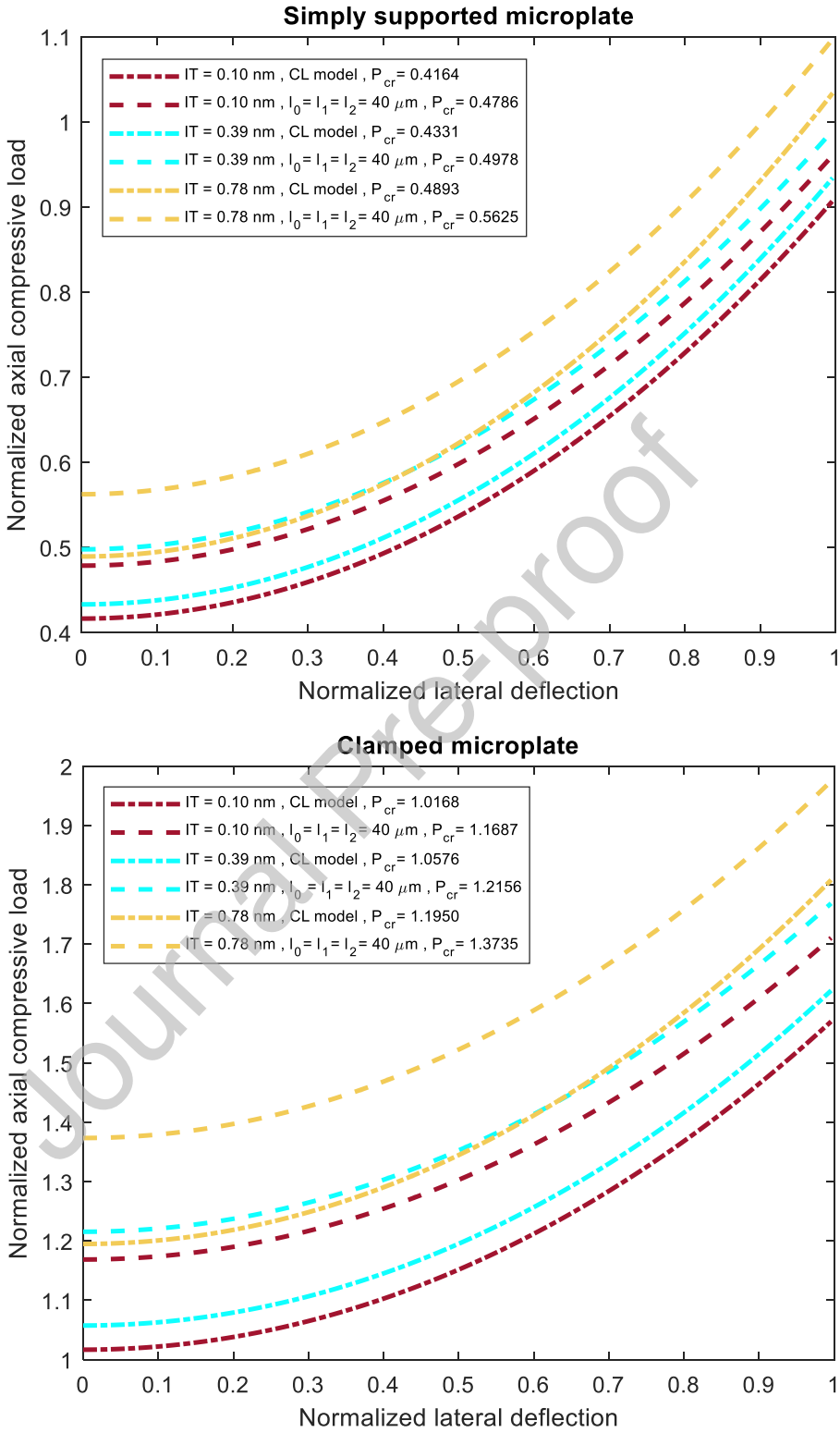

Fig. 16. CL-based and MSGT-based load-deflection nonlinear equilibrium graphs allocated to different values of IT ($IS = 43.4\ GPa, V_{CNT} = \text{maximum}, \text{V}_{\text{GF}} = 50\%$)

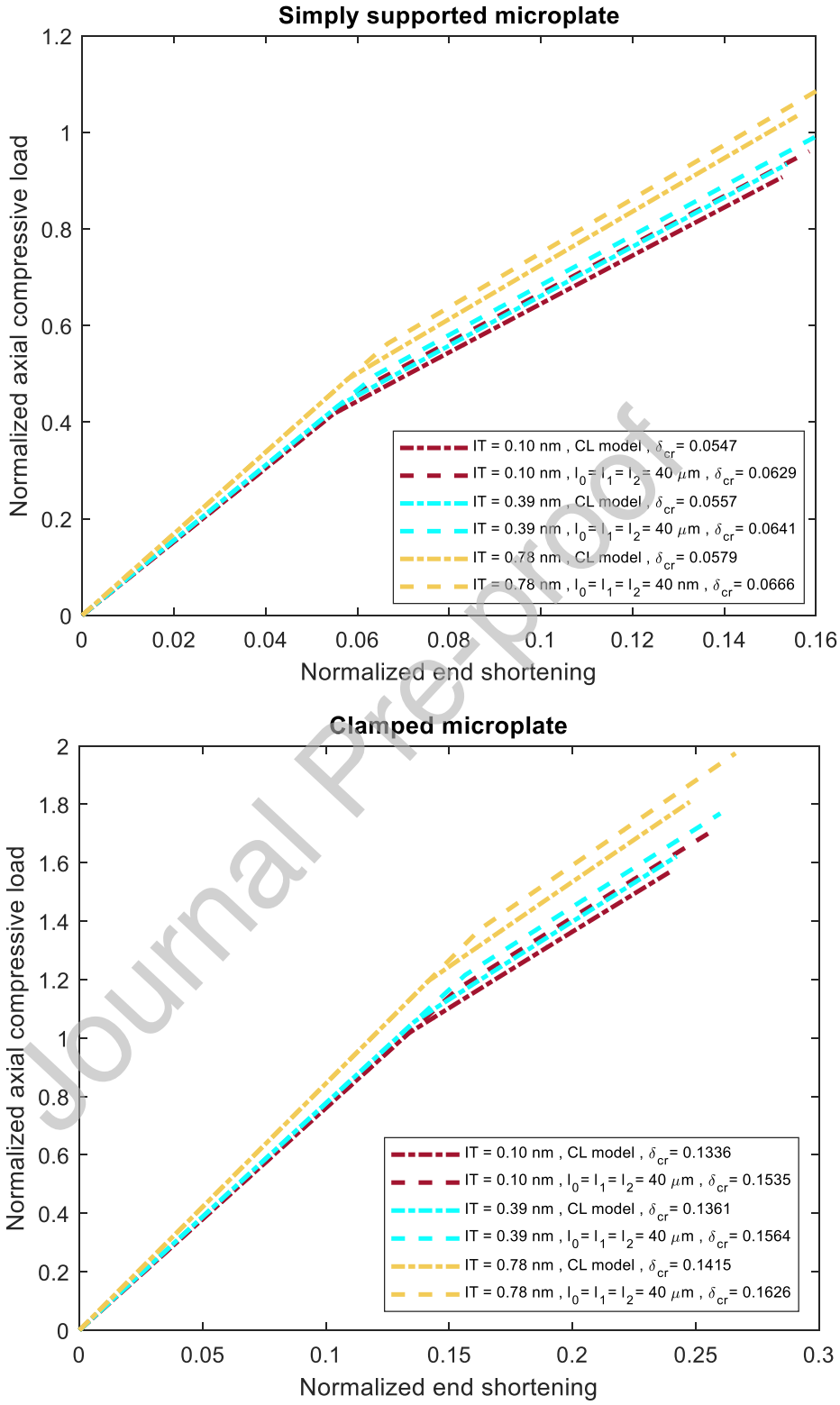

Fig. 17. CL-based and MSGT-based load-shortening nonlinear equilibrium graphs allocated to different values of IT ($IS = 43.4\ GPa, V_{CNT} = \text{maximum}, \text{V}_{\text{GF}} = 50\%$)

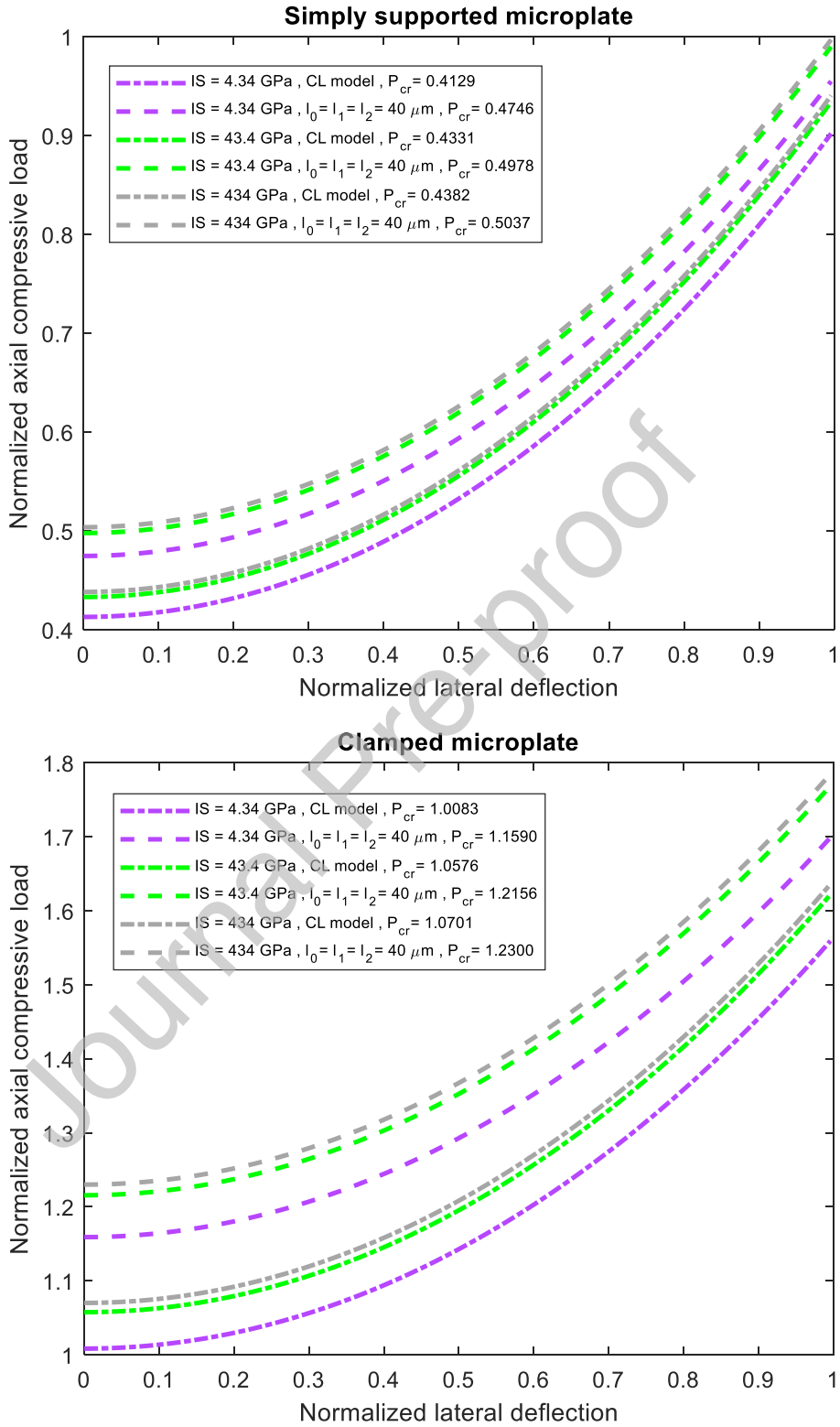

Fig. 18. CL-based and MSGT-based load-deflection nonlinear equilibrium graphs allocated to different values of IS ($IT = 0.39\ nm, V_{CNT} = \text{maximum}, \text{V}_{\text{GF}} = 50\%$)

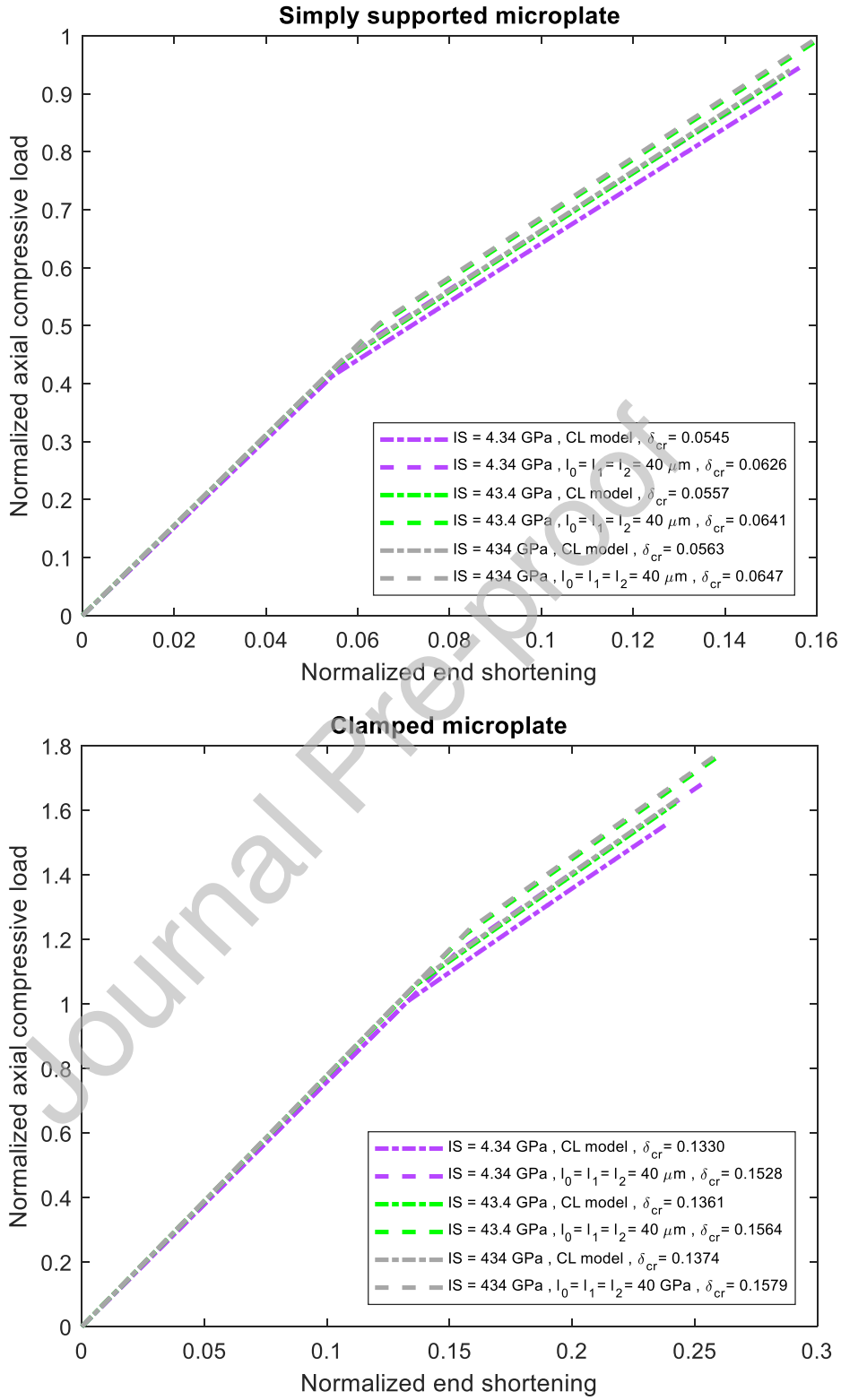

Fig. 19. CL-based and MSGT-based load-deflection nonlinear equilibrium graphs allocated to different values of IS ($IT = 0.39\ nm, V_{CNT} = \text{maximum}, \text{V}_{\text{GF}} = 50\%$)

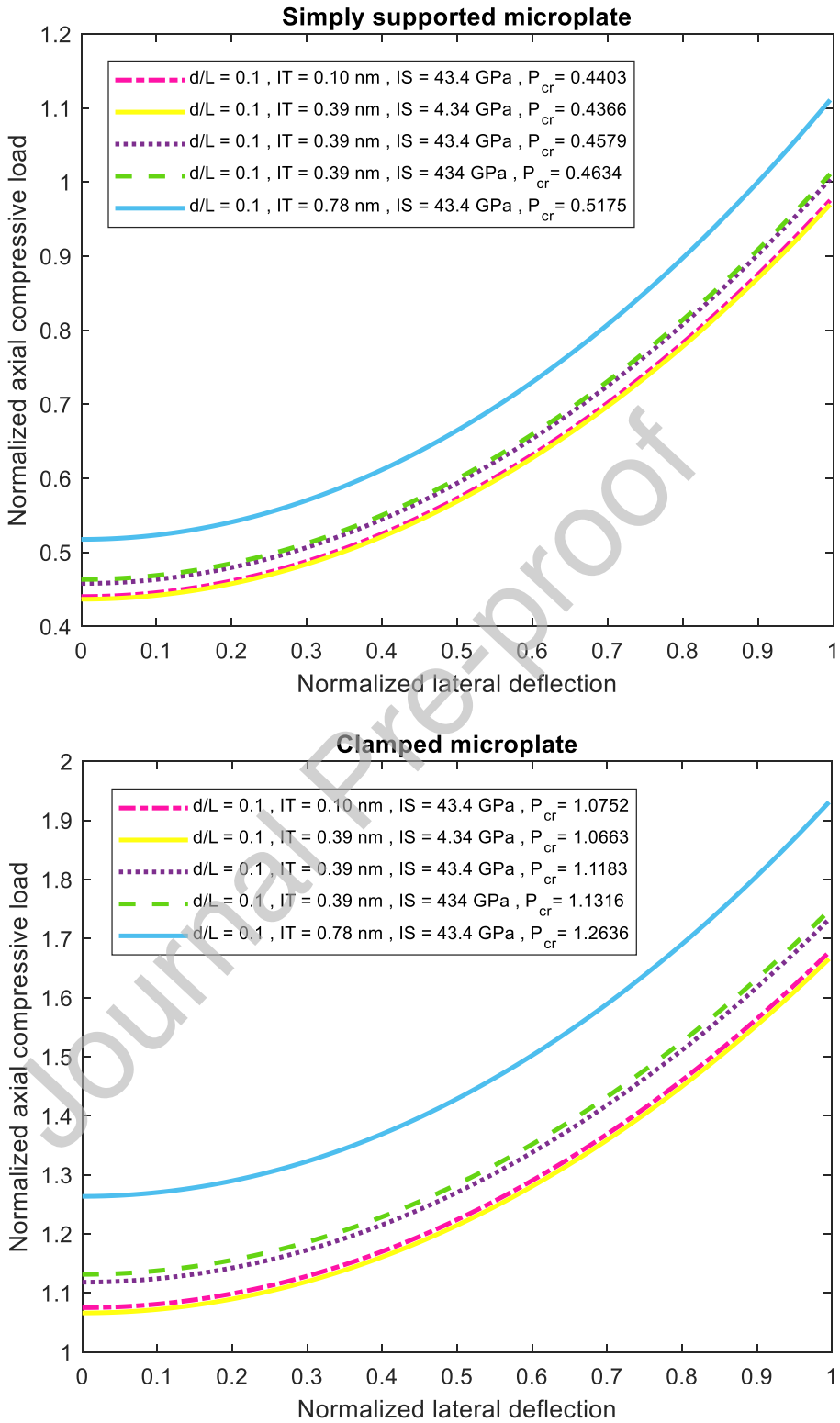

Fig. 20. MSGT-based load-deflection nonlinear equilibrium graphs allocated to the microplate having a central circular cutout ($l_0 = l_1 = l_2 = 40\ \mu m, V_{CNT} = \text{maximum}, \text{V}_{\text{GF}} = 50\%$)

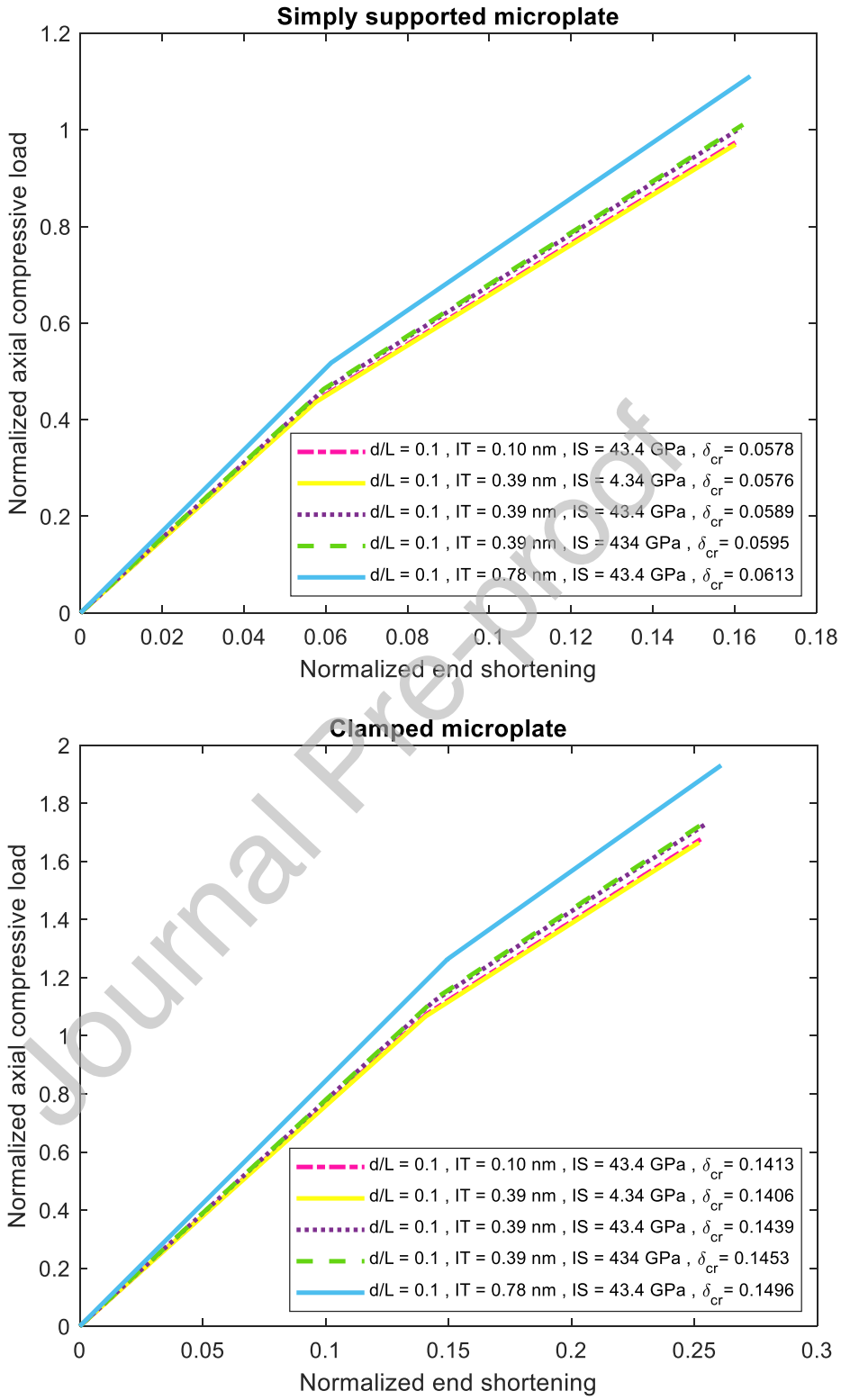

Fig. 21. MSGT-based load-shortening nonlinear equilibrium graphs allocated to the microplate having a central circular cutout ($l_0 = l_1 = l_2 = 40\ \mu m, V_{CNT} = \text{maximum}, \text{V}_{\text{GF}} = 50\%$)

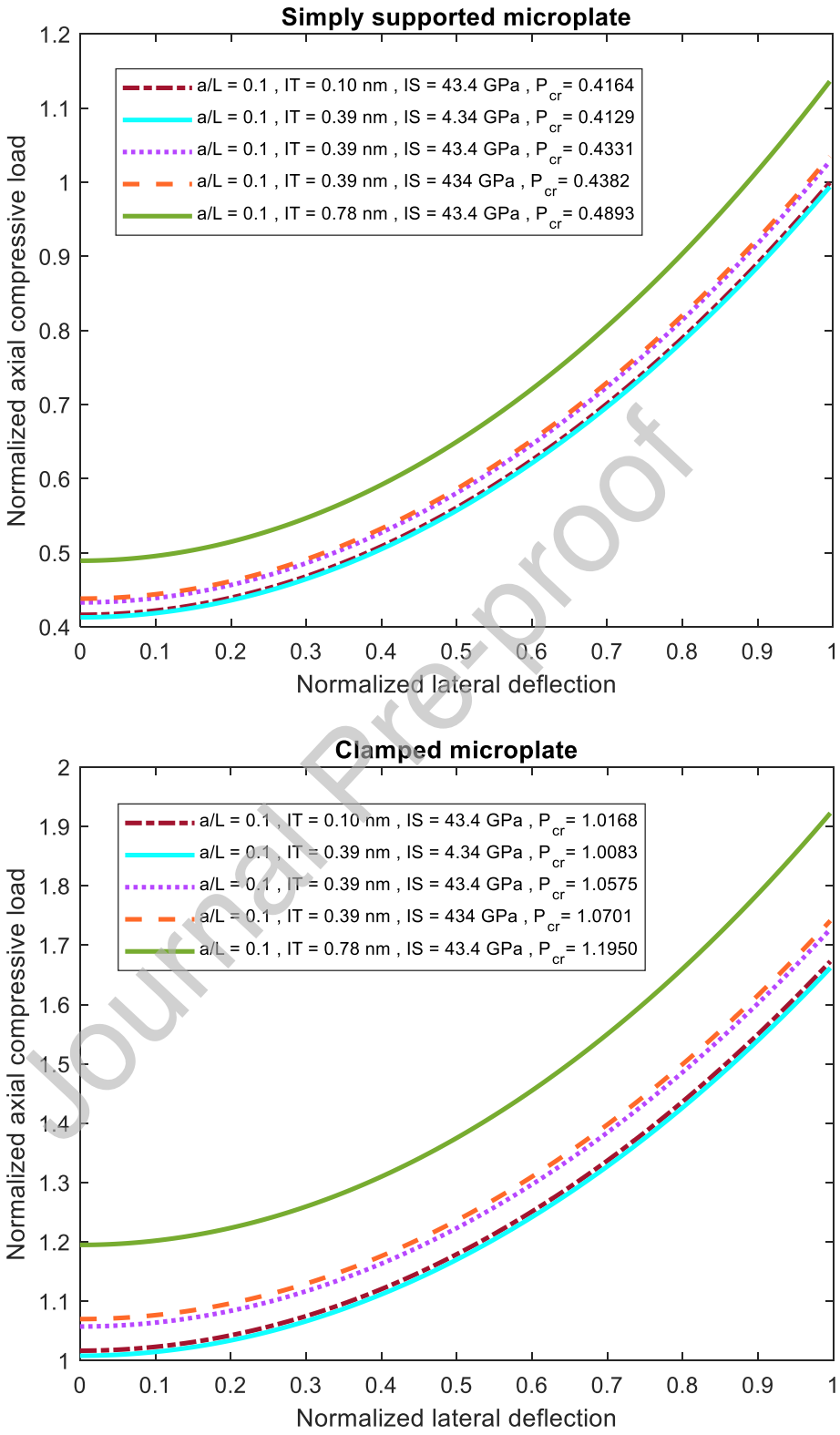

Fig. 22. MSGT-based load-deflection nonlinear equilibrium graphs allocated to the microplate having a central square cutout ($l_0 = l_1 = l_2 = 40\ \mu m, V_{CNT} = \text{maximum}, \mathrm{V_{GF}} = 50\%$)

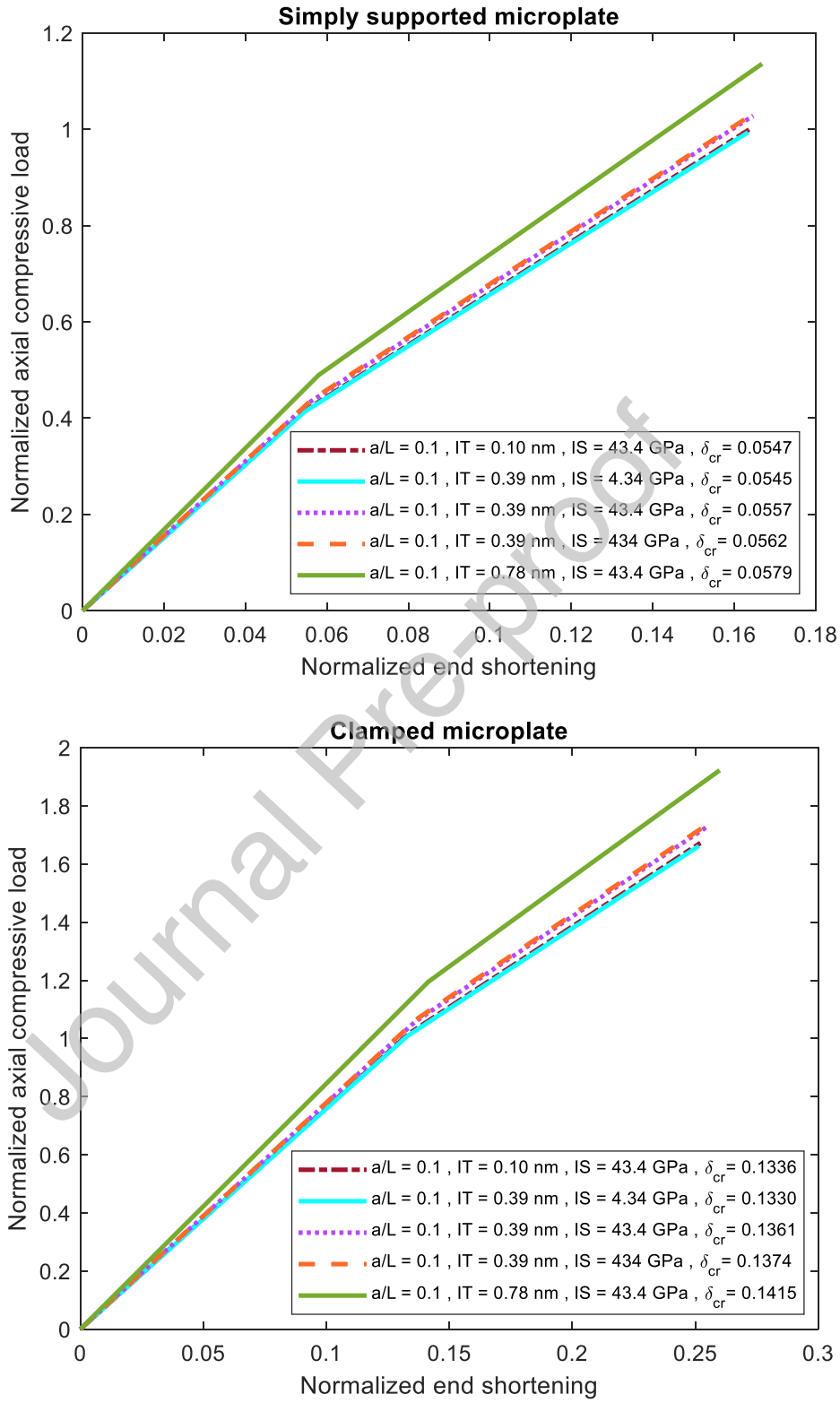

Fig. 23. MSGT-based load-shortening nonlinear equilibrium graphs allocated to the microplate having a central square cutout ($l_0 = l_1 = l_2 = 40\ \mu m, V_{CNT} = \text{maximum}, \text{V}_{\text{GF}} = 50\%$)

Credit Author Statement

- Saeid Sahmani
  Conceptualization; Formal analysis; Methodology; Investigation
- Eligiusz Postek
  Conceptualization; Methodology; Project administration; Writing – Review & Editing
- Reza Ansari
  Investigation; Validation; Data curation; Writing – Review & Editing
- Mohammad Kazem Hassanzadeh-Aghdam
  Formal analysis; Investigation; Writing – Original Draft

Declaration of Interest Statement

It is confirmed that there is no conflict of interest, no financial or personal relationships that may be perceived as influencing our work.

Thank you for your kind consideration.

All the best,

Prof. Saeid Sahmani

Institute of Fundamental Technological Research – Polish Academy of Sciences